CHARACTERIZING THE MOUSE DEAFNESS GENE BAIAP2L2

By

Julia B. Halford

A DISSERTATION

Presented to the Neuroscience Graduate Program

and the Oregon Health & Science University

School of Medicine in partial fulfillment of

the requirements for the degree of

Doctor of Philosophy

March 2022

Table of Contents

List of Figures & Tables

Figures

Supplemental Figures

Tables

Acknowledgements

I thank Dr. Peter Barr-Gillespie for the excellent mentorship and support over the past 4 years. Peter has taught me how to carefully formulate my approach to scientific problems, while also giving me ample freedom to pursue the experiments and lines of thought I find interesting (and to realize when I have perhaps not thought through every aspect of something). I thank my fellow lab members for their considerable help. Dr. Paroma Chatterjee first showed me how to do inner ear dissections, an invaluable skill for the Barr-Gillespie lab. Dr. Jocelyn Krey gave me many useful experimental ideas that I deeply appreciate. Jennifer Goldsmith kept track of the many mouse lines I used; my experiments would have been far more difficult without her. Michael Bateschell generated the *Eps8* mouse line, made many plasmids, and performed many surgeries. I thank him for these contributions to my work in the lab and this dissertation. I thank my committee members, Dr. Philip Stork, Dr. John Brigande, Dr. Kelly Monk and Dr. Mike Cohen, for their guidance and patience. I thank my previous mentor, Dr. Ina Wanner, for getting me started down this exciting path of scientific research. And lastly, I thank my favorite people. I thank my parents, Annette Swarzenski and Keith Halford, for their support and faith in me. I thank my sister Margit Halford for her bad science puns in response to almost any lab-related comment. I thank my partner Nicholas Lawrence for his good-natured patience with my (continuing) indecisiveness on post-PhD plans, and for being there to talk through anything.

Abstract

The hair bundle, an exquisitely structured organelle of filamentous actin-based protrusions, mediates the transduction of sound into electrochemical signals, thus enabling the sense of hearing. The correct assembly of the bundle during development is therefore essential to hearing. While many molecules involved in the development and maintenance of the bundle have been identified and examined in depth, there nonetheless remains much to be understood about how hair cells so consistently generate the precisely stereotyped structure of the bundle. This dissertation examines the contribution of a novel mouse deafness gene, *Brain-specific angiogenesis inhibitor 1-associated protein 2-like protein 2* (*Baiap2l2*), to bundle maintenance and function. Chapter 1 contextualizes the experiments described in the ensuing chapters by describing how *Baiap2l2* was identified as a candidate hair cell marker, discussing the bin-amphiphysin-Rvs (BAR) family of proteins to which BAIAP2L2 belongs, and providing background on bundle development. Chapter 2 presents the characterization of two *Baiap2l2* mouse knockouts, revealing that *Baiap2l2* deficiency causes progressive deafness likely explained by gradual deterioration of the transducer current and transducing stereocilia. Chapter 3 examines the mechanisms through which BAIAP2L2 is targeted within the hair bundle, demonstrating that BAIAP2L2 relies on active transduction currents to remain localized at stereocilia tips, and identifying Ca^{2+} as a specific factor required for that maintenance. Altogether, this dissertation deepens the understanding of the molecular underpinnings of bundle assembly by adding BAIAP2L2 as an essential factor for bundle stability and by providing evidence for Ca^{2+} as a mediator of how transduction modulates bundle proteins.

Chapter 1 – Introduction

Form and development of hair bundles

Perception of the outside world relies on the transduction of a variety of stimuli into electrochemical signals that can be processed by the central nervous system. The auditory hair bundle is a particularly elegant example of the means through which such transduction can occur. Bundles are highly specialized elaborations of the apical surface of hair cells, the specialized sensory cells that mediate the senses of hearing and balance. These elaborations take the form of stereocilia, hair-like extensions from the cell surface that are densely filled with filamentous actin packed in a paracrystalline array (Tilney *et al.*, 1980). In mammalian auditory bundles, the stereocilia form a staircase-like pattern, with the stereocilia arrayed in three rows of incrementing height (Kaltenbach *et al.*, 1994) (Fig. 1-1A). The dimensions of individual stereocilia within each row are remarkably uniform. The conversion of sound to electrochemical signal happens as the bundle is deflected towards its tallest row (row 1) of stereocilia. Mechanically-gated channels located at the tips of the two shorter rows (rows 2 and 3) are coupled to their taller neighbors with extracellular filaments known as tip links (Fig. 1-1B). Bundle deflection allows channels to open beyond their resting state, allowing influx of K^+ and Ca^{2+} to depolarize the cell, leading to transmission of that signal along the auditory pathway for the brain to interpret (Fettiplace and Kim, 2014).

Assembly of the bundle, so that each of the rows of stereocilia are positioned correctly relative to each other and their heights are appropriately spaced to allow channel openings in response to specific stimuli, is tightly regulated, and occurs in a series of distinct stages (Tilney *et al.*, 1992; Kaltenbach *et al.*, 1994; Krey *et al.*, 2020) (Fig. 1-1C). Bundle morphogenesis begins with a lawn of microvilli, from which a primary cilium, the kinocilium, migrates to one side of the cell as planar polarity is determined. The microvilli closest to the kinocilium begin to elongate as those furthest away begin to resorb as the bundle's characteristic staircase is established. After the initial phase of elongation, rows 1 and 2 of the stereocilia begin to widen. The final stage in bundle development is a refinement of stereocilia heights, as row 1 lengthens again and row 2 is slightly shortened.

Dysregulation of any of these processes during development can lead to mature hair bundles with stereocilia that are disorganized or depart significantly from their requisite staircase arrangement, whether that is through the loss of rows (Furness *et al.*, 2013; Fang *et al.*, 2015), the presence of extra rows (Du *et al.*, 2021), or differences in the step sizes between row heights (Probst *et al.*, 1998; Zampini *et al.*, 2011; Giese *et al.*, 2017). In turn, deviations from normal bundle morphology frequently cause disruptions in the bundle's capacity for transduction, and thus deficits in hearing. The clear relationship between an intact bundle and auditory function has greatly facilitated the genetic dissection and identification of many of the bundle's component molecules (Frolenkov *et al.*, 2004; Petit and Richardson, 2009). Examination of deafness mutants continues to provide insight into the assembly of the hair bundle, a complex process yet to be solved in its entirety (Barr-Gillespie, 2015).

Baiap2l2 deficiency is implicated in hearing loss.

The gene *Brain-specific angiogenesis inhibitor 1-associated protein 2-like protein 2* (*Baiap2l2*) arose as a candidate for study in a screen for hearing loss in mouse knockout strains performed by the International Mouse Phenotyping Consortium (IMPC) (Bowl *et al.*, 2017). This screen used auditory brainstem response (ABR) testing, which determines the minimum sound pressure level required to evoke a measurable response (Willott, 2006), to identify genes of interest for the field of hearing research. *Baiap2l2* variants appear to also have implications for human hearing health. A genome-wide association study discovered a single nucleotide polymorphism in a non-coding portion of the *BAIAP2L2* gene associated with self-reported hearing loss (Wells *et al.*, 2019). More recently, whole exome analysis of patients with hearing loss has also identified a variant of *BAIAP2L2* that causes hearing loss that follows an autosomal dominant inheritance pattern (Mutai *et al.*, 2022).

Several experiments described in this dissertation seek to deepen the understanding of the consequences for *Baiap2l2* deficiency on hearing by more completely characterizing the auditory phenotype. In Chapter 2, ABRs were measured at several frequencies in *Baiap2l2*-null mice at time points between the ages of post-natal day 14 (P14) and ~P200 to examine the progression of the phenotype. Further, distortion product otoacoustic emissions (DPOAEs) were measured at the same time points as ABRs to assess outer hair cell (OHC) function of *Baiap2l2*-null mice. As DPOAEs are a product of cochlear amplification produced by OHC motility (Martin *et al.*, 2006), they can provide some insight to the contribution of OHC dysfunction to an observed auditory deficit. Chapter 2 also examines the impact of *Baiap2l2* deficiency on the transduction current.

The data from IMPC clearly associate *Baiap2l2* with a strong auditory phenotype. However, hearing deficits are not always directly linked to hair cell or hair bundle dysfunction: mutations in *GJB2*, which encodes a gap junction channel connexin 26 expressed in cochlear supporting cells but not hair cells (Zhao and Yu, 2006), are one of the most common causes of hereditary deafness (Carpena and Lee, 2018). Thus, further evidence was needed to tie the auditory phenotype associated with *Baiap2l2* to hair cells and the bundle. RNA sequencing of isolated mouse hair cells from the auditory and vestibular organs identified *Baiap2l2* as a hair cell marker, and revealed that *Baiap2l2* is enriched in cochlear and utricular hair cells (Scheffer *et al.*, 2015). Further, the RNA sequencing analysis indicates that *Baiap2l2* peaks relatively early in both cochlear and utricular hair cells during development of the bundle, around P4, which coincides with the widening of the stereocilia in rows 1 and 2 (Tilney *et al.*, 1992; Krey *et al.*, 2020) (Fig. 1-1C). In the cochlea, *Baiap2l2* was no longer detected at P16 (Scheffer *et al.*, 2015).

While the RNA sequencing data shows that there is *Baiap2l2* expression in the neuroepithelial tissue of the organ of Corti (Scheffer *et al.*, 2015), *in situ* hybridization analysis of mouse tissues has also demonstrated *Baiap2l2* expression in the kidneys and intestines. BAIAP2L2 protein was also localized at the plasma membrane in regions of cell-cell contact by immunohistochemistry of Caco-2 cultures, a human epithelial cell line derived from colon carcinoma (Pykalainen *et al.*, 2011). However, the localization of BAIAP2L2 in the organ of Corti was unknown. Work in this dissertation demonstrated that BAIAP2L2 is a stereocilia protein that concentrates at the tips of the transducing stereocilia, rows 2 and 3, as shown by immunolocalization experiments in Chapter 2. This finding was replicated by another group (Yan *et al.*, 2022), and the mechanisms behind BAIAP2L2's concentration at the tips of transducing stereocilia are explored in Chapter 3.

I-BAR domain proteins bind membranes.

BAIAP2L2 belongs to a subcategory of the Bin/Amphiphysin/Rvs (BAR) domain family of proteins, the inverse-BAR (I-BAR) domain family proteins. BAR domain proteins are multi-effector scaffolding proteins defined by the presence of the eponymous BAR domain (Fig. 1-2A, B), a helical bundle that self-associates to form anti-parallel dimers (Carman and Dominguez, 2018). The BAR domain is responsible for membrane binding, and is associated with curved membranes around cellular structures such as microvilli (Postema *et al.*, 2018; Gaeta *et al.*, 2021), filopodia (Millard *et al.*, 2005; Mattila *et al.*, 2007), and tubules (Takei *et al.*, 1999). The question of whether BAR domain membrane binding either senses pre-existing curvature or induces curvature may be best answered by energetics:

BAR domains can induce curvature in the membranes they bind if the difference between the energy required to bind flat or curved membranes is greater than the energy needed to deform and curve the membrane (Peter *et al.*, 2004). I-BAR domains have a convex membrane-binding surface (Millard *et al.*, 2005), and thus, most members of the I-BAR domain subfamily are thought to bind regions of negative curvature (Saarikangas *et al.*, 2009) (Fig. 1-2A). The I-BAR domain of BAIAP2L2 associates with planar membranes and generates regions of relatively flat membrane (Pykalainen *et al.*, 2011) (Fig. 1-2B), although the I-BAR domains of the most closely related proteins BAIAP2 (IRSp53) and BAIAPL1 (IRTKS), which each share ~30% amino acid sequence identity with BAIAP2L2's I-BAR domain, can induce tubulation when binding to the inner leaflet of the membrane (Saarikangas *et al.*, 2009).

The tips of the transducing stereocilia are beveled, angled towards the taller rows, and covered by planar membrane (Rzadzinska *et al.*, 2004) (Figs. 1-1A, 1-2C). While much of the asymmetric shape can be attributed to gradations in the lengths of the actin filaments constituting the cores of the transducing stereocilia due to active remodeling of the actin, some is the result of "tenting" as force exerted by the tip link pulls the membrane away from the cytoskeleton (Assad *et al.*, 1991) (Fig. 1-2C). Tenting requires deformation of the membrane, which may or may not be static (Pickles *et al.*, 1991; Powers *et al.*, 2012). BAR domains, as discussed above, are certainly capable of inducing membrane deformation, although it is not known if the membrane deformation involved in tenting at stereocilia tips requires any other force beyond what is exerted by the tip link. Intriguingly, the *BAIAP2L2* variant (Val169Ala) identified by whole exome sequencing of patients with hearing loss affects a residue within the I-BAR domain of BAIAP2L2 (Mutai *et al.*, 2022), suggesting that BAIAP2L2's membrane binding capacity may prove crucial for bundle development and/or function.

Regulation of actin effectors by I-BAR proteins.

In addition to their membrane-binding properties, BAR proteins are strongly associated with regulation of the actin cytoskeleton (Zhao *et al.*, 2011; Carman and Dominguez, 2018). As scaffolding molecules, BAR proteins have a modular structure that typically includes several protein binding motifs in addition to their characteristic membrane-binding domain. BAIAP2L2 and the closely related BAIAP2 and BAIAP2L1 all feature an Src Homology 3 (SH3) domain and a WASP Homology 2 (WH2)-like domain (Fig. 1-2B). The presence of an SH3 domain, which recognizes and binds to proline-rich motifs (Kurochkina and Guha, 2013), is frequently associated with the recruitment of actin effectors such as members of the Arp2/3 complex or formins (Carman and Dominguez, 2018). WH2 domains bind monomeric actin (Paunola *et al.*, 2002) and can act as a sink for actin monomers before monomers are incorporated into filaments. Indeed, BAIAP2 has been implicated in several processes involving actin-based protrusions, including the formation of filopodia (Yamagishi *et al.*, 2004; Millard *et al.*, 2005) and dendritic spines (Choi *et al.*, 2005). Similarly, BAIAP2L1 elongates microvilli in mouse small intestinal organoids, which model the epithelium of the enterocyte brush border (Postema *et al.*, 2018).

Like filopodia and microvilli, stereocilia are actin-based protrusions. Accordingly, the regulation of actin is crucial during development of the hair bundle, as evidenced by the observation that a significant subset of proteins discovered by mass spectrometry analysis of isolated bundles interact with actin (Drummond *et al.*, 2012; Shin *et al.*, 2013; Wilmarth *et al.*, 2015). Several aspects of actin growth must be considered during bundle development (Fig. 1-1C). First, the cell must generate its lawn of microvilli—while the precise genesis of the hair cell's microvilli appears somewhat nebulous, there is evidence that puncta of EPS8 and BAIAP2L1 mark the sites of nascent microvilli in intestinal tissues (Gaeta *et al.*, 2021). During the elongation phases, F-actin must continue to be polymerized. During the widening phase, new actin filaments must be added to the stereocilia, and bundled together with the existing core of the stereocilium. These activities must work together to ensure consistent packing density of actin filaments within the stereocilia and that the developing stereocilia reach their appropriate dimensions.

Considering that hair bundle development relies on the progressive sculpting of the stereocilia's F-actin cores into their final structure, and that other BAR-domain containing proteins participate in the formation and regulation of numerous actin-based cellular structures, we hypothesized that BAIAP2L2 activity in bundles may contribute to shaping the F-actin core. As the level of *Baiap2l2* transcripts appears to peak at P4, when stereocilia are in their widening phase, we further hypothesized that BAIAP2L2 activity could be linked to the widening step of bundle assembly. To that end, Chapter 2 examines the morphology of *Baiap2l2*-knockout stereocilia by measuring their widths and heights and comparing them against those of their wild-type or heterozygote counterparts. Scanning electron microscopy is also used to examine bundle morphology in Chapter 2.

As BAR domain family proteins typically act as scaffolds to cluster interacting proteins, their actin-regulating activity is often indirect, although some BAR domain proteins do contain actin-binding motifs such as BAIAP2L2's WH2-like domain. The effects on actin dynamics are instead generally mediated in conjunction with other molecules. Examination of the other proteins associated with a given BAR domain protein provides further context to their activities within a cell. BAIAP2L2's interactome is partially investigated in Chapter 2, by testing for in vitro binding against a panel of bundle proteins, most of which have been previously demonstrated to interact with either BAIAP2 or BAIAP2L1, including EPS8. In Chapter 3, the BAIAP2L2-EPS8 interaction is explored in greater detail, using proximity ligation (Soderberg *et al.*, 2006) to assay protein-protein interactions in vivo and nanoscale pulldown (Bird *et al.*, 2017) to assess protein-protein binding in intact cells.

Transduction modulates hair bundle morphology.

The sculpting of the stereocilia's F-actin cores into their mature structure is controlled by several known factors and is likely further influenced by several unknown factors. Of the known factors, the MYO15A-EPS8 complex labels all stereocilia tips regardless of row early during development (Tadenev *et al.*, 2019) (Fig. 1-3A). In later stages of development, the MYO15A-EPS8 complex also binds a module of WHRN-GPSM2-GNAI; this expanded complex enriches specifically at the tips of row 1 in mature bundles (Fig. 1-3A). Bundles from mice where any of the members of the expanded MYO15A-EPS8 complex are missing share a phenotype in which all the stereocilia are very short and stubby, from which it has been concluded that this complex mediates the elongation of row 1 in addition to setting its identity (Probst *et al.*, 1998; Mburu *et al.*, 2003; Zampini *et al.*, 2011; Tadenev *et al.*, 2019). Similarly, the shorter rows of stereocilia have a set of characteristic molecules that concentrate at their tips: row 2 stereocilia tips are marked by the actin capping proteins CAPZB (Avenarius *et al.*, 2017), EPS8L2 (Furness *et al.*, 2013), and TWF2 (Peng *et al.*, 2009), among others. Morphological phenotypes of bundles lacking these row 2 molecules are not nearly as homogeneous as those for lacking the row 1 complex members, but nonetheless share alterations in stereocilia dimensions that most prominently affect the shorter transducing rows.

Interestingly, the localization of several bundle molecules shifts in the absence of transduction (Fig. 1-3B). MYO15A and EPS8 localization effectively reverts to the immature state of labelling all stereocilia tips if transduction is blocked pharmacologically, or fails to enrich selectively in row 1 if transduction has been genetically ablated through mutations in the pore-forming constituents of the transduction channel (Krey *et al.*, 2020). However, WHRN, GPSM2 and GNAI, which are later additions to the row 1 complex, remain enriched at row 1 tips under those same conditions (Krey *et al.*, 2020). These observations lead to the conclusion that the localization of MYO15A-EPS8 must be influenced by aspects of the transduction current. Similarly, CAPZB, EPS8L2 and TWF2 also fail to enrich at the tips of row 2 in the absence of transduction, and instead distribute more broadly throughout the bundle (Krey *et al.*, 2020) (Fig. 1-3B). As localization of these proteins and complexes is driven by transduction, then their actin-molding activity (or at least the location of their activity) is also driven by transduction (Fig. 1-3D). Rather direct evidence for this is the observation that the number of available F-actin barbed ends decreases in the absence of transduction, implying that ion influx through channels inhibits capping of the barbed ends (McGrath *et al.*, 2021). Relatively short periods without transduction can accordingly produce dramatic changes to the morphology of the bundle. When cochlear explants are cultured in the presence of transduction blockers, the transducing rows of both outer and inner hair cells shorten significantly and bundle morphology appears to regress to a more immature state (Velez-Ortega *et al.*, 2017; Krey *et al.*, 2020). If the transduction blockers are removed, the shortened stereocilia can recover to their original lengths after an additional day in culture (Velez-Ortega *et al.*, 2017). The apparent plasticity of the stereocilia's actin core suggests that the mature bundle may not be static once development is complete but instead likely relies on constant input through active transduction channels to maintain its shape and structure.

Although it has been shown that Ca^{2+} mediates the remodeling of actin in response to changes in transduction state (Velez-Ortega *et al.*, 2017), the mechanisms through which the transduction current influences the localization of the bundle's actin-regulatory complexes and their attendant effects on the underlying actin structure of the bundle are still largely unclear. As EPS8 demonstrably shifts its localization in response to changes in transduction, Chapter 3 builds on a BAIAP2L2-EPS8 interaction identified in Chapter 2 to examine if BAIAP2L2 localization is also linked to transduction. Chapter 3 tests the effect of pharmacological transduction block or genetic ablation of various channel components on BAIAP2L2 localization in the bundle. Chapter 3 also tests the effect of modulating Ca^{2+} levels on the membrane-binding activity of BAIAP2L2's I-BAR domain to propose a mechanism by which Ca^{2+} entering through open transduction channels may directly modulate the protein environment at stereocilia tips.

Overall goals

The overall goal of this dissertation is to examine the contributions of BAIAP2L2 to hair bundle development in the mouse. Chapter 2 describes the characterization of two *Baiap2l2* mouse knockouts, which reveals that the loss of *Baiap2l2* causes progressive deafness, and provides initial insights into the interactome of BAIAP2L2. Chapter 3 examines how BAIAP2L2 is targeted within the hair bundle, demonstrating that BAIAP2L2 relies on active transduction currents to remain localized at stereocilia tips, and identifying Ca^{2+} as the specific factor required for that maintenance. Chapter 4 further discusses the results and conclusions of the preceding chapters, describes the preliminary results of several related experiments, and lastly suggests some further lines of inquiry for investigating BAIAP2L2 in the hair bundle.

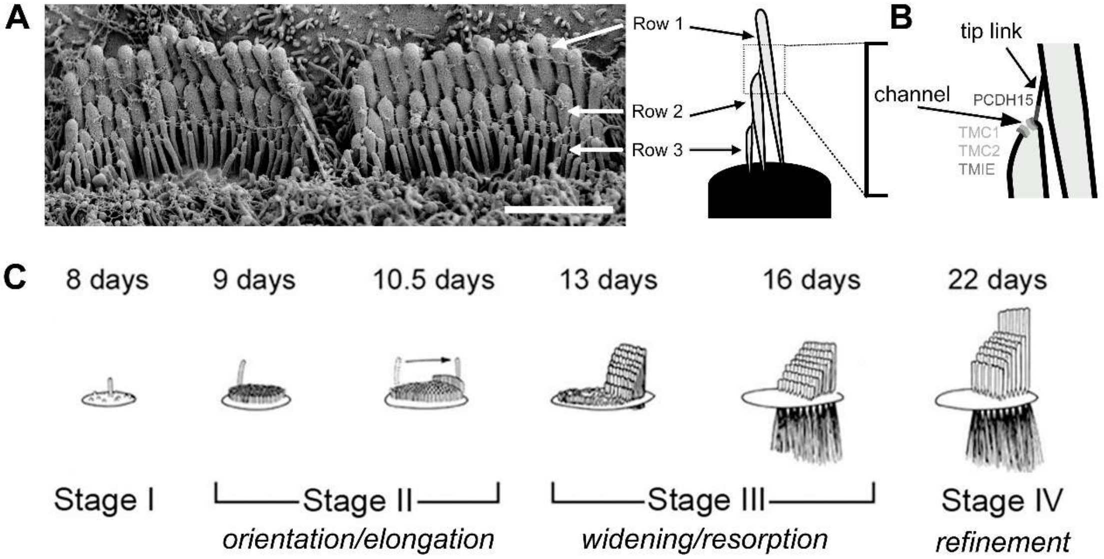

Figure 1-1. Hair bundles are stereotyped structures whose assembly follows distinct steps. (A) Inner hair cell bundles from a P9 C57BL/6J mouse visualized by scanning electron microscopy (SEM). To familiarize the reader with how bundles are described throughout this work, rows of stereocilia are labeled from tallest (row 1) to shortest (row 3), and a schematic shows a bundle in cross section with the same labeling of rows. Image courtesy of Paroma Chatterjee. Scale, 2 µm. (B) Simplified schematic of the transduction channel's gating mechanism. Selected components of the transduction apparatus are highlighted; TMC1, TMC2, and TMIE constitute pore-forming units of the transduction channel, while PCDH15 forms the lower half of the tip link. Mouse mutants of these components are examined in Chapter 3. (C) Progression of hair bundle development, as observed in embryonic chick cochlea. Notably, bundle development proceeds by following similar stages in mammals. Reproduced with permission from (Tilney *et al.*, 1992).

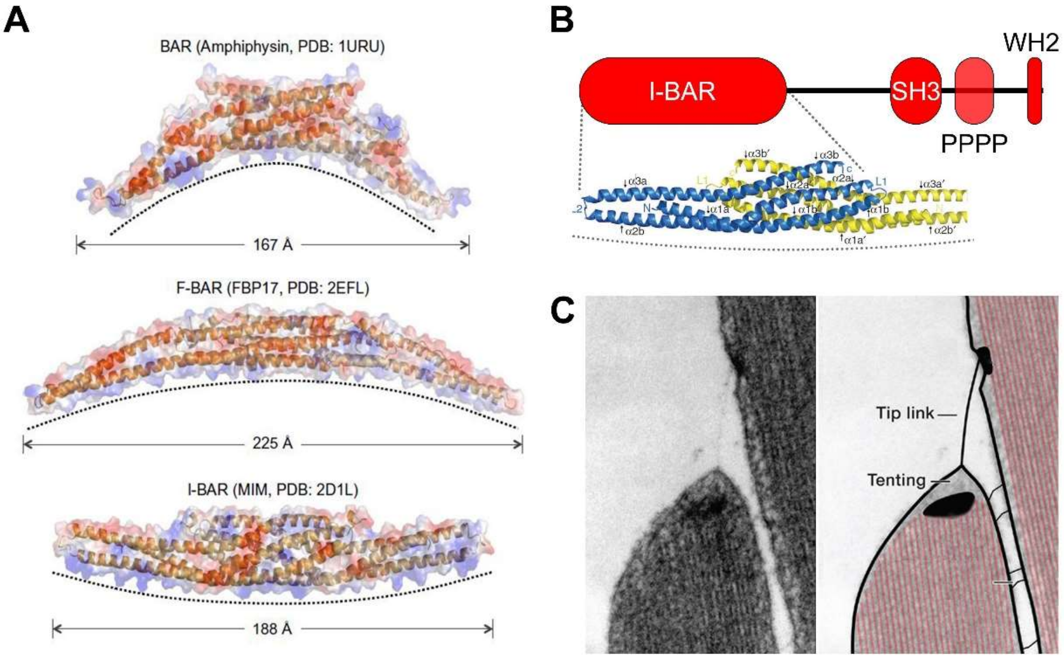

Figure 1-2. BAIAP2L2 belongs to the I-BAR subfamily of BAR domain proteins.

(A) Structures of BAR domains from representative members of the major subfamilies. Electrostatic surfaces are superimposed over diagrams of component alpha-helices, and likely membrane binding surfaces are indicated by dotted lines. Scale indicates dimensions of the BAR dimers. Reproduced with permission from (Carman and Dominguez, 2018). (B) Line schematic of BAIAP2L2 protein domains, with structure of dimerized I-BAR domain, reproduced with permission from (Pykalainen *et al.*, 2011). Length of full dimer is 164 Å. Likely membrane binding surface indicated by dotted line. In line schematic of entire BAIAP2L2 protein, “PPPP” indicates a proline-rich motif. (C) Transmission electron micrograph of a stereocilia pair with evident membrane tenting. Image courtesy of R.A. Jacobs and A.J. Hudspeth, reproduced with permission from (Gillespie and Muller, 2009).

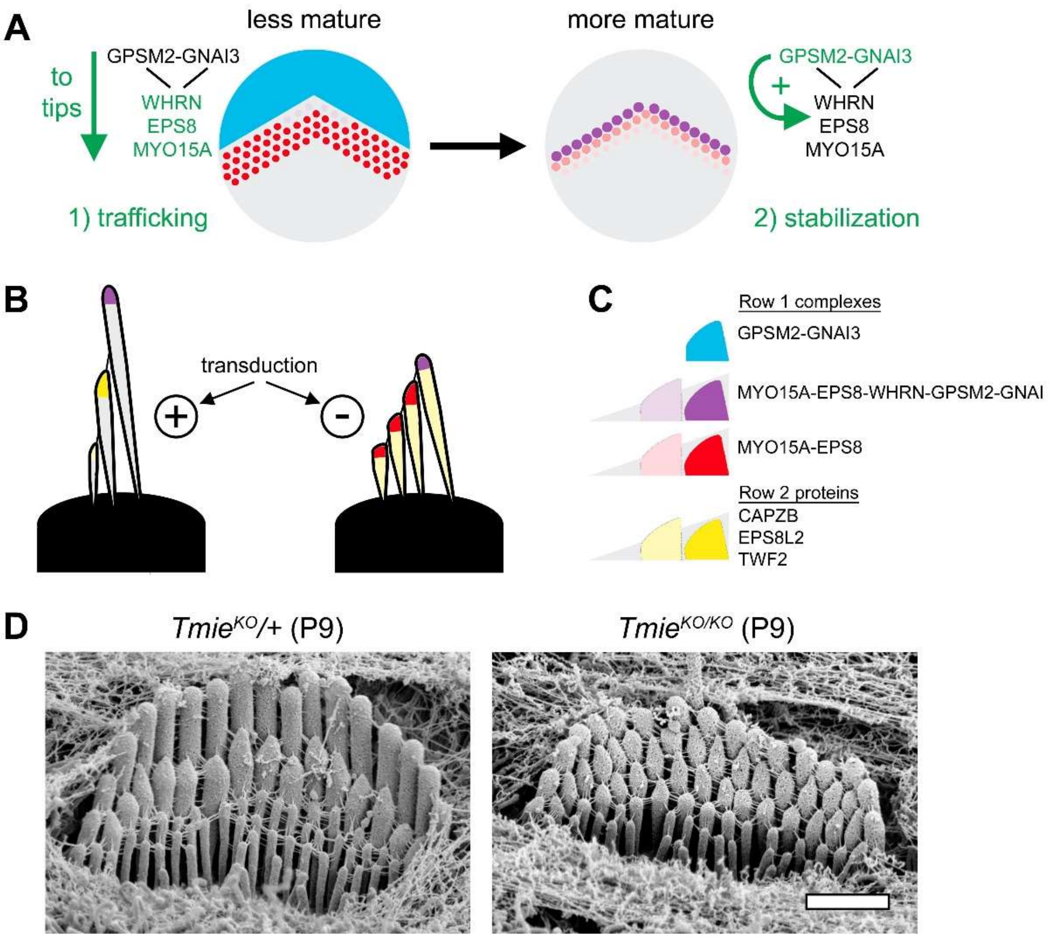

Figure 1-3. Transduction shapes hair bundles.

(A) Schematic of targeting model for MYO15A-EPS8. Early in development, all stereocilia tips are targeted by a MYO15A-EPS8 complex (trafficking phase), while GPSM2-GNAI3 is concentrated in the region apical to the hair bundle (bare zone). At later ages, as transducer currents develop, MYO15A-EPS8, with WHRN, enriches primarily at row 1 tips, where it is stabilized by GPSM2-GNAI3 (stabilization phase). Note that row 2 proteins are present at row 2 tips even though they are not explicitly labelled as such in the stabilization phase bundle; this schematic is intended to track changes in row 1 proteins over development. Figure modified from Tadenev *et al.*, 2019 with permission. (B) Schematic of protein localization in bundles with or without transduction. In the absence of transduction, most row 1 proteins label all tips, but row 2 protein labelling spreads out across the shafts of the entire bundle. (C) Legend for bundle tip proteins shown in A and B. (D) Inner hair cell bundles from P9 *Tmie*$^{KO/+}$ and P9 *Tmie*$^{KO/KO}$ mice visualized by scanning electron microscopy (SEM). TMIE, as noted in Fig. 1-1B, forms part of the transduction channel's pore. Thus, *Tmie* mutants are transduction deficient. Other mouse mutants affecting the transduction channel share the phenotype observed here, where the bundle's staircase is shallower with rows of more uniform width, demonstrating the effect the transduction current has on the bundle's underlying actin structure. Images courtesy of Paroma Chatterjee. Scale, 1 μm.

Chapter 2 – Loss of *Baiap2l2* destabilizes the transducing stereocilia of cochlear hair cells and leads to deafness

Adam J. Carlton[1,2,#], Julia Halford[3,#], Anna Underhill[1,2], Jing-Yi Jeng[1,2], Matthew R. Avenarius[3,6], Merle L. Gilbert[3,7], Federico Ceriani[1,2], Kimimuepigha Ebisine[4], Steve D. M. Brown[4], Michael R. Bowl[4,8], Peter G. Barr-Gillespie[3,5,*], Walter Marcotti[1,2,*]

[1]*Department of Biomedical Science, University of Sheffield, Sheffield, S10 2TN, UK*
[2]*Neuroscience Institute, University of Sheffield, Sheffield, S10 2TN, UK*
[3]*Oregon Hearing Research Center & Vollum Institute, Oregon Health & Science University, Portland, OR 97239, USA*
[4]*Mammalian Genetics Unit, MRC Harwell Institute, Oxfordshire, UK*
[5]*Oregon Hearing Research Center, Mail Code L335A, Oregon Health & Science University, Portland, OR 97239, USA*
[6]Present address: *Department of Pathology, Wexner Medical Center, The Ohio State University, Columbus, OH 43210, USA*
[7]Present address: *US Army Medical Department Activity-Korea, Camp Humphreys, Republic of Korea*
[8]Present address: *UCL Ear Institute, University College London, London, WC1X 8EE.*
[#]Joint first Authors

[*]Joint corresponding authors:
Walter Marcotti (*w.marcotti@sheffield.ac.uk*)
Peter Barr-Gillespie (*gillespp@ohsu.edu*)

This work was published in the Journal of Physiology, February 15, 2021; 599 (4).

Figure Attributions

Fig. 2-1. (A) The *Baiap2l2*^{tm1b} allele was propagated by S.D.M.B. and M.R.B. (B). The *Baiap2l2*$^{\Delta 16}$ allele was generated by M.R.A. and M.L.G.

Fig. 2-2. ABR data collection was performed by W.M., and ABR analysis was performed by F.C.

Fig. 2-3. DPOAE data collection was performed by W.M., and ABR analysis was performed by F.C.

Fig. 2-4. BAIAP2L2 immunostaining was performed by J.H. and J.-Y.J. J.H. contributed panels (A) & (F); J.-Y.J. contributed panels (B-E)

Fig. 2-5. BAIAP2L2/EPS8 immunostaining was performed by J.-Y.J.

Fig. 2-6. SEM images produced by A.U.

Fig. 2-7. Bundle dimensions were measured by J.H.

Fig. 2-8. Transducer currents were measured by A.J.C. and analyzed by W.M. (A-J, N,O). FM1-43 uptake assay was performed by J.H. (K-M).

Fig. 2-9. IHC basolateral membrane properties were measured by A.J.C. and analyzed by W.M.

Fig. 2-10. OHC basolateral membrane properties were measured by A.J.C. and analyzed by W.M.

Fig. 2-11. J.H. performed *in vitro* pulldown assays.

Fig. 2-12. EPS8 immunostaining in *Baiap2l2*^{tm1b} performed by J.-Y.J. (A, B). ESPNL immunostaining in *Baiap2l2*$^{\Delta 16}$ performed by JH (C, D). BAIAP2L2 immunostaining in *Espnl*^{KO} performed by J.H. (E, F). BAIAP2L2 immunostaining in *Eps8*^{KO} performed by J.-Y.J. (G, H). EPS8/BAIAP2L2 immunostaining in *Myo15a*^{sh2} performed by J.H. (I, J).

Key Points Summary

- Mechanoelectrical transduction at auditory hair cells requires highly specialized stereociliary bundles that project from their apical surface forming a characteristic stair-case structure.
- The morphogenesis and maintenance of these stereociliary bundles is a tightly regulated process requiring the involvement of several actin-binding proteins, many of which are still unidentified.
- We have identified a new stereociliary protein, the I-BAR protein BAIAP2L2, which localises to the tips of the shorter transducing stereocilia in both inner and outer hair cells (IHCs and OHCs).
- We found that *Baiap2l2* deficient mice lose their 2nd and 3rd rows of stereocilia, their MET current, and develop progressive hearing loss, becoming deaf by 8 months of age.
- We also demonstrated that BAIAP2L2 localization to stereocilia tips is dependent on the motor protein MYO15A and its cargo EPS8.
- We propose that BAIAP2L2 is a new key protein required for the maintenance of the transducing stereocilia in mature cochlear hair cells.

Abstract

The transduction of sound waves into electrical signals depends upon mechanosensitive stereociliary bundles that project from the cochlear hair cell's apical surface. The height and width of these actin-based stereocilia is tightly regulated throughout life to establish and maintain their characteristic staircase-like structure, which is essential for normal mechanoelectrical transduction. Here, we show that BAIAP2L2, a member of the I-BAR protein family, is a newly identified hair bundle protein that is localized to the tips of the shorter rows of transducing stereocilia in mouse cochlear hair cells. BAIAP2L2 was detected by immunohistochemistry from postnatal day 2.5 (P2.5) throughout adulthood. In *Baiap2l2* deficient mice outer hair cells (OHCs), but not inner hair cells (IHCs), began to lose their 3rd row of stereocilia and showed a reduction in the size of the mechanoelectrical transducer current from just after P9. Over the following post-hearing weeks, the ordered staircase structure of the bundle progressively deteriorates, such that by 8 months of age both OHCs and IHCs of *Baiap2l2* deficient mice have lost most of the 2nd and 3rd rows of stereocilia and become deaf. We also found that BAIAP2L2 interacts with other key stereociliary proteins involved in normal hair bundle morphogenesis such as CDC42, RAC1, EPS8 and ESPNL. Furthermore, we show that BAIAP2L2 localization to the stereocilia tips depends on the motor protein MYO15A and its cargo EPS8. We propose that BAIAP2L2 is key to maintenance of the normal actin structure of the transducing stereocilia in mature mouse cochlear hair cells.

Abbreviations: IHC: inner hair cells; OHC: outer hair cells; PD: postnatal day; MET current: mechanoelectrical transducer current; ABR: auditory brainstem responses; DPOAE: distortion product otoacoustic emission; I-BAR: Inverse bin-amphiphysin-Rvs protein; BAIAP2L2: brain-specific angiogenesis inhibitor 1-associated protein 2-like protein 2; PSF: point spread function.

Introduction

The perception of sound depends on the transduction of acoustic information into electrical signals by the sensory hair cells, which requires the opening of mechanically gated ion channels (Fettiplace and Kim, 2014). The hair bundles of cochlear inner and outer hair cells (IHCs and OHCs) consists of three rows of stereocilia, which are cross-linked by several types of extracellular links (Tilney *et al.*, 1992; Goodyear *et al.*, 2005; Velez-Ortega and Frolenkov, 2019). In the mammalian cochlea, these mechanoelectrical transducer (MET) channels are located at the tips of the middle and shorter rows of the stereociliary hair bundle that protrude from the apical surface of the hair cells. Stereocilia have a tightly packed and uniformly polarized actin cytoskeletal core (Tilney *et al.*, 1992; Bartles, 2000). The length of stereocilia is scaled precisely to form the characteristic staircase-like structure of the hair bundle (Barr-Gillespie, 2015). The growth of stereocilia is so tightly regulated that their height within each row is similar not only within a single hair bundle, but also between adjacent bundles, and changes depending on location along the tonotopic axis of the cochlea (Tilney *et al.*, 1992; Manor and Kachar, 2008; Petit and Richardson, 2009). This indicates a sophisticated level of control over the lengthening and widening of stereocilia, which in altricial rodents mainly occurs during late embryonic and early postnatal stages (Roth and Bruns, 1992; Kaltenbach *et al.*, 1994; Zine and Romand, 1996) and involves several actin-binding proteins and unconventional myosin motors (Barr-Gillespie, 2015; Velez-Ortega and Frolenkov, 2019).

One well characterized mechanism regulating the lengthening of stereocilia involves an extended protein complex, where the motor MYO15A (short isoform (Fang *et al.*, 2015)) is required to transport the scaffolding protein whirlin (WHRN) (Belyantseva *et al.*, 2005) and G-protein signal modulator 2 (GPSM2) and inhibitory G protein alpha (GNAI) (Tadenev *et al.*, 2019) to the stereocilia tips. MYO15A-whirlin regulation of stereocilia length also requires interaction of the complex with epidermal growth factor receptor substrate 8 (EPS8) (Manor *et al.*, 2011). EPS8 is an actin-regulatory protein with actin bundling and cross-linking activity (Croce *et al.*, 2004; Hertzog *et al.*, 2010); in the cochlea, it is primarily located at the tips of tallest row of stereocilia in both OHCs and IHCs (Furness *et al.*, 2013). In the absence of the protein, the stereocilia of cochlear hair cells fail to elongate, leading to deafness in both mice (Zampini *et al.*, 2011) and humans (Behlouli *et al.*, 2014). The EPS8 family-related protein EPS8L2, which is also endowed with actin-binding activity (Offenhauser *et al.*, 2004), is mainly expressed at the tip of the shorter rows of stereocilia. *Eps8l2* knockout mice develop a late-onset, progressive hearing loss that is caused by the gradual loss of the shorter rows of stereocilia (Furness *et al.*, 2013). The exact mechanism by which these proteins are segregated between the rows of stereocilia, and whether additional key proteins are involved in this segregation, is currently unknown.

The I-BAR (Inverse bin-amphiphysin-Rvs) protein family consists of five members: IRSp53 (also known as BAIAP2), IRTKS (BAIAP2L1), FLJ22582 (BAIAP2L2 or Pinkbar), MIM (MTSS1) and ABBA (MTSS1L) (Ahmed *et al.*, 2010). I-BAR proteins are generally able to detect and induce negative membrane curvature[1] (Zhao *et al.*, 2011) by dimerising and binding to acidic phospholipids (Ahmed *et al.*, 2010) via their N-terminal BAR domain. All members of the family also possess a C-terminal WH2 domain (Wiskott-Aldrich homology 2 (Zhao *et al.*, 2011)) which binds globular actin (Lee *et al.*, 2007; Saarikangas *et al.*, 2008). In addition, BAIAP2, BAIAP2L1, and BAIAP2L2 possess a central SH3 domain[2] (Ahmed *et al.*, 2010), which is capable of recruiting actin effector proteins including EPS8

---

[1] While not in original publication, see Fig. 1-2A for the relationship between BAR domain structure and preferred membrane curvature.

[2] See Fig. 1-2B for a schematic of BAIAP2L2's structure and domains.

(Postema *et al.*, 2018), mDia1 (Goh *et al.*, 2012) and WAVE2 (Suetsugu *et al.*, 2006). The ability of I-BAR proteins to localise EPS8 in the gut to regulate actin based protrusions, such as microvilli growth (Postema *et al.*, 2018) and filopodia dynamics (Sudhaharan *et al.*, 2016), suggests that the I-BAR proteins may possess a role in stereocilia morphogenesis and/or maintenance via EPS8 targeting. In particular, BAIAP2L2 binds to actin via its C-terminal WH2 domain (Lee *et al.*, 2007), and it has been identified as a hair cell protein using RNAseq (Scheffer *et al.*, 2015; Zhu *et al.*, 2019), and as a novel hearing loss gene in mice (Bowl *et al.*, 2017). A recent genome-wide association study (GWAS) has also provided a link between *Baiap2l2* and hearing pathology in humans (Wells *et al.*, 2019), indicating the crucial role of this gene in hearing function.

Here, we generated two *Baiap2l2* knockout mouse lines and studied the structure and physiology of the stereociliary bundles of cochlear hair cells. In the absence of BAIAP2L2, the hair bundles of OHCs and IHCs progressively lose their transducing stereocilia row, leading to a rapid increase of hearing thresholds. By 8 months of age, *Baiap2l2* deficient mice were deaf. The hair cells' basolateral membrane characteristics were not affected by absence of BAIAP2L2. We also found that BAIAP2L2 was specifically localized at the tip of the shorter rows of stereocilia, especially row 2, in cochlear hair cells from just after birth up to adult ages in mice. We showed that BAIAP2L2 interacted with CDC42, RAC1, EPS8, and ESPNL, which are known to be essential for the normal morphogenesis and maintenance of the stereociliary bundles. The localization of BAIAP2L2 to the stereocilia tip requires both the actin-regulator protein EPS8 and the motor protein MYO15A. We propose that MYO15A, EPS8 and BAIAP2L2 are part of a stereociliary protein complex involved in the maintenance of the transducing stereocilia in the adult hair cells.

Materials and Methods

Ethics statement

In the UK, all animal work was performed at the University of Sheffield (UK) and licensed by the Home Office under the Animals (Scientific Procedures) Act 1986 (PPL_PCC8E5E93) and was approved by the University of Sheffield Ethical Review Committee (180626_Mar). For *in vitro* experiments mice were killed by cervical dislocation followed by decapitation. For *in vivo* auditory brainstem responses (ABRs) and distortion product otoacoustic emissions (DPOAEs) mice were anesthetized using intraperitoneal injection of ketamine (100 mg/Kg body weight, Fort Dodge Animal Health, Fort Dodge, USA) and xylazine (10 mg/Kg, Rompun 2%, Bayer HealthCare LLC, NY, USA). At the end of the *in vivo* recordings, mice were either culled by cervical dislocation or recovered from anesthesia with intraperitoneal injection of atipamezole (1 mg/Kg). Mice under recovery from anaesthesia were returned to their cage, placed on a thermal mat and monitored over the following 2-5 hrs.

In the USA, all animal procedures were approved by the Institutional Animal Care and Use Committee (IACUC) at Oregon Health & Science University (protocol IP00000714). For *in vitro* experiments, neonatal mice were killed by cervical dislocation followed by decapitation.

In all cases, experiments were carried out according to the guidelines laid down by the University of Sheffield and Oregon Health & Science University animal welfare committees, and conform to the principles and regulations as described in the Editorial by Grundy (2015).

Characterization of *Baiap2l2*^{tm1b} mice

The *Baiap2l2*^{tm1a} allele (EM:07678) was imported from the EMMA repository at Orleans, France. To obtain *Baiap2l2*^{tm1b} animals, cre-mediated conversion of the 'knockout-first' tm1a allele was achieved by treating IVF derived embryos with a cell permeable cre-enzyme (Excellgen). *Baiap2l2*^{tm1b} mice were generated using the C57BL/6N strain, were genotyped using the following primers: wild-type forward primer 5`-CAG ATC CTC AAC ACC AAC GA-3`; knockout forward primer 5`-CCA GTT GGT CTG GTG TCA-3`; reverse primer 5`-TCG GCT CCT TGA TAA AAT GG-3`.

Production of the *Baiap2l2*$^{\Delta 16}$ mutant using CRISPR

The *Baiap2l2* locus was targeted for CRISPR-mediated knockout using guide RNAs (gRNAs) designed to exons 4 and 10 (*http://crispr.mit.edu/*). The gRNA sequences (exon 4, 5'-GCGGCACTTGAACTCAGAC; exon 10, 5'-CAATTCCTTCGGCGAGCGCC) were individually cloned into the DR274 gRNA expression vector (Addgene #42250) and transcribed using the MegaScript T7 kit (ThermoFisher). The in vitro transcribed gRNAs were purified using the NucleoSpin miRNA kit (Macherey-Nagel) and quantified using a NanoDrop spectrophotometer. A mixture containing 30 ng/μl of each gRNA and 110 ng/μl of the Cas9 mRNA (Trilink) was prepared, injected into zygotes, and zygotes implanted into pseudopregnant females. Founders were screened for mutations in the targeted exons as well as for large deletions in the intervening sequence. An out-of-frame mutation in the coding region of exon 4 (c.247_262delCGGCACTTGAACTCAG) that resulted in a premature termination codon (p.Arg83ThrfsTer67) was identified, backcrossed on to the B6 background, and propagated for the experiments described in this study.

Baiap2l2 CRISPR mice (denoted *Baiap2l2*$^{\Delta 16}$) were genotyped using the following primers: wild-type forward primer 5`-CCA GCG GCA CTT GAA CTC AG-3`; wild-type reverse primer 5`-CTG AGA CTC GGC TCC TTG AT-3`; knockout forward primer 5`-GGT TCA GAG CAT CAT GGA GC-3`; knockout reverse primer 5`-ACC TCC AGG TCT GGG TGT GT-3`.

Tissue preparation

Patch clamp recordings were performed from hair cells within the 9-12 kHz region of the cochlear apical coil (Müller *et al.* 2005). The apical coil of wild-type (C57BL) and *Baiap2l2*^{tm1b} mice were dissected out in extracellular solution composed of (in mM): 135 NaCl, 5.8 KCl, 1.3 $CaCl_2$, 0.9 $MgCl_2$, 0.7 NaH_2PO_4, 5.6 D-glucose, 10 HEPES-NaOH. Sodium pyruvate (2 mM), amino acids and vitamins were added from concentrates (Thermo Fisher Scientific, UK). The pH was adjusted to 7.48 with 1 M NaOH (~308 mmol kg^{-1}). The dissected apical coil was then transferred to a microscope chamber, and immobilised via a nylon mesh attached to a stainless steel ring. The chamber (volume 2 ml) was perfused at a flow of about 10 ml h^{-1} from a peristaltic pump and mounted on the stage of an upright microscope (Olympus BX51, Japan; Leica DMLFS, Germany) with Nomarski Differential Interference Contrast (DIC) optics (63x or 60x water immersion objective) and a 15x eyepiece. The microscope chamber was continuously perfused with extracellular solution by a peristaltic pump (Cole-Palmer, UK).

Whole-cell electrophysiology

Inner hair cells (IHCs) and outer hair cells (OHCs) were studied in acutely dissected organs of Corti from postnatal day 6 (P8) to P40 where the day of birth (P0) corresponds to E19.5. Patch clamp recordings were performed at room temperature (20-24°C) using an Optopatch amplifier (Cairn Research Ltd, UK) as previously described (Furness *et al.* 2013; Ceriani *et al.* 2019; Jeng *et al.* 2020a; 2020b). Patch pipettes were pulled from soda glass capillaries and had a typical resistance in extracellular solution of 2-3 MΩ. In order to reduce the electrode capacitance, patch electrodes were coated with surf wax (Mr Zoggs SexWax, USA). The patch pipette intracellular solution contained (in mM): 131 KCl, 3 $MgCl_2$, 1 EGTA-KOH, 5 Na_2ATP, 5 HEPES-KOH, 10 Na-phosphocreatine (pH was adjusted with 1M KOH to 7.28; 294 mmol kg^{-1}). Data acquisition was controlled by pClamp software using Digidata 1440A (Molecular Devices, USA). Recordings were low-pass filtered at 2.5 kHz (8-pole Bessel), sampled at 5 kHz and stored on computer for off-line analysis (Clampfit, Molecular Devices; Origin 2020: OriginLab, USA). For voltage-clamp experiments, membrane potentials were corrected off-line for the residual series resistance R_s after compensation (usually 80%: IHCs 1.2 ± 0.2 MΩ, n = 25; OHCs 1.0 ± 0.1 MΩ, n = 21) and the liquid junction potential (LJP) of –4 mV, which was measured between electrode and bath solutions. Holding currents were plotted as zero current to allow a better comparison between recordings. Voltage clamp protocols are referred to a holding potential of –84 mV or –64 mV depending on the protocol used. Voltage recordings in current clamp were also corrected for the LJP.

For mechanoelectrical transducer (MET) current recordings, the hair bundles of hair cells were displaced using a fluid jet from a pipette driven by a 25 mm diameter piezoelectric disc (Corns *et al.*, 2014; Marcotti *et al.*, 2016; Corns *et al.*, 2018). The pipette was pulled from borosilicate glass to a final overall length of 5.3-5.5 cm. The fluid jet pipette tip had a diameter of 8-10 μm and was positioned near the hair bundles to elicit a maximal MET current. Mechanical stimuli were applied as 50 Hz sinusoids (filtered at 1 kHz, 8-pole Bessel) with driving voltages of up to ± 40 V for OHCs and ± 20 V for IHCs. Prior to the positioning of the fluid jet by the hair bundles, any steady-state pressure was removed by monitoring the movement of debris in front of the pipette. The use of the fluid-jet also allows to efficiently displace the hair bundles in both the excitatory and inhibitory directions, which is essential to perform reliable measurements of the resting open probability of the MET channels (Corns *et al.*, 2014; Marcotti *et al.*, 2016; Corns *et al.*, 2018).

Auditory brainstem responses

Following the onset of anaesthesia (see *Ethics statement* above) and the loss of the retraction reflex with a toe pinch, mice were placed in a soundproof chamber (MAC-3 acoustic chamber, IAC Acoustic, UK). Both male and female mice were positioned onto a heated mat (37°C) with the animal's pinna being positioned at a distance of 10 cm from the loudspeaker. Two subdermal electrodes were placed under the skin behind the pinna of each ear (reference and ground electrode), and one electrode half-way between the two pinna on the vertex of the mouse (active electrode) as previously described (Ingham *et al.*, 2011). Sound stimuli were delivered to the mouse ear by a calibrated loudspeaker (MF1-S, Multi Field Speaker, Tucker-Davis Technologies, USA), which was calibrated with a low-noise microphone probe system (ER10B+, Etymotic, USA). Experiments were performed using a customized software (Ingham *et al.*, 2011) driving an RZ6 auditory processor (Tucker-Davis Technologies). ABR thresholds, which were delivered as clicks and stimulus pure tones of frequencies at 6, 12, 18, 24, 30 and 36 kHz, were defined as the lowest sound level where any recognisable feature of the waveform was visible. Stimulus sound pressure levels were typically 0-95 dB SPL, presented in steps of 5 dB SPL (average of over 256 repetitions). Tone bursts were 5 ms in duration with a 1 ms on/off ramp time, which was presented at a rate of 42.6/sec.

Wave 1 amplitude and latency were measured from ABR recordings obtained by stimulating mice with a pure tone (12 kHz). We selected the 12 kHz value as it is close to the frequency range used for the *in vitro* work. An initial automatic identification of Wave 1 was carried out using a custom software routine based on the *find_peaks* function of the scipy.signal Python module (Python 3.7, Python software foundation) (Virtanen *et al.*, 2020). Results were manually reviewed and, if required, adjusted to the correct peak. The Wave 1 amplitude was calculated as the difference between the amplitude of the first peak and the first trough of the ABR waveform; the latency was calculated as the delay of the Wave 1 peak from the beginning of the recording. Since the distance of the speaker from the animal is 10 cm (see above), this leads to a delay in the signal of ~0.3 ms.

Distortion product otoacoustic emissions

Distortion product otoacoustic emissions (DPOAEs) was used to assess OHC function *in vivo* by the synchronous presentation of two stimulus tones (primaries f1 and f2). DPOAEs were recorded at 2f1-f2 in response to primary tones f1 and f2, where f2/f1 = 1.2. The f2 level (L2) was set from 20 to 80 dB (maximum level set for our system) in 10 dB increments, and the f1 level (L1) was set equal to L2. Frequency pairs of tones between f2 = 6.5 kHz and f2 = 26.3 kHz were presented directly into the left ear canal of mice by means of a coupler, which was connected to two calibrated loudspeakers using 3 cm plastic tubes (MF1-S, Multi Field Speaker, Tucker-Davis Technologies, USA).

Recordings were performed in a soundproof chamber (MAC-3 Acoustic Chamber, IAC Acoustic, UK) and the emission signals were recorded by a low-noise microphone (ER10B+: Etymotic Research Inc, USA) connected to the above-mentioned coupler. Experiments were performed using BioSigRZ software driving an RZ6 auditory processor (Tucker-Davis Technologies). The DPOAE thresholds were defined by the minimal sound level where the DPOAEs were above the standard deviation of the noise. The determined DPOAE thresholds were plotted against the geometric mean frequency of f1 and f2. Stimulus sound pressure levels were typically 0-80 dB SPL, presented in steps of 10 dB. The response signal was averaged over 500 repetitions.

Scanning electron microscopy (SEM)

For SEM, the dissected mouse cochleae were initially fixed by a very gentle intralabyrinthine perfusion using a 10 µl pipette tip through the round window. The fixative contained 2.5% vol/vol glutaraldehyde in 0.1M sodium cacodylate buffer plus 2 mM Ca_2Cl (pH 7.4). After a few minutes, the cochleae were immersed in the above fixative for 2 hrs at room temperature. After the fixation, the organ of Corti was exposed by removing the bone from the apical coil to the cochlea and then immersed in 1% osmium tetroxide in the cacodylate buffer for 1 h. For osmium impregnation, which avoids gold coating, cochleae were incubated in solutions of saturated aqueous thiocarbohydrazide (20 mins) alternating with 1% osmium tetroxide in buffer (2 h) twice (the OTOTO technique (Furness and Hackney, 1986)). The cochleae were then dehydrated through an ethanol series and critical point dried using CO_2 as the transitional fluid (Leica EM CPD300), and mounted on specimen stubs using conductive silver paint (Agar Scientific, Stansted, UK). The apical coil of the organ of Corti was examined at 10 kV using a Tescan Vega3 LMU scanning electron microscope.

Immunofluorescence microscopy

In the UK, the inner ears were dissected and fixed with 4% paraformaldehyde in phosphate-buffered saline (PBS, pH 7.4) for 20 minutes at room temperature. Cochleae were washed three times in PBS for 10 minutes and fine dissected. Samples were incubated in PBS supplemented with 5% normal goat or horse serum and 0.5% Triton X-100 for 1 hour at room temperature. The samples were immunolabelled with primary antibodies overnight at 37˚C, washed three times with PBS and incubated with the secondary antibodies for 1 hour at 37˚C. Antibodies were prepared in 1% serum and 0.5% Triton X-100 in PBS. F-actin was stained with Texas Red-X (1:400, ThermoFisher, T7471) phalloidin within the secondary antibody solution. Primary antibodies were: rabbit-IgG anti-BAIAP2L2 (1:50, Atlas Antibodies, HPA003043), mouse-IgG1 anti-Eps8 (1:1000, BD Biosciences, 610143), mouse-IgG1 anti-BK channel (1:200, NeuroMab, 75-408), mouse-IgG1 anti-CtBP2 (1:50, BD Biosciences, 612044), goat-IgG anti-ChAT (1:500, Millipore, AB144P), rabbit-IgG anti-KCNQ4 (1:100, StressMarq Biosciences, SMC-309), mouse-IgG1 anti-MYO7a (1:100, Developmental Studies Hybridoma Bank, #138-1s), rabbit-IgG anti-MYO7a (1:500, Proteus Biosciences, 25-6790) mouse-IgG2a anti-PSD95 (1:1000, Millipore, MABN68), rabbit-IgG anti-prestin (1:1000, kindly provided by Robert Fettiplace), rabbit-IgG anti-SK2 (1:500, Sigma-Aldrich, P0483). Secondary antibodies were species appropriate Alexa Fluor or Northern Lights secondary antibodies. Samples were mounted in VECTASHIELD (H-1000). The images from the apical cochlear region (8-12 kHz) were captured with Nikon A1 confocal microscope equipped with Nikon CFI Plan Apo 60x Oil objective or a Zeiss LSM 880 AiryScan equipped with Plan-Apochromat 63x Oil DIC M27 objective for super-resolution images of hair bundles. Both microscopes are part of the Wolfson Light Microscope Facility at the University of Sheffield. Image stacks were processed with Fiji ImageJ software.

In the USA, inner ears were isolated from *Baiap2l2* or *Myo15a*^{sh2} mice and wildtype or heterozygote littermates at the indicated ages and dissected in cold Leibovitz's L-15 medium (L-15) supplemented with 5 mM HEPES, pH 7.4. Small openings were made within the periotic bones to allow perfusion of the fixative and the ears were then fixed in 4% formaldehyde in PBS for 1 hour at room temperature. Ears were washed in PBS, then the cochleae were dissected out from the periotic bone and the lateral wall was removed. Cochleae were permeabilized in 0.5% Triton X-100 in PBS for 10 minutes at room temperature. For stereocilia dimension analysis of *Baiap2l2* mice using only phalloidin, ears were then incubated with 0.4 U/mL Alexa Fluor 488 phalloidin in PBS for 3 hours at room temperature. Organs were washed three times in PBS over 15 minutes and then mounted with Vectashield. For immunolabelling, after permeabilization, samples were blocked for 1 hour in PBS supplemented with 5% normal donkey serum. Samples were then incubated overnight at 4°C in the primary antibody solution and washed three times in PBS over 15 minutes. The samples were then incubated in secondary antibody containing solution (donkey anti-rabbit Alexa Fluor 488, donkey anti-mouse Alexa Fluor 568) with phalloidin (0.4 U/mL CF568 phalloidin or 0.8U/mL CF405 phalloidin) for 3 hours at room temperature, washed three times in PBS over 15 minutes, and mounted in Vectashield. Primary antibodies included rabbit anti-BAIAP2L2 (1:200; Abcam ab224323); mouse anti-EPS8 (1:200; BD #610143); and rabbit anti-ESPNL (1:250; Ebrahim et al., 2016). All samples were imaged with a 63x, 1.4 NA Plan-Apochromat objective on a Zeiss Elyra PS.1/LSM710 system equipped with an Airyscan detector and ZEN 2012 (black edition, 64-bit software; Zeiss, Oberkochen, Germany) acquisition software. The full-width at half maximum of the point-spread function (PSF) in the x-y plane was 186 nm; resolution in the z-axis is about three-fold poorer (Krey *et al.*, 2020).

Measurements of stereocilia dimensions

Phalloidin-stained cochleae were imaged such that hair bundles were aligned with the z-axis of the stack, and that x-z reslices showed pairs of stereocilia in profile. Measurements of stereocilia length and width were approximated from stereocilia profiles using Fiji. Reslices were processed for this function by first applying an unsharp mask with a radius of 3 pixels and a mask weight of 0.6, then binarizing the filtered images with a threshold set such that the stereocilia would be discrete. The Analyze Particles function was applied to the resulting binary mask; Show Ellipses was selected, and Fit ellipse was selected in Set Measurements. The major and minor axes of ellipses fit to the processed stereocilia profiles correspond to approximate stereocilia length and width. Because these measurements are deconvolved with the objective's point spread function (PSF), they are approximations of stereocilia dimensions rather than absolute dimensions with errors of ~40% for width and ~15% for length (Krey *et al.*, 2020). However, measurements obtained as described nonetheless demonstrate the relative changes in stereociliary shape that occur throughout development.

FM1-43 uptake

Inner ears were isolated from *Baiap2l2*$^{\Delta 16}$ mice and wildtype or heterozygote littermates at P8.5, and cochleae were dissected in 155 mM NaCl, 6 mM KCl, 3 mM D-glucose supplemented with 5 mM HEPES, pH 7.3 (low Ca^{2+} saline). This nominally Ca^{2+}-free saline contained 1-2 μM Ca^{2+} as measured by atomic absorption (Kachar *et al.*, 2000). Per experiment, 2-3 animals per genotype were used. Intact cochleae were left on the modiolus, with the stria vascularis removed; as measured by FM1-43 loading, transduction persisted for tens of minutes under these conditions. Cochleae were kept on ice in low Ca^{2+} saline prior to pulsing with 6 μM FM1-43 in low Ca^{2+} saline for 30 seconds with agitation to allow dye loading through the apical surface. Under these conditions, FM1-43 labeling assays for MET and not membrane cycling (Meyers *et al.*, 2003). To control for non-specific dye uptake, one cochlea per animal was incubated on ice in low Ca^{2+} saline supplemented with 5 mM 1,2-bis(*o*-aminophenoxy)ethane-*N*,*N*,*N'*,*N'*-tetraacetic acid (BAPTA) to break tip-links and prevent dye entry through the MET channel. After pulsing with FM1-43, organs were washed three times in low Ca^{2+} saline (1-2 minutes per wash) and fixed in 4% formaldehyde in low Ca^{2+} saline for 20 minutes. Fixed organs were washed three times (1-2 minutes per wash) in PBS, mounted in Vectashield, and imaged immediately with a 63x, 1.4 NA Plan-Apochromat objective on the same system described above. Z-stacks for 1-2 fields of view per animal were acquired to capture the apical surface of the hair cells and 2-5 μm deep. To quantify differences in FM1-43 uptake across conditions (with or without BAPTA) and genotypes (*Baiap2l2*$^{\Delta 16}$/+, *Baiap2l2*$^{\Delta 16/\Delta 16}$), signal intensity was measured in Fiji from regions of interest (ROIs) drawn in slices just below (~0.5 μm) the apical surface. FM1-43 uptake was variable across experiments, so single cell intensities were normalized to the average wild-type control (no BAPTA) signal.

Bacterial expression and characterization of recombinant proteins for pull-down assays

BAIAP2L2 domains (N-terminal, aa1-261; C-terminal, aa262-522; SH3, aa323-386) were expressed in *Escherichia coli* BL21(DE3) with an N-terminal GST tag using the pGEX-4T3 vector (GE Healthcare Life Sciences). EPS8, EPS8L1, EPS8L2, ESPNL, CDC42, RAC1 were expressed in *Escherichia coli* BL21(DE3) with N-terminal 6xHis-2xHA tags using a modified pTrcHis2-C vector (Thermo Fisher). To map the binding site for these proteins on BAIAP2L2, constructs of truncated BAIAP2L2 C-terminal domains, with (aa323-522) and without the SH3 domain (aa387-522), were made. Protein expression was induced with the addition of 0.5 mM IPTG, and continued overnight at 25°C. Bacterial extracts were prepared under nondenaturing conditions by first sonicating cells resuspended in PBS supplemented with protease inhibitor cocktail (Sigma Aldrich), and then clarifying the sonicates by centrifugation at 12,000 x g for 30 minutes. Supernatants (clarified bacterial extracts) containing soluble protein were collected, and expression levels were assessed by immunoblotting. For pull-down assays, GST-tagged BAIAP2L2 domains were used as bait proteins. Glutathione Sepharose 4B beads (GE Healthcare Life Sciences) were loaded with GST-tagged proteins by incubation with clarified bacterial extracts for 1 hour at room temperature with rotation followed by three washes in PBS (5 minutes at 500 x *g*). Loaded beads were then incubated with bacterial extracts containing 6xHis-2xHA tagged prey proteins for 1 hour at room temperature with rotation to allow complexes to form. Unbound proteins were washed off (3 times 5 minutes at 500 x g) with PBS. Beads with bound complexes were transferred to spin columns, and incubated for 10 minutes in hot 2X LDS (Thermo Fisher Scientific) sample buffer before spinning 5 minutes at 1000 x g to elute into 2X reducing agent

(Thermo Fisher Scientific). Eluted samples (20% of total eluate) and input lysates (1% of sample applied to beads) were analysed by immunoblotting, and detected with either rabbit anti-GST or mouse anti-6*His.

Statistical analysis

Statistical comparisons of means were made by Student's two-tailed *t*-test or, for multiple comparisons, analysis of variance (1-way or 2-way ANOVA followed by a suitable post-test). $P<0.05$ was selected as the criterion for statistical significance. Only mean values with a similar variance between groups were compared. Average values are quoted in text and figures as means ± S.D. For DPOAE experiments, due to the presence of "not found" values (i.e. above the upper threshold limit of our equipment), the non-parametric aligned ranks transformation 2-way ANOVA (Mann-Whitney U-test for pairwise comparisons with Bonferroni adjusted P values) statistical test was used (Jeng *et al.*, 2020); data are quoted as median, and first and third quartiles.

Results

Generation of *Baiap2l2* knockout mice

Baiap2l2-deficient mice (*Baiap2l2*^{tm1b}) were produced through Cre-mediated conversion of the ‘knockout-first’ tm1a allele, which was achieved by treating IVF derived embryos with a cell permeable Cre-enzyme (**Fig. 2-1***A*). In the converted tm1b allele, exon 4 (ENSMUSE00000126561) of the *Baiap2l2* gene (ENSMUSG00000018126; MGI:2652819), located on chromosome 15, is deleted leaving a lacZ reporter cassette. Exon 4 encodes part of the I-BAR domain, which is critical for BAIAP2L2 function, and the *lacZ* cassette contains a splice acceptor that subsumes normal splicing (**Fig. 2-1***A*). We also used CRISPR/Cas9 gene editing to generate a mouse line (*Baiap2l2*$^{\Delta 16}$) with a 16 nucleotide deletion in exon 4 (c.247_262delCGGCACTTGAACTCAG p.Arg83Thrfs*67) (**Fig. 2-1***B*). Both transgenic mouse lines (UK: *Baiap2l2*^{tm1b}; USA: *Baiap2l2*$^{\Delta 16}$) showed the same morphological and physiological phenotypes.

Baiap2l2$^{tm1b/tm1b}$ mice exhibit early progressive hearing loss

The hearing sensitivity of *Baiap2l2*^{tm1b} mice was tested using auditory brainstem responses (ABRs). Control mice (*Baiap2l2*$^{tm1b/+}$) had normal thresholds for click at P14 that decreased to even lower sound pressure levels over the first post-hearing week ($P < 0.0001$, Tukey’s post-test, one-way ANOVA), as previously shown in wild-type mice (Song *et al.* 2006), and then remained constant up to at least 245 days of age (about 8 months, $P = 0.1357$, one-way ANOVA) (**Fig. 2-2***A*). *Baiap2l2* knockout littermate mice (*Baiap2l2*$^{tm1b/tm1b}$) exhibited a similar initial decrease in click ABR thresholds ($P < 0.0001$, Tukey’s post-test), but by 2 months of age thresholds were elevated back to levels seen at 14 postnatal days ($P = 0.2185$, Tukey’s post-test). Despite the comparable initial trend, ABR thresholds for clicks were significantly elevated in *Baiap2l2*$^{tm1b/tm1b}$ compared to control mice ($P < 0.0001$, two-way ANOVA, **Fig. 2-2***A*). By 5-8 months of age (**Fig. 2-2***A*: 166-245 days), click ABRs were no longer detected in *Baiap2l2*$^{tm1b/tm1b}$ mice. Pure-tone evoked ABRs (3, 6, 12, 18, 24, 36 kHz) were also found to be significantly elevated at all age-group tested in *Baiap2l2*$^{tm1b/tm1b}$ compared to littermate controls ($P <$ 0.0001 for all ages: two-way ANOVA, **Fig. 2-2***B-C*).

We then analysed the amplitude and latency of the ABR wave 1 at 12 kHz (**Fig. 2-2***D,E*). This frequency was selected because it allows correlation between ABR data and the *in vitro* results, which were performed in the 9-12 kHz frequency range (see below). We found that the amplitude of wave 1 over the overlapping range was significantly reduced in *Baiap2l2*$^{tm1b/tm1b}$ compared to control mice at both age-ranges (range: 50-95 dB SPL, $P <$ 0.0001, Tukey's post-test, two-way ANOVA, **Fig. 2-2***F*, upper panel). Wave 1 latency was significantly increased between the two genotypes at both ages ($P <$ 0.0001, **Fig. 2-2***F*, lower panel). When the latency of wave 1 was plotted as a function of the dB relative to threshold, it was no longer significantly increased in *Baiap2l2*$^{tm1b/tm1b}$ compared to control mice (range: 0-40 dB SPL, $P =$ 0.9677, two-way ANOVA, **Fig. 2-2***G*, lower panel). In contrast, wave 1 amplitude was still significantly different between the two genotypes at both ages (19-22 days: $P <$ 0.0001, 48-53 days: P = 0.0468, Tukey's post-test, two-way ANOVA, **Fig. 2-2***G*, upper panel). Since ABRs wave 1 is generated by the summed response to sound of the afferent nerve fibres innervating the IHCs (Moller and Jannetta, 1982; Schaette and McAlpine, 2011), these results suggested that the loss of BAIAP2L2 is likely to affect the sensory hair cells. Moreover, the increased ABR threshold and the steeper growth of the wave 1 amplitude in the young adult *Baiap2l2*$^{tm1b/tm1b}$ mice (P19-P22, **Fig. 2-2***G*) suggest a possible loss of cochlear compression with increasing stimulus levels, which suggests OHC dysfunction.

To provide a specific readout of OHC function *in vivo*, we recorded distortion product otoacoustic emissions (DPOAEs) (**Fig. 2-3**). DPOAEs are a product of cochlear amplification caused by the displacement of OHC stereociliary bundles during sound stimulation. We found that the DPOAE thresholds over the age-range investigated in *Baiap2l2*$^{tm1b/tm1b}$ mice were raised significantly compared to littermate controls ($P<0.0001$ for all 3 age groups: non-parametric aligned ranks transformation 2-way ANOVA), indicating that OHCs are likely to be dysfunctional.

BAIAP2L2 is localized at the tips of the shorter transducing stereocilia

RNA-seq data has recently shown that in the mouse cochlea *Baiap2l2* is specifically expressed in hair cells within the organ of Corti (https://umgear.org (Kolla *et al.*, 2020)). The exact localization of BAIAP2L2 in the hair cell was investigated using immunofluorescence labelling with two different antibodies (see Methods). BAIAP2L2 expression was already detectable as early as P2.5 (**Fig. 2-4*A***) and persisted in the adult cochlea in both hair cell types (**Fig. 2-4*B-D***), but was absent in hair cells from *Baiap2l2*$^{tm1b/tm1b}$ (**Fig. 2-4*E***) and *Baiap2l2*$^{\Delta16}$ mice (data not shown). Within the OHCs BAIAP2L2 was present in both the second and third rows of stereocilia (**Fig. 2-4*A***), which correspond to the transducing stereocilia (Beurg *et al.*, 2009), whereas in IHCs it only appeared to localize primarily at the tips of the second stereociliary row (**Fig. 2-4*B-D***). When detected with the Abcam antibody, BAIAP2L2 appeared to shift in IHCs during development; while initially concentrated at row 2 tips, BAIAP2L2 localization gradually became more annular and was found along row 2 stereocilia shafts from ~P14 onwards (**Fig. 2-4*F***). The modest differences in apparent localization of BAIAP2L2 in older animals may reflect differential exposure of the distinct antibody epitopes.

BAIAP2L2 localization was different to that of EPS8, which mainly localizes at the tallest row of stereocilia in both young P6-P12 (**Fig. 2-5*A,B***) and adult P113-117 mice (**Fig. 2-5*C,D***). By contrast, BAIAP2L2 had a similar localization to that of EPS8L2; both were found at the tips of rows 2 and 3, the shorter transducing stereocilia (Furness *et al.*, 2013).

Progressive loss of the transducing rows of stereocilia in *Baiap2l2* knockout mice

Because BAIAP2L2 is expressed in stereociliary bundles, we investigated whether its absence caused defects in the normal growth and/or maintenance of the stereocilia in both OHCs and IHCs. Using scanning electron microscopy, we found that at P11 the hair bundles of *Baiap2l2*$^{tm1b/tm1b}$ mice showed a few missing stereocilia in the shorter third row in OHCs, but not in IHCs (**Fig. 2-6***A,B*). A similar phenotype has previously been described in *Eps8l2* knockout mice, but only in the mature cochlea (Furness *et al.*, 2013). At P49, the third row of stereocilia in OHCs was almost completely missing in the *Baiap2l2*$^{tm1b/tm1b}$ mice, while IHCs appeared to have a normal complement of stereocilia (**Fig. 2-6***C,D*). By P245, a time when *Baiap2l2*$^{tm1b/tm1b}$ mice are completely deaf (**Fig. 2-2**), the stereocilia of both OHCs and IHCs lacking BAIAP2L2 were almost exclusively formed by one row of stereocilia and several hair cells were missing in the sensory epithelium (**Fig. 2-6***E,F*). These data indicate that the progression of the stereocilia defects due to the absence of BAIAP2L2 was different between OHCs and IHCs, with the latter being delayed by several weeks. We quantified stereocilia dimensions of P0.5 to P21 IHCs and of P5.5 to P21 OHCs from *Baiap2l2*$^{\Delta 16}$ mice by measuring the apparent length and width of the phalloidin-stained actin cores (Krey *et al.*, 2020). While pairwise comparisons for row dimensions between genotypes at each age yielded several significant differences, no consistent trend in the direction of the differences was observed for either IHCs (**Fig. 2-7***A*-L) or OHCs (**Fig. 2-7***M-T*). We also noted the loss of row 3 stereocilia from P21 *Baiap2l2*$^{\Delta 16}$ mice (**Fig. 7***P,T*), which is in agreement with the above SEM data (**Fig. 2-6**).

Mechanotransducer currents are reduced in *Baiap2l2* knockout mice

Considering that the stereociliary bundles of *Baiap2l2*$^{tm1b/tm1b}$ mice appear to lose the 3rd row of stereocilia prior to the onset of hearing (**Fig. 2-6**), we investigated possible functional changes in the mechanoelectrical transducer (MET) apparatus. MET currents were recorded from P8 to P11 apical coil OHCs (**Fig. 2-8**) by displacing their stereociliary bundles using a 50 Hz sinusoidal force stimulus from a piezo-driven fluid-jet (Corns *et al.*, 2014; Corns *et al.*, 2018). Moving the bundles in the excitatory direction (i.e., towards the taller stereocilia) and at negative membrane potentials elicited a large inward MET current in all OHCs tested at P8-P9 (**Fig. 2-8***A*-*C*), with a maximal value that was not significantly different between control *Baiap2l2*$^{+/tm1b}$ (–915 ± 145 pA $n = 11$, at –124 mV) and littermate *Baiap2l2*$^{tm1b/tm1b}$ mice (–767 ± 327 pA $n = 17$, $P = 0.1711$, *t*-test, **Fig. 2-8***G*). At P11, as expected during development, the MET currents in control OHCs significantly increased (–1200 ± 317 pA $n = 6$, **Fig. 2-8***D,F,G*) compared to early ages ($P = 0.0208$). By contrast, the MET current at P11 of *Baiap2l2*$^{tm1b/tm1b}$ mice was only about half that of littermate controls (–511 ± 131 pA $n = 4$, $P = 0.0036$) (**Fig. 2-8***E*-*G*). This result is consistent with the loss of row 3 stereocilia and their transducer channels. By stepping the membrane potential from –124 mV to more depolarized values in 20 mV increments, the transducer current decreased in size at first and then reversed near 0 mV in both genotypes (**Fig. 2-8***C,F*), consistent with the non-selective permeability of MET channels to cations. Note that the current became outward when excitatory bundle stimulation was applied during voltage steps positive to the reversal potential of the transducer current. The maximal MET current at positive membrane potentials (**Fig. 2-8***H*) was also not significantly different between the two genotypes at P8-P9 (*Baiap2l2*$^{+/tm1}$: +955 ± 206 pA $n = 11$, +96 mV; *Baiap2l2*$^{tm1b/tm1b}$: +805 ± 337 pA $n = 5$, $P = 0.2020$, *t*-test) but highly reduced at P11 (*Baiap2l2*$^{+/tm1b}$: +1484 ± 205 pA $n = 17$; *Baiap2l2*$^{tm1b/tm1b}$: +579 ± 79 pA $n = 4$, $P < 0.0001$).

The resting MET current, which is the current flowing through open transducer channels in the absence of mechanical stimulation, can be measured from the difference between the holding current and the current present during inhibitory bundle deflection. Experimentally, this inhibitory stimulation is obtained when negative driver voltages pull solution into the fluid jet and completely close the MET channel. At negative membrane potentials, the resting current was evident in OHCs from both control (**Fig. 2-8***A,D*, arrowheads) and *Baiap2l2*$^{tm1b/tm1b}$ mice (**Fig. 2-8***B*,E, arrowheads). At positive potentials, the larger resting transducer current (**Fig. 2-8***A,B,D,E*, arrows) is due to an increased open probability of the transducer channel resulting from a reduced driving force for Ca^{2+} influx (Crawford et al. 1989; Corns *et al.* 2014). The resting MET current was represented as a proportion of the total MET current (i.e. resting open probability, P_o) and was similar between the two genotypes at both negative (**Fig. 2-8***I*) and positive (**Fig. 2-8***J*) membrane potentials.

We further tested whether the resting MET current was significantly reduced in adult P8.5 OHCs by using the styryl dye FM1-43, a permeant blocker of the hair cell MET channel that has previously been used to assess the presence of the resting transducer current (Gale *et al.* 2001). Bath application of FM1-43 labelled control OHCs, but dye loading was considerably reduced in *Baiap2l2*$^{\Delta16/\Delta16}$ cells (**Fig. 2-8***K-M*). FM1-43 uptake in OHCs of *Baiap2l2*$^{\Delta16/\Delta16}$ mice was further decreased when the hair bundles were treated with the Ca^{2+} chelator BAPTA (**Fig. 2-8***M*), which is known to break the tip links (Zhao *et al.*, 1996). Considering that the P_o of MET current in OHCs is not affected (**Fig. 2-8***I,J*), these FM1-43 data support the suggestion that loss of BAIAP2L2 does not affect the properties of MET channels but rather reduces the number of transducing stereocilia as shown by the SEM data (**Fig. 2-6**).

In order to verify whether the apparently normal stereociliary bundles of IHCs from young adult *Baiap2l2*$^{tm1b/tm1b}$ mice (**Fig. 2-6***D*) was associated with normal mechanoelectrical transduction, we measured the MET current by displacing their hair bundles as described for OHCs, but only at the holding potential of –84 mV. This more restricted experimental protocol was due to the technically demanding MET current recordings from adult IHCs. Moving the bundles of P19-P28 IHCs in the excitatory direction elicited an inward MET current with a maximal size that was not significantly different between *Baiap2l2*$^{+/tm1b}$ (–358 ± 96 pA n = 16) and littermate *Baiap2l2*$^{tm1b/tm1b}$ mice (–317 ± 84 pA n = 12, P = 0.2486, t-test, **Fig. 2-8*N,O***). No significance was also present for the resting open probability between the two genotypes (P = 0.3229, **Fig. 2-8*O***). These data suggest that the absence of BAIAP2L2 in IHCs, which as for OHCs is expressed from just after birth (**Fig. 2-4**), has a late effect on these cells possibly due to compensatory mechanisms (see Discussion).

Basolateral membrane properties develop normally in *Baiap2l2*$^{tm1b/tm1b}$ mice.

Considering that substantial hearing loss observed in young-adult *Baiap2l2*$^{tm1b/tm1b}$ mice (**Figs. 2-2, 2-3**), we investigated whether the absence of BAIAP2L2 caused any additional defects in the basolateral membrane properties of both IHCs and OHCs, which could have directly contributed to the hearing phenotype. Mature IHCs express a large outward K$^+$ current (I_{K}), which was present in both *Baiap2l2*$^{tm1b/+}$ and *Baiap2l2*$^{tm1b/tm1b}$ mice using whole-cell patch clamp recordings (**Fig. 2-9*A*-*C***). A characteristic K$^+$ current of mature IHCs is the rapid activating, large conductance Ca^{2+}-activated K$^+$ current named $I_{\mathrm{K,f}}$ (Kros *et al.*, 1998; Marcotti *et al.*, 2004), which was evident in IHCs from both genotypes using both electrophysiology (**Fig. 2-9*A*-*C*:** insets) and immunostaining (**Fig. 2-9*D***). The size of the total outward I_{K} and $I_{\mathrm{K,f}}$ were not significantly different between the two genotypes (I_{K}: P = 0.3001; $I_{\mathrm{K,f}}$: P = 0.1312, t-test, **Fig. 2-9*E***). Another K$^+$ current characteristic of mature IHCs is that carried by KCNQ4 channels ($I_{\mathrm{K,n}}$ (Marcotti *et al.*, 2003; Oliver *et al.*, 2003)), which was also similarly expressed in both genotypes (P = 0.8122, t-test, **Fig. 2-9*F,G***). Different from IHCs, the basolateral membrane K$^+$ current in adult OHCs is almost exclusively represented by $I_{\mathrm{K,n}}$ (**Fig. 2-10*A,B***, see also (Marcotti and Kros, 1999)). As for IHCs, the size of $I_{\mathrm{K,n}}$ was not significantly affected between control and littermate

Baiap2l2$^{tm1b/tm1b}$ mice in both young adult (P12: *P* = 0.4592, *t*-test, **Fig. 2-10***C*) and older mice (P29-40: *P* = 0.1022, **Fig. 2-10***D-F*). OHCs from adult *Baiap2l2*$^{tm1b/tm1b}$ mice also showed normal size and expression profile of the motor protein prestin (**Fig. 2-10***G*), which is required for driving non-linear (voltage dependent) capacitance, and is the signature of mature electromotility in OHCs (Abe *et al.*, 2007; Jeng *et al.*, 2020). We also found that the resting membrane potentials (V_m) and cell surface area (membrane capacitance, C_m) was not significantly different in both IHCs and OHCs from control and *Baiap2l2*$^{tm1b/tm1b}$ mice (see **Figs. 2-9, 2-10** legends).

These findings indicate that IHCs and OHCs from *Baiap2l2*$^{tm1b/tm1b}$ mice are normal and functional in terms of basolateral properties.

Interaction of BAIAP2L2 with other stereociliary bundle proteins.

We hypothesized that BAIAP2L2 may interact with other proteins known to be concentrated at the tip of the 2nd row of stereocilia, such as EPS8L2 (Furness *et al.*, 2013) and ESPNL (Ebrahim *et al.*, 2016a). We also reasoned that BAIAP2L2 could interact with proteins or protein families known to interact with other members of the I-BAR family, including the entire EPS8 family (Sekerkova *et al.*, 2003; Sudhaharan *et al.*, 2016), and the RHO GTPase family (Kast *et al.*, 2014; Sudhaharan *et al.*, 2016). We therefore tested the ability of BAIAP2L2 domains (**Fig. 2-11***A,B*) to interact *in vitro* with a panel of plausible interacting proteins (EPS8, EPS8L1, EPS8L2, ESPNL, CDC42, and RAC1); we also included the membrane-binding stereocilia proteins EZR and RDX were included as negative controls. The N-terminal I-BAR domain alone served as an additional negative control that was internal to the assay, as this domain is thought to primarily interact with membranes (Pykalainen *et al.*, 2011). Recombinant constructs of panel proteins were generated with either an N-terminal 6xHis tag or an N-terminal Myc tag, while BAIAP2L2 constructs were generated with an N-terminal GST tag. BAIAP2L2 domain constructs were tested for pulldown of the panel proteins using the method described (Sekerkova *et al.,* 2003) with some modifications (see Methods). We found that BAIAP2L2 interacted with CDC42, RAC1, EPS8, and ESPNL, but not with EPS8L1, EPS8L2, EZR or RDX (**Fig. 2-11***C*). To map where within BAIAPL2L2 these proteins bind, C-terminal truncations were assayed (**Fig. 2-11***A,B*); the BAIAP2L2 SH3 domain was necessary but not sufficient for the above mentioned interactions to occur (**Fig. 2-11***D*).

Dependence of BAIAP2L2 location on stereocilia proteins.

We investigated the biological significance of EPS8 and ESPNL interactions with BAIAP2L2 by probing their localization in *Baiap2l2*$^{tm1b/tm1b}$ and *Baiap2l2* $^{\Delta16/\Delta16}$ mice, and the localization of BAIAP2L2 in *Eps8* and *Espnl* knockouts (**Fig. 2-12***A-H*). The localization of both EPS8 (**Fig. 2-12***A,B*) and ESPNL (**Fig. 2-12***C,D*) is normal in *Baiap2l2*$^{tm1b/tm1b}$ and *Baiap2l2*$^{\Delta16/\Delta16}$ mice, respectively; BAIAP2L2 localization in *Espnl* knockout mice is also normal (**Fig. 2-12***E,F*). By contrast, BAIAP2L2 no longer targets to stereocilia tips in *Eps8* knockout mice (**Fig. 2-12***G,H*), which suggests that BAIAP2L2 targeting relies on an interaction with EPS8.

As EPS8 targeting to the tips of stereocilia requires the motor protein MYO15A (Manor *et al.*, 2011; Zampini *et al.*, 2011), we tested if BAIAP2L2 localization also required MYO15A. In mice deficient in MYO15A (*Myo15a*^{sh2} (Probst *et al.*, 1998)), we accordingly found that BAIAP2L2 labelling was absent at stereocilia tips (**Fig. 2-12***I,J*). This result indicates that the transport of BAIAP2L2 is similar to that of EPS8, but different than EPS8L2, which is still present in stereocilia of *Myo15a*^{sh2} mice (Furness *et al.*, 2013).

Discussion

The morphogenesis and maintenance of the stereociliary bundle in hair cells is a tightly regulated process requiring the interaction of several protein complexes, many of which include actin-capping and -bundling proteins as well as specialised myosin motors (Barr-Gillespie, 2015). We found that the I-BAR protein BAIAP2L2 (Ahmed *et al.*, 2010) is a new hair bundle protein located at the tips of the two shorter rows of transducing stereocilia of cochlear IHCs and OHCs. In the absence of BAIAP2L2, the hair bundle of OHCs progressively start to lose their 3rd row of stereocilia just before the onset of hearing. IHC stereociliary bundles appeared unaffected at least until P49. By 8 months of age, both OHCs and IHCs have lost the 3rd row of stereocilia and the 2nd row was largely affected. This morphological degeneration causes OHCs to lose about half of the MET current, which is likely to be attributed to the loss of MET channels situated at the tips of 3rd row stereocilia. The progressive deterioration of the stereociliary bundles in the absence of BAIAP2L2 leads to the rapid increase of hearing thresholds of *Baiap2l2*$^{tm1b/tm1b}$ mice, which become completely deaf before they reach 8 months of age (about 245 days). We also found that BAIAP2L2 interacts with other stereociliary proteins involved in the normal morphogenesis of the hair bundles (CDC42, RAC1, EPS8 and ESPNL), and that BAIAP2L2 localization to stereocilia tips depends on the motor protein MYO15A and its cargo EPS8 (Manor *et al.*, 2011; Tadenev *et al.*, 2019). We propose that BAIAP2L2 contributes to maintenance of the transducing stereocilia in mature cochlear hair cells by interacting with MYO15A and EPS8.

Baiap2l2 deficiency is associated with progressive hearing loss and the loss of the transducing stereocilia

Baiap2l2-deficient mice show progressive hearing loss, which leads to a highly reduced hearing sensitivity over the entire frequency range investigated (6-36 kHz). At P14, about two days after the onset of hearing in mice (Mikaelian and Ruben, 1964; Ehret, 1983; Romand, 1983), ABR thresholds were already significantly elevated in animals lacking BAIAP2L2, indicating that defects in hair cells are likely to begin during cochlear development. The initial morphogenesis of the stereocilia in *Baiap2l2*$^{tm1b/tm1b}$ mice appeared normal since OHCs and IHCs acquired hair bundles with a normal staircase structure. However, by the end of the second postnatal week, OHCs of *Baiap2l2*$^{tm1b/tm1b}$ mice start to lose the shortest (3rd) row of stereocilia. At this age, MET current and FM1-43 uptake into the hair cells through the MET channels were also significantly reduced in the OHCs of these mice. By 8 months of age, both OHCs and IHCs from *Baiap2l2*$^{tm1b/tm1b}$ mice have lost most of the shorter transducing stereocilia (2nd and 3rd rows). Altogether, these results indicate that BAIAP2L2 is essential for the maintenance of transducing stereocilia following morphogenesis.

Several proteins are known to regulate the length of the hair bundles during early stages of stereocilia growth through actin capping activity (Barr-Gillespie, 2015). Some of these proteins appear to be particularly enriched in the shorter transducing stereocilia, including TWF2 (Peng *et al.*, 2009), CAPZB (Avenarius *et al.*, 2017) and EPS8L2 (Furness *et al.*, 2013). EPS8L2 is a member of a family of actin-regulatory proteins (EPS8 and EPS8L1-L3) endowed with actin bundling and capping activities (Offenhauser *et al.*, 2004). In the hair cells, EPS8L2 acts by restricting the length of the shorter stereociliary rows by means of capping the barbed ends of actin filaments (Furness *et al.*, 2013). In *Eps8l2* knockout mice, both IHCs and OHCs start to lose the 3rd stereocilia row from ~1 month of age and by 8 months they almost completely disappear (Furness *et al.*, 2013). The loss of 3rd row stereocilia has also been observed for mice lacking ESPNL, an actin-regulating cargo of MYO3A/B (Ebrahim *et al.*, 2016a). In *Espnl* knockout mice, OHCs from the basal regions of cochleae begin to lose their 3rd row of stereocilia starting from ~P10, while OHCs from the more apical regions of the cochlea retained normal morphology (Ebrahim *et al.*, 2016a). Despite the common loss of 3rd row stereocilia for *Baiap2l2*, *Eps8l2*, and *Epsnl* knockout OHCs, the effect on hearing may not be uniform. *Espnl* and *Eps8l2* deficiency produce primarily high frequency hearing loss, while *Baiap2l2* deficiency appears to result in hearing loss over the entire mouse auditory frequency range. Despite the presence of BAIAP2L2 in IHCs from early stages of postnatal development, their hair bundle appeared unaffected at least up to P49. The lack of a significant IHC phenotype in *Baiap2l2* deficient mice until later in life could be due to the presence of functional redundancy among I-BAR proteins (see below).

Functional maturation of the stereociliary bundle of cochlear hair cells

Our data indicate that hearing loss in *Baiap2l2* deficient mice is caused by the gradual loss of the shortest rows of transducing stereocilia, which apparently leads to a reduction in the number of functional MET channels. Although OHCs exhibited hair bundle defects already at pre-hearing stages of development, by 8 months of age both hair cell types showed substantial loss of row 2 and row 3 stereocilia. Several protein complexes are needed to achieve the extremely precise regulation of the stereocilia actin cytoskeleton required to establish the fine structure of the hair bundle. This includes the regulation of the stereocilia length, which is identical within rows and between neighbouring hair cells, but also changes along the cochlea and between rows within each bundle (Tilney *et al.*, 1992; Kaltenbach *et al.*, 1994); Reviewed by: (Barr-Gillespie, 2015; Velez-Ortega and Frolenkov, 2019). The widening of the stereocilia in both IHCs and OHCs depends on the ability of the actin-bundling protein such as ESPN to bind to and cross-link the actin filaments (Bartles *et al.*, 1998; Sekerkova *et al.*, 2011). In adult cochlear hair cells, the tallest row of stereocilia contains a protein complex formed by EPS8, MYO15A-S, WHRN, GPSM2, and GNAI3[3], which acts to identify, selectively lengthen, and widen row

---

[3] See Fig. 1-3A for a model of how this complex is targeted.

1 relative to the other shorter rows (Belyantseva *et al.*, 2003; Mburu *et al.*, 2003; Manor *et al.*, 2011; Zampini *et al.*, 2011; Tarchini *et al.*, 2016; Tadenev *et al.*, 2019). Although the shaping of the shortest two rows of stereocilia is less well characterized, recent data indicate that EPS8L2 (Furness *et al.*, 2013), MYO15A-L (Fang *et al.*, 2015; Krey *et al.*, 2020), CAPZB (Avenarius *et al.*, 2017), TWF2 (Peng *et al.*, 2009) and gelsolin (Mburu *et al.*, 2010; Olt *et al.*, 2014) are all recruited to the tips of these stereocilia, where they may form a complex or complexes. The actin-capping activity of EPS8L2, CAPZB and TWF2 inhibits actin polymerization, thus shifting the equilibrium in favour of depolymerisation and resulting in their rows being shorter than row 1. The current data does not demonstrate that BAIAP2L2 interacts *in vivo* with any of the proteins thus far identified as regulators of row 2 and 3 stereocilia. However, as mentioned in the preceding section, the progressive loss of row 3 stereocilia is shared by *Baiap2l2*, *Eps8l2*, and *Espnl*-deficient OHCs, suggesting that the complementary or cooperative activity of these proteins may be required for maintenance of mature stereocilia. Whether these proteins do interact in stereocilia remains to be determined. However, the finding that BAIAP2L2 binds EPSNL *in vitro*, together with the observation that localization that both BAIAP2L2 and ESPNL concentrate at the tips of row 2 stereocilia (Ebrahim *et al.*, 2016a), suggests that a stereociliary BAIAP2L2-EPSNL interaction might be possible, although EPSNL and BAIAP2L2 do localize to stereocilia tips independently.

I-BAR proteins are known to exhibit functional redundancy (Saarikangas *et al.*, 2015; Chou *et al.*, 2017). Therefore, the presence of compensatory I-BAR protein members could explain why stereocilia morphogenesis in hair cells is normal despite BAIAP2L2 being expressed from early stages of postnatal development, and also why stereocilia are initially normal in IHCs that also localize

BAIAP2L2 at their stereocilia tip. Notably, the I-BAR proteins BAIAP2 and BAIAP2L1 are both detected in hair cells (umgear.org).

BAIAP2L2 and protein trafficking within stereocilia

The exact mechanism of how the complex of MYO15A-S and EPS8 facilitates the localization of BAIAP2L2 to the shorter two rows of stereocilia, and not the tallest row where the majority of EPS8 signal resides, remains unknown. We hypothesize that BAIAP2L2 is trafficked to all stereocilia tips as a cargo of MYO15A-EPS8-BAIAP2L2, but is selectively retained at the rows of the shorter tips by an unknown mechanism. The transduction channels are located selectively at stereocilia rows 2 and 3 (Beurg *et al.*, 2009), so retention of BAIAP2L2 may require the transduction channels themselves or a signal dependent on transduction. Why the MYO15A-EPS8 complex accumulates at the tips of row 1 without the presence of BAIAP2L2 is unknown.

I-BAR proteins regulate actin protrusions

The I-BAR proteins, by first dimerising and then binding to the membrane, are capable of detecting and inducing negative membrane curvature, such as what is present at the tip of a membrane protrusion (Zhao *et al.*, 2011). Thus, by localising to growing actin protrusions and recruiting proteins which facilitate actin filament elongation, members of this family are able to modulate protrusion growth (Sudhaharan *et al.*, 2016). For example, BAIAP2L1 is responsible for localising EPS8 to the growing microvilli of the brush border in the gut, and regulating their growth directly via its WH2 domain (Postema *et al.*, 2018). BAIAP2L1 localises itself via the I-BAR domain, likely by detecting negative membrane curvature, and loss of the SH3 domain results in shortened microvilli and a complete lack of EPS8 localisation (Postema *et al.*, 2018).

BAIAP2L2 represents an exception among the I-BAR proteins, since it appears to show particularly high expression in epithelial cells (Carman and Dominguez, 2018) and has a relatively flat membrane-binding surface, so instead of promoting membrane protrusion or invagination it assembles into planar membrane sheets (Pykalainen *et al.*, 2011). The diameters of cochlear stereocilia are relatively large compared to microvilli or filopodia, however, so an I-BAR protein favouring a flat membrane may readily associate at stereocilia tips. In contrast to BAIAP2L1 at the brush border of the gut, in the OHC stereocilia of the cochlea it appears as though the MYO15A-S-EPS8 complex precedes BAIAP2L2 at the tips of the shorter rows of stereocilia, and localises the I-BAR protein via an SH3 domain-dependent interaction. Alternatively, expression of *Baiap2l2* may lag behind the localization of *Myo15a* and *Eps8* (Scheffer *et al.*, 2015), so when *Baiap2l2* finally appears, it is transported to stereocilia tips via the MYO15A-S-EPS8 complex. Since the protein does not function to detect negative membrane curvature in this setting (Pykalainen *et al.*, 2011), it is likely to modulate actin dynamics directly after recruitment via the WH2 domain or indirectly through the recruitment or stabilisation of additional currently unknown actin effector proteins (Zhao *et al.*, 2011; Postema *et al.*, 2018). **Competing interests:** The Authors declare no conflict of interest.

Author contributions

All authors helped with the collection, analysing and interpretation of the data and commenting on the manuscript. A.J.C, J.H, P.G.B-G. and W.M. wrote the paper. S.D.M.B, M.R.B and W.M. conceived the study in the UK; P.G.B-G. conceived the study in the USA. P.G.B-G. and W.M. coordinated the study.

All authors approved the final version of the manuscript. All authors agree to be accountable for all aspects of the work in ensuring that questions related to the accuracy or integrity of any part of the work are appropriately investigated and resolved. All persons designated as authors qualify for authorship, and all those who qualify for authorship are listed

Funding: This work was supported by the: BBSRC (BB/S006257/1) to S.D.M.B, M.R.B and W.M. and National Institutes of Health grant R01DC002368 to P.G.B-G.

A.J.C. is funded by a PhD studentship from Action on Hearing Loss (S50).

Acknowledgements

In the UK, the authors thank Michelle Bird (University of Sheffield) for her assistance with the mouse husbandry, and Catherine Gennery and Laila Moushtaq-Kheradmandi for their genotyping work. The *Baiap2l2*<tm1a> allele (EM:07678) was imported from the EMMA repository at Orleans, France.

In the USA, we developed the *Baiap2l2*$^{\Delta 16}$ mouse line in conjunction with the OHSU Transgenic Mouse Models core, and carried out confocal microscopy in the OHSU Advanced Light Microscopy Core @ The Jungers Center (P30 NS061800 provided support for imaging).

The data that support the findings of this study are available from the corresponding authors upon reasonable request.

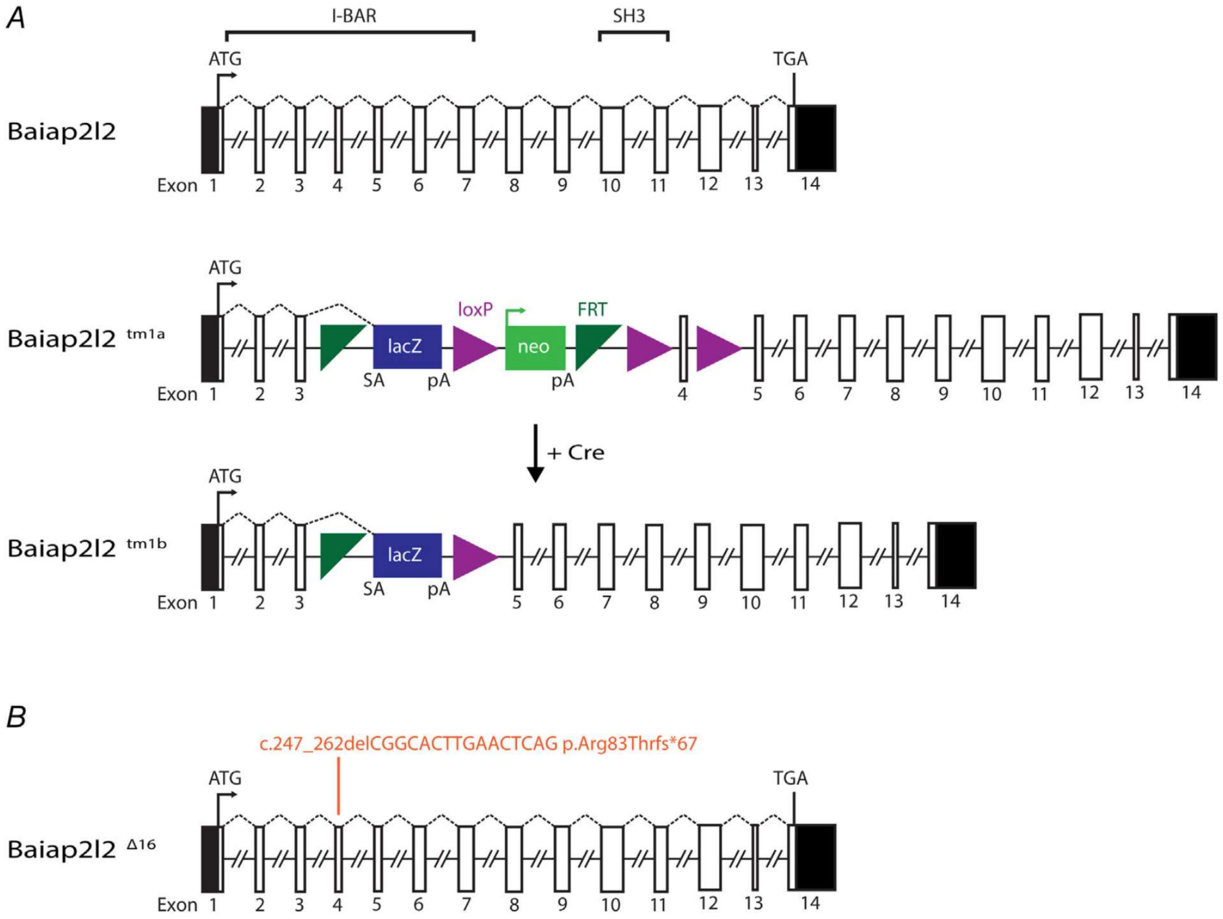

Figure 2-1. Schematic representation of the genomic structure of the mouse *Baiap2l2*.

A, *BAI1-associated protein 2-like 2* (*Baiap2l2*) gene (ENSMUSG00000018126; MGI:2652819) comprises 14 exons, spanning ~30 Kb of genomic DNA on chromosome 15. BAIAP2L2 is a 522 amino acid phosphoinositide-binding protein that contains an I-BAR domain (encoded by exons 1 to 7) and a SH3 domain (encoded by exons 10 and 11). The ATG (translation start) and the TGA (Stop) sites are in exons 1 and 14, respectively, and the untranslated regions are shown in black. The IMPC uses different targeting strategies to produce knockout alleles, which rely on the identification of a critical exon common to all transcript variants that when deleted disrupts gene function (Skarnes PMID: 21677750). For the *Baiap2l2* gene, a promoter-driven targeting cassette was used to generate a 'knockout-first' allele (tm1a) in C57BL/6N embryonic stem cells. Insertion of the *lacZ* trapping cassette and a floxed promoter-driven *neo* cassette inserted into intron 3 of the gene is expected to disrupt gene function. Cre-mediated deletion of the selection cassette and floxed exon 4 of the tm1a allele generates a *lacZ*-tagged allele (*tm1b*), which was used for the present study. *FRT*, flippase recognition target; neo, neomycin resistance gene; pA, polyadenylation site; SA, splice acceptor. *B,* Generation of the null allele of *Baiap2l2* using CRISPR/Cas9. gRNA was targeted to exon 4, and several mouse lines containing indels were obtained. We chose a line that had a 16 bp deletion (coding sequence deletion: c.247_262delCGGCACTTGAACTCAG; protein truncation: p.Arg83Thrfs*67). The protein product is predicted to be truncated in the I-BAR domain. We referred the line we used here as *Baiap2l2*$^{\Delta 16}$. Mice were backcrossed to C57BL/6 for more than six generations to minimize any off-target modifications.

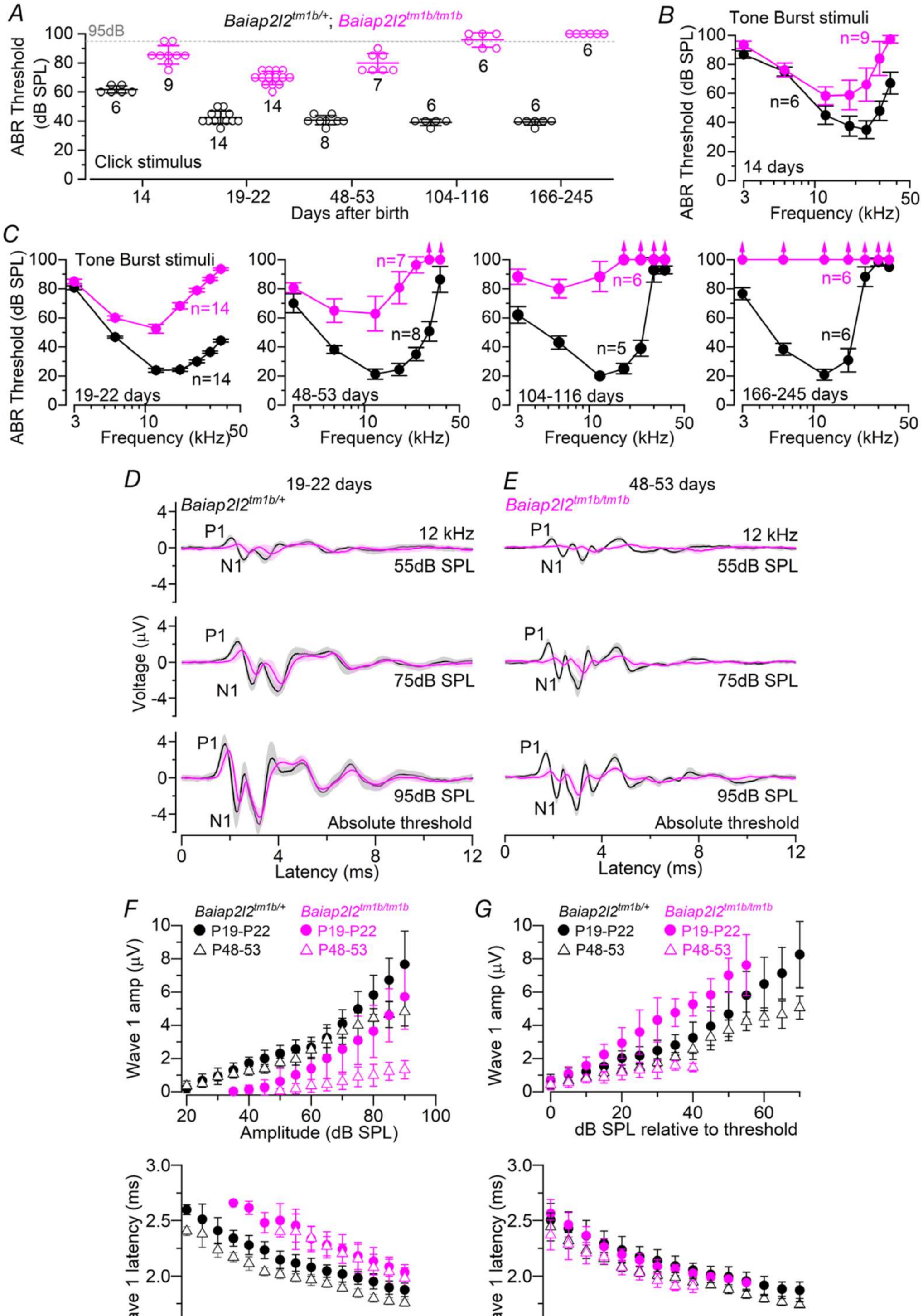

Figure 2-2. ABR thresholds evoked in *Baiap2l2* mice

A, Average ABR thresholds for click stimuli recorded from *Baiap2l2* control (*Baiap2l2*$^{+/tm1b}$) and knockout littermate mice (*Baiap2l2*$^{tm1b/tm1b}$) of increasing ages. The dashed line represents the upper threshold limit of our system, 95dB. Number of mice tested is shown above or below the average data points (closed symbols) and single data points is plotted as small open symbols. *B,C,* ABR thresholds for frequency-specific pure tone stimulation from 3 kHz to 36 kHz recorded from control and *Baiap2l2*$^{tm1b/tm1b}$ littermate mice at 14 days (*B*) and 19-22 days, 48-53 days, 104-116 days and 166-245 days (*C*) after birth. The number of mice tested for each age/strain is shown. *D,E,* Average ABR waveform responses at 12 kHz at increasing stimulus intensity (dB) relative to threshold at postnatal day 19-22 (*D*, control: $n = 14$; *Baiap2l2*$^{tm1b/tm1b}$: $n = 14$) and 48-53 (*E*, control: $n = 8$; *Baiap2l2*$^{tm1b/tm1b}$: $n = 7$). Continuous lines represent the average values and the shaded areas the SD. P1 and N1 indicate the positive and negative peaks of wave 1, respectively. *F,G,* Average amplitude (from P1 to N1: top panels) and latency of wave 1 (time between the onset of the stimulus and P1: bottom panels) as a function to the actual dB SPL used (*F*) and relative to threshold (*G*) in both strains at 19-22 days and 48-53 days. In panel F, the wave 1 amplitude of ABR signals below thresholds were set to zero, and were not used to measure the latency.

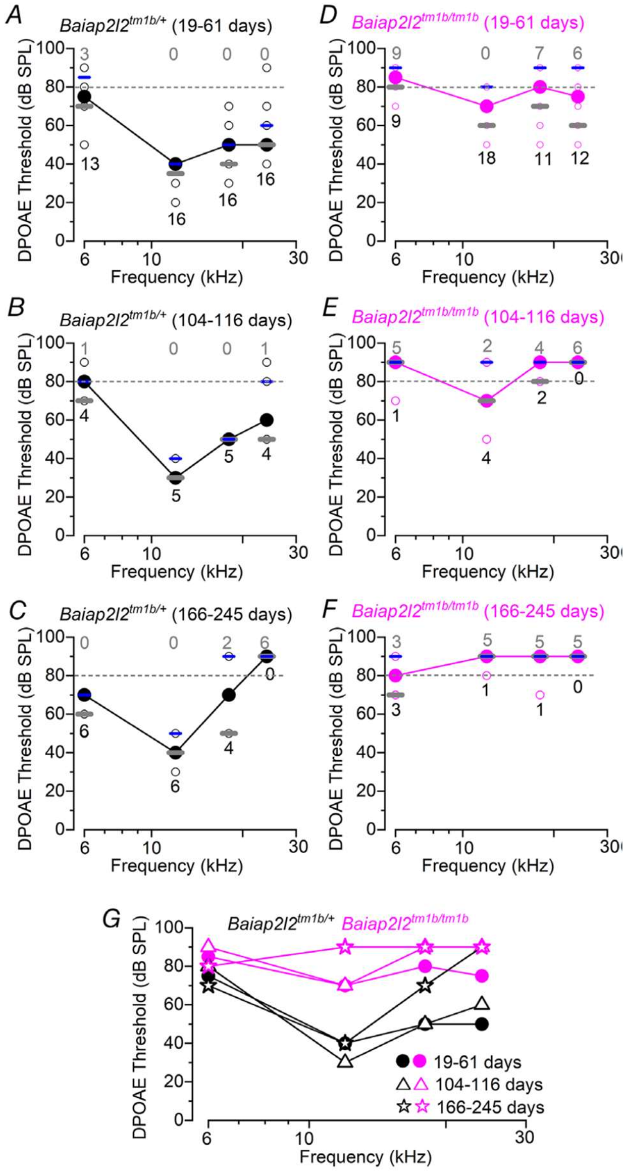

Figure 2-3. DPOAE thresholds are realised in *Baiap2l2* knockout mice

A-*F*, DPOAE thresholds measured from control (*A*-*C*) and *Baiap2l2*$^{tm1b/tm1b}$ mice (*D*-*F*) at 19-61 days (*A*,*D*), 104-116 days (*B*,*E*) and 166-145 days (*C*,*F*) after birth. The frequency range tested was: 6 kHz, 12 kHz, 18 kHz and 24 kHz. Due to the presence of "not-found" values (i.e. above the upper threshold limit of our system, 80dB), values are plotted as the median (black line and circles) together with the first (red lines) and third (blue lines) quartiles. Single values are reported as open circles. The number of "found" and "not-found" values at each frequency is shown below (grey) and above (blue) the median (closed circles and lines), respectively. *G,* Comparison of the median DPOAE thresholds from panels *A*-*F*.

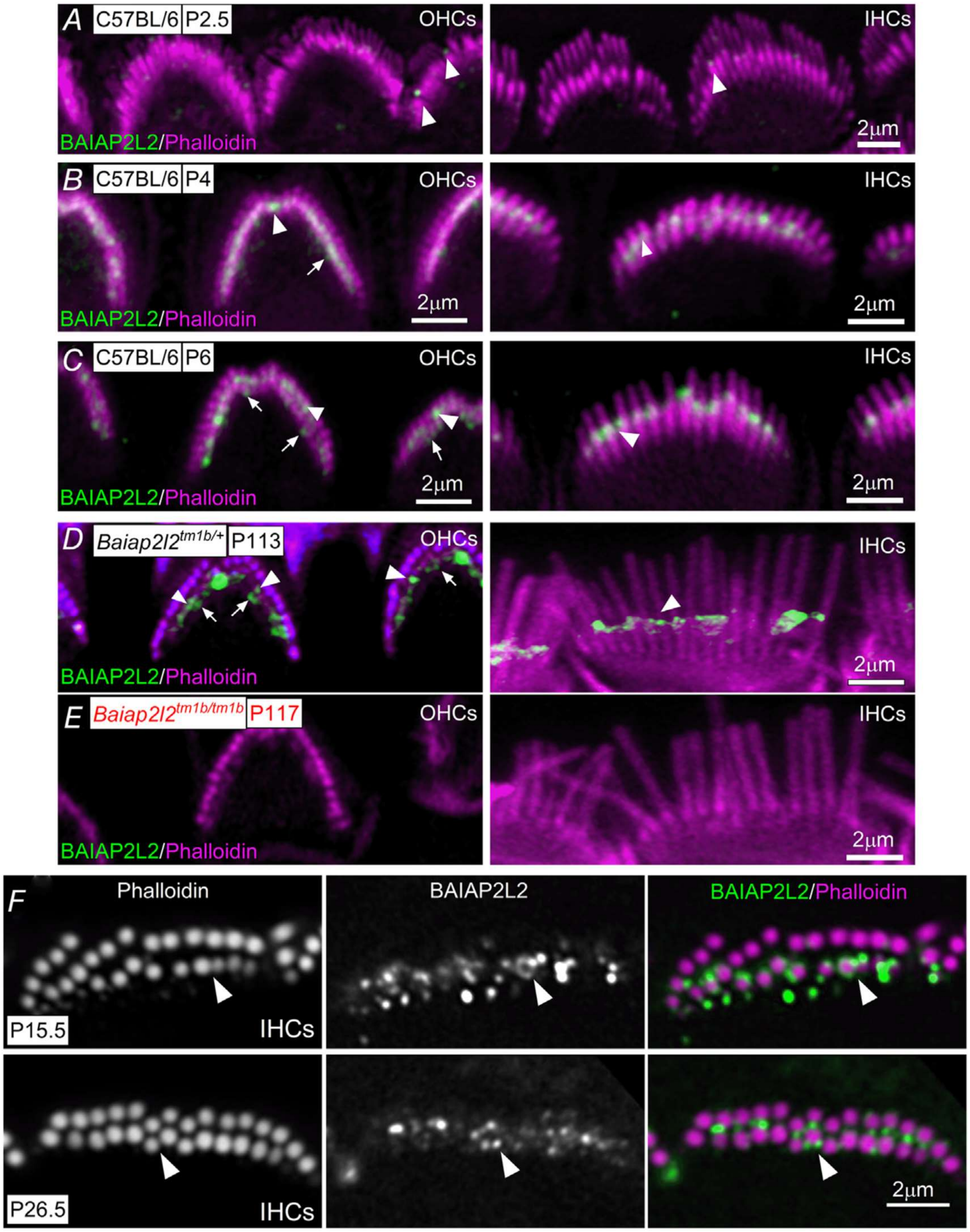

Figure 2-4. BAIAP2L2 localizes to stereocilia tips

A-*D*, Antibody against BAIAP2L2 (green) labels its localization at stereocilia tips in apical-coil OHCs (*A*-*D*, left panels) and IHCs (*A*-*D*, right panels) from P2.5 (*A*), P4 (*B*), P6 (*C*) and P113 (*D*) mice. Anti-BAIAP2L2 was: Atlas Antibodies (HPA003043). Phalloidin (red) labels actin, marking the stereocilia.

Note that BAIAP2L2 is localized at the tips of the second (arrowheads) and third (arrows) rows of stereocilia in OHCs, but primarily in the second rows of stereocilia in IHCs (arrowheads). *E*, BAIAP2L2 staining was absent in the stereocilia of OHCs (left) and IHCs (right) from P117 *Baiap2l2*$^{tm1b/tm1b}$ mice using the same antibody listed above. *F*, Top view of the stereocilia from P15.5 (top panels) and P26.5 (bottom panels) IHCs to show that BAIAP2L2 (green) localization shifts to stereocilia shafts in older animals. Single slices shown at approximately mid-way down the length of row, with instances of clear annular signal marked with arrowheads.

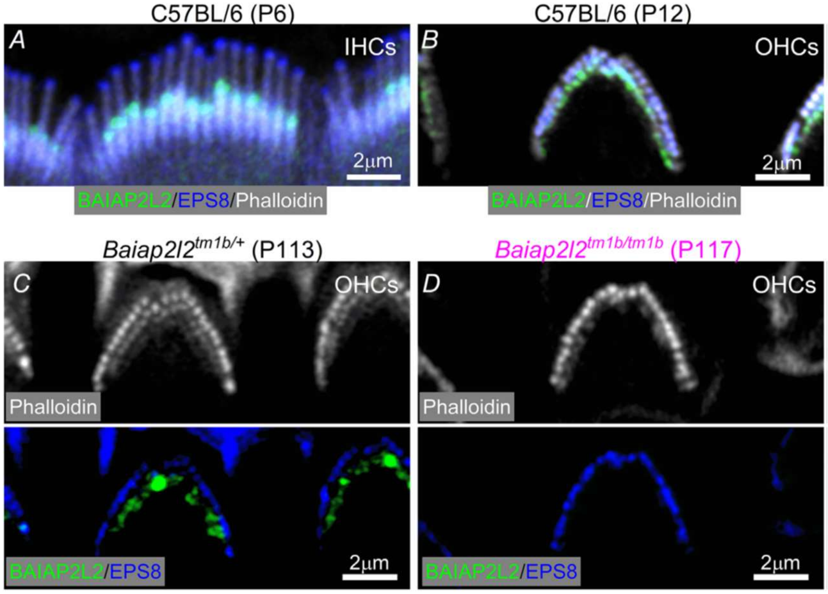

Figure 2-5. Separate localization of BAIAP2L2 and EPS8 at the stereocilia tips

A-*C*, BAIAP2L2 (green) and EPS8 (blue) appear spatially segregated, with the latter primarily located at the tips of the taller rows of stereocilia in P6 IHCs (*A*) and P12 OHCs (*B*) from C57BL/6 mice, and P113 OHCs (*C*) from *Baiap2l2*$^{+/tm1b}$. *D*, OHCs from *Baiap2l2*$^{tm1b/tm1b}$ mice only showed EPS8 staining. In *C* and *D*, the phalloidin staining (white: stereociliary marker) is shown in a separate panel to better visualize the segregated distribution of BAIAP2L2 and EPS8.

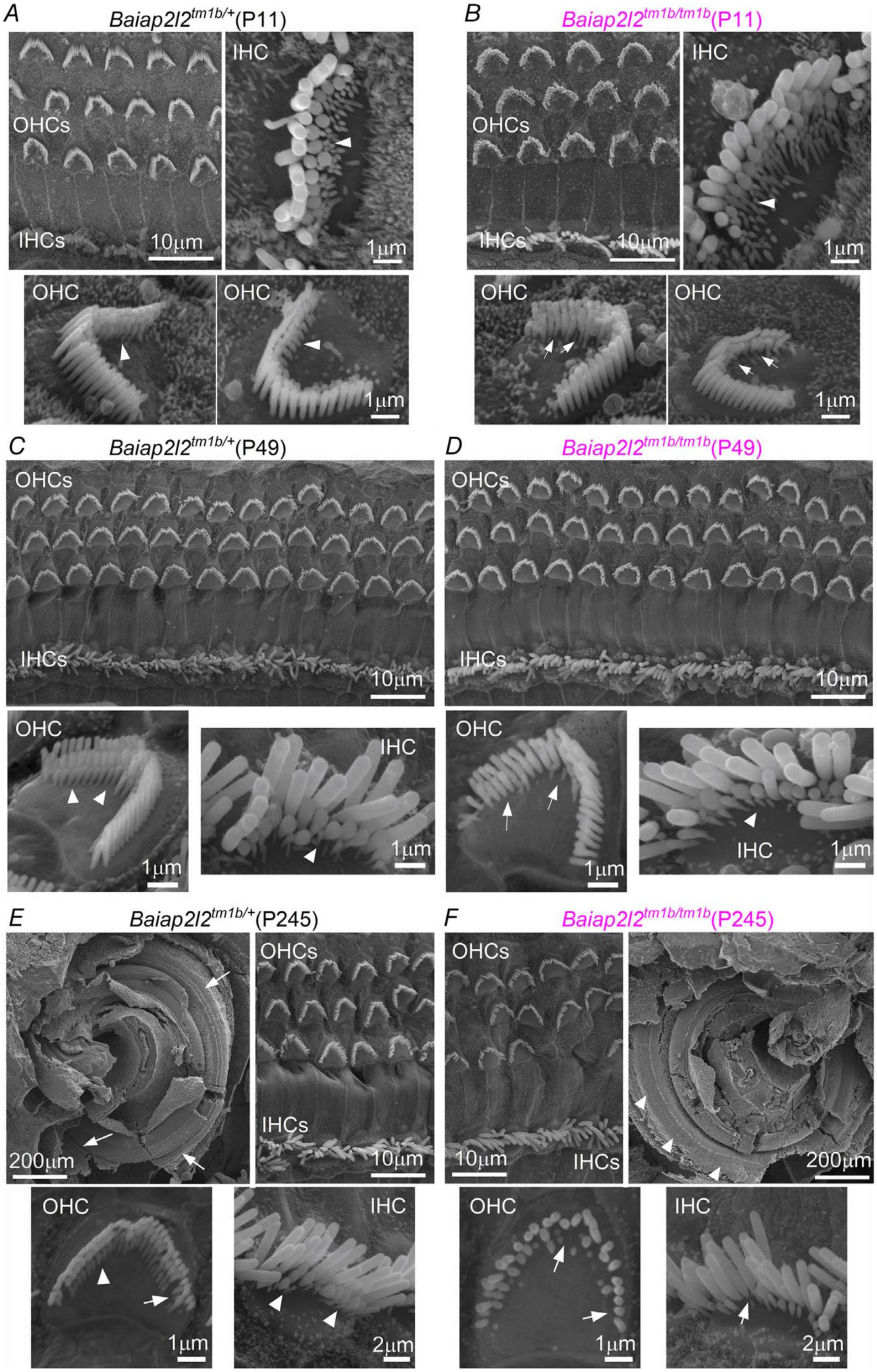

Figure 2-6. Hair bundle morphology in hair cells from adult *Baiap2l2* mice.

A-F, Scanning electron micrographs (SEM) showing the typical hair bundle structure from apical-coil OHCs and IHCs in control (**A**,**C**,**E**) and *Baiap2l2*$^{tm1b/tm1b}$ mice (**B**,**D**,**F**) at pre-hearing stages of development (P11: **A**,**B**), at P49 (**C**,**D**) and at P245 (**E**,**F**). Note that generally, hair bundles are composed of three rows of stereocilia: tall, intermediate and short. Arrowheads indicate the presence of the third row of stereocilia; arrows indicate missing stereocilia in *Baiap2l2* knockout OHCs. Panel **E** and **F** also show low magnification SEM illustrating the gross morphology of the apical coil portion of the cochlea control (**E**, top left) and *Baiap2l2*$^{tm1b/tm1b}$ (**F**, top right) mice at P245 days of age. Note that the hair bundles of the hair cells are gradually disappearing from the surface of the epithelium in *Baiap2l2*$^{tm1b/tm1b}$ (arrowheads in panel **F**) but still present in littermate controls (arrows in panel **E**).

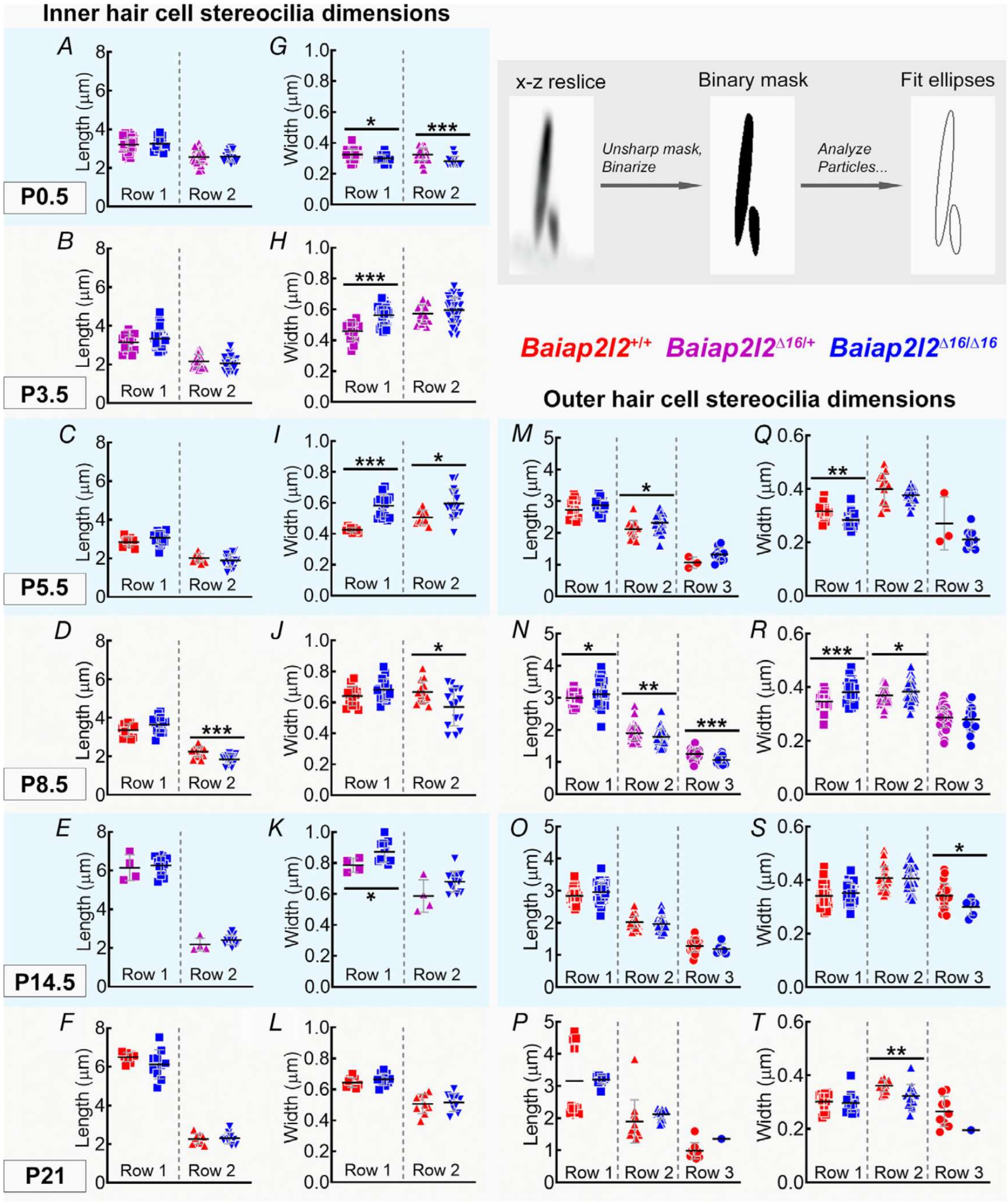

Figure 2-7. Bundle morphology is normal at early stages of development in both IHCs and OHCs

A-L, IHC stereocilia lengths and widths for rows 1 and 2. Row 3 stereocilia of IHCs are typically not resolvable by fluorescence, and thus not measured here. P0.5 from *Baiap2l2*$^{\Delta 16/+}$ (magenta: n = 42 stereocilia profiles from 15 IHCs, 4 cochleae), *Baiap2l2*$^{\Delta 16/\Delta 16}$ (blue: n =12 stereocilia profiles from 5

IHCs, 2 cochleae). P3.5 *Baiap2l2*$^{\Delta16/+}$ (*n* = 15 stereocilia, 5 IHCs, 3 cochleae), *Baiap2l2*$^{\Delta16/\Delta16}$ (*n* = 42 stereocilia, 15 IHCs, 6 cochleae). P5.5 *Baiap2l2*$^{+/+}$ (red, *n* = 9 stereocilia, 5 IHCs, 2 cochleae), *Baiap2l2*$^{\Delta16/\Delta16}$ (*n* = 16 stereocilia, 7 IHCs, 2 cochleae). P8.5 *Baiap2l2*$^{+/+}$ (*n* = 13 stereocilia, 5 IHCs, 1 cochleae), *Baiap2l2*$^{\Delta16/\Delta16}$ (*n* = 15 stereocilia, 6 IHCs, 2 cochleae). P14.5 *Baiap2l2*$^{\Delta16/+}$ (*n* = 4 stereocilia, 3 IHCs, 1 cochleae), *Baiap2l2*$^{\Delta16/\Delta16}$ (*n* = 12 stereocilia, 6 IHCs, 1 cochleae). P21 *Baiap2l2*$^{+/+}$ (*n* = 9 stereocilia, 3 IHCs, 1 cochleae), *Baiap2l2*$^{\Delta16/\Delta16}$ (*n* = 10 stereocilia, 7 IHCs, 3 cochleae). *M-T*, OHC stereocilia lengths and widths for rows 1, 2, and 3. The number of measurable row 3 stereocilia decreases by P21. P5.5 *Baiap2l2*$^{+/+}$ (*n* = 13 stereocilia, 6 OHCs, 2 cochleae), *Baiap2l2*$^{\Delta16/\Delta16}$ (*n* = 23 stereocilia, 5 OHCs, 1 cochleae). P8.5 *Baiap2l2*$^{\Delta16//+}$ (*n* = 73 stereocilia, 15 OHCs, 4 cochleae), *Baiap2l2*$^{\Delta16/\Delta16}$ (*n* = 45 stereocilia, 9 OHCs, 2 cochleae). P14.5 *Baiap2l2*$^{+/+}$ (*n* = 31 stereocilia, 7 OHCs, 3 cochleae), *Baiap2l2*$^{\Delta16/\Delta16}$ (*n* = 38 stereocilia, 9 OHCs, 3 cochleae). P21 *Baiap2l2*$^{+/+}$ (*n* = 12 stereocilia, 5 OHCs, 2 cochleae), *Baiap2l2*$^{\Delta16/\Delta16}$ (*n* = 15 stereocilia, 8 OHCs, 2 cochleae). All measurements made from apical turn of the cochlea. Pairwise comparisons between genotypes used t-tests (2-tailed, assumption of equal variance). Individual measurements of each stereocilia are plotted separately and overlaid with their mean ± SD. The inset shows an example stereocilia pair from P21 IHCs of *Baiap2l2*$^{+/+}$ mice, demonstrating extraction of length and width measurements from fit ellipses applied to processed x-z reslice (panel width of 4 μm).

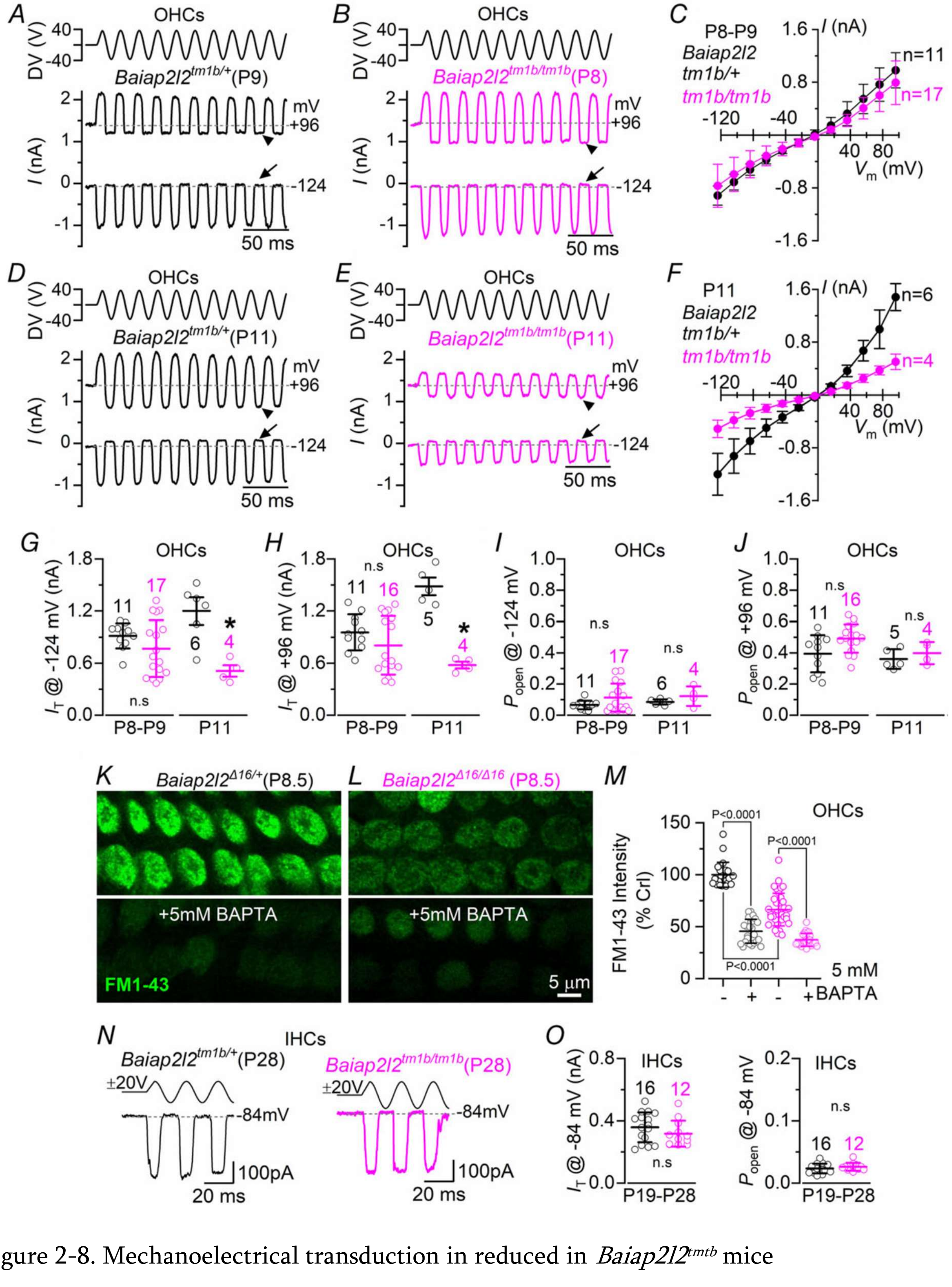

Figure 2-8. Mechanoelectrical transduction in reduced in *Baiap2l2*^{tmtb} mice

A,B, Saturating MET currents in apical OHCs from control (*A*, P9) and *Baiap2l2*$^{tm1b/tm1b}$ (B, P8) mice in response to 50 Hz sinusoidal force stimuli to the hair bundles at membrane potentials of –124 mV and +96 mV. Driver voltage (DV) stimuli to the fluid jet are shown above the traces, with positive deflections of the DV being excitatory. The arrows and arrowheads indicate the closure of the transducer channel in response to inhibitory bundle stimuli at –124 mV and +96 mV, respectively. *C*, Average peak to peak MET current-voltage curves from apical OHCs of control *Baiap2l2*$^{tm1b/+}$ (*n* = 11) and littermate *Baiap2l2*$^{tm1b/tm1b}$ (*n* = 17) mice. Recordings were obtained by mechanically stimulating the hair bundles of OHCs while stepping their membrane potential from –124 mV to +96 mV in 20 mV increments. *D-F*, Saturating MET current recorded in P11 OHCs from control (*n* = 6) and littermate *Baiap2l2*$^{tm1b/tm1b}$ (*n* = 4) mice using the same protocols described in panels *A-C*. *G,H*, Maximal size of the MET current in both genotypes measured at –124 mV (G) and +96 mV (*H*) at the two age range investigated in panels *A-F*. *I,J*, Resting open probability (P_o) of the MET current in OHCs from the two genotypes at and the two age tested from the holding of –124 mV (I) and +96 mV(*J*). The resting current is given by the holding current minus the current present during inhibitory bundle deflection. The P_o was found not significantly different between the two genotypes, even though the size of the MET current was largely reduced at P11 (–124 mV: $P = 0.1950$; +96 mV: $P = 0.4225$, *t*-test). At P8-P9 P_o was also not significantly different between the two genotypes (–124 mV: $P = 0.1035$; +96 mV: $P = 0.0680$). For average data values see Supplementary Statistical Summary Table. *K-M*, Example experiment for FM1-43 uptake by OHCs from P8.5 *Baiap2l2*$^{\Delta16/+}$ (*K*) and P8.5 *Baiap2l2*$^{\Delta16/\Delta16}$ mice with and without the application of 5 mM BAPTA, with quantification (*L*). Representative results shown from a single experiment (*n* = 24 - 36 OHCs per condition). Statistical test done with one-way ANOVA, Sidak's multiple comparison test. *N*, Saturating MET currents in apical IHCs from *Baiap2l2*$^{tm1b/+}$ (left, P28) and

Baiap2l2$^{tm1b/tm1b}$ (right, P28) mice in response to 50 Hz sinusoidal force stimuli to the hair bundles at membrane potentials of –84. Driver voltage (DV) stimuli to the fluid jet are shown above the traces. *O*, Maximal size of the MET current (left) and resting open probability (P_o: right) in adult IHCs from both genotypes measured at –84 mV.

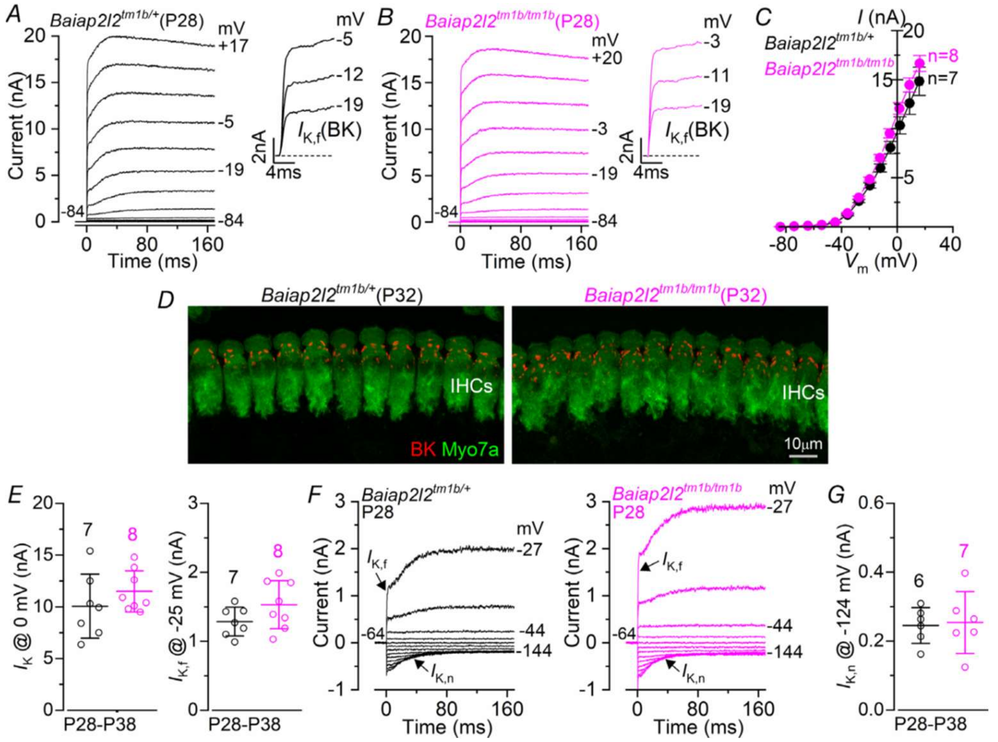

Figure 2-9. The basolateral membrane properties of adult IHCs are indistinguishable between control and littermate *Baiap2l2*$^{tm1b/tm1b}$ mice

A,B, Current responses from IHCs of control *Baiap2l2*$^{tm1b/+}$ (*A*) and *Baiap2l2*$^{tm1b/tm1b}$ (*B*) P28 mice. Current recordings were elicited by using depolarizing voltage steps (10 mV increments) from the holding potential of –84 mV to the various test potentials shown by some of the traces. The fast activation of the BK current ($I_{K,f}$) is better appreciated in the expanded time scale (see insets). ***C***, Steady-state current-voltage curves obtained from IHCs of control (P28-38) and *Baiap2l2*$^{tm1b/tm1b}$ (P28-35) mice. ***D***, Maximum intensity projections of confocal z-stacks taken from the apical cochlear region of control and *Baiap2l2*$^{tm1b/tm1b}$ P32 mice using antibodies against BK (red) and the hair cell marker Myo7a (green). ***E***, The size of the outward K$^+$ current $I_{K,f}$, which was measured at –25 mV and at 1 ms from the onset of the voltage step (Marcotti *et al.* 2003). Number of IHCs recorded are shown above each column. ***F***, Current responses from IHCs of control *Baiap2l2*$^{tm1b/+}$ and *Baiap2l2*$^{tm1b/tm1b}$ P28 mice, elicited by using hyperpolarizing and depolarizing voltage steps (10 mV increments) from the holding potential of –64 mV to the various test potentials shown by some of the traces. This protocol is used to emphasise the presence of $I_{K,n}$. *G*, The size of $I_{K,n}$, which was measured as the difference between the peak and steady state of the deactivating inward current at -124 mV. Single cell value recordings (open symbols) are plotted behind the average data. Number of IHCs investigated is shown above the average data points. The average IHC resting membrane potential (V_m) and membrane capacitance (C_m) were not significantly different between *Baiap2l2*$^{tm1b/+}$ (V_m –70.4 ± 2.0 mV, $n = 8$; C_m 11.4 ± 2.4 pF, $n = 8$) and *Baiap2l2*$^{tm1b/tm1b}$ mice (V_m –70.7 ± 3.5 mV, $n = 9$, $P = 0.8275$; C_m 12.2 ± 2.9 pF, $n = 8$, $P = 0.5606$, t-test).

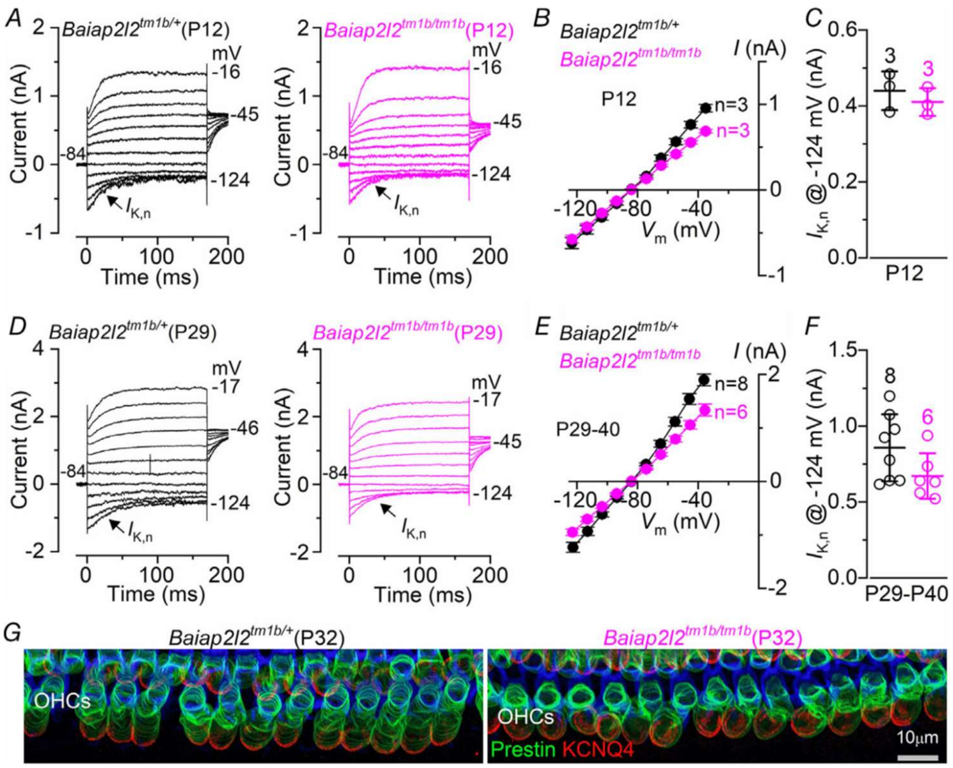

Figure 2-10. The basolateral membrane properties of adult OHCs are preserved in *Baiap2l2*^{tm1b} mice.

A-*F*, Current responses from OHCs of control (*Baiap2l2*$^{tm1b/+}$) and *Baiap2l2*$^{tm1b/tm1b}$ mice at the onset of hearing (P12: *A*-*C*) and adult mice (P29-40: *D*-*F*). Current recordings were elicited by using depolarizing and hyperpolarizing voltage steps (10 mV increments) from the holding potential of –84 mV to the various test potentials shown by some of the traces. Note that the a large $I_{K,n}$, which is carried by KCNQ4 channels, is present in OHCs at all ages and in both genotypes. Peak current-voltage curves obtained from OHCs of control and *Baiap2l2*$^{tm1b/tm1b}$ mice are shown in *B* (P12) and *E* (P29-40). The size of the isolated $I_{K,n}$ (see **Fig. 9*E***) was not significantly different between the two genotypes (*C*: P12: P = 0.4592; *F*: P29-40: P = 0.1022, *t*-test). Number of IHCs recorded are shown next to the current-voltage traces (*B*,*E*) or above each column (*C*,*F*). *G*, Maximum intensity projections of confocal z-stacks taken from the apical cochlear region of control and *Baiap2l2*$^{tm1b/tm1b}$ mice at P32 using antibodies against KCNQ4 (red) and prestin (green). Phalloidin (blue) highlights the cuticular plate of the OHCs. Myo7a was used as the hair cell marker (blue). Single cell value recordings (open symbols) are also plotted behind the average closed symbols. Number of OHCs investigated is shown above the average data points. The average OHC resting membrane potential (V_m) and membrane capacitance (C_m) were not significantly different between *Baiap2l2*$^{+/tm1b}$ (V_m –73.1 ± 1.6 mV, $n = 9$; C_m 10.6 ± 0.6 pF, $n = 8$) and *Baiap2l2*$^{tm1b/tm1b}$ mice (V_m –73.7 ± 1.3 mV, $n = 6$, $P = 0.7528$; C_m 10.1 ± 0.3 pF, $n = 6$, $P = 0.5449$, t-test).

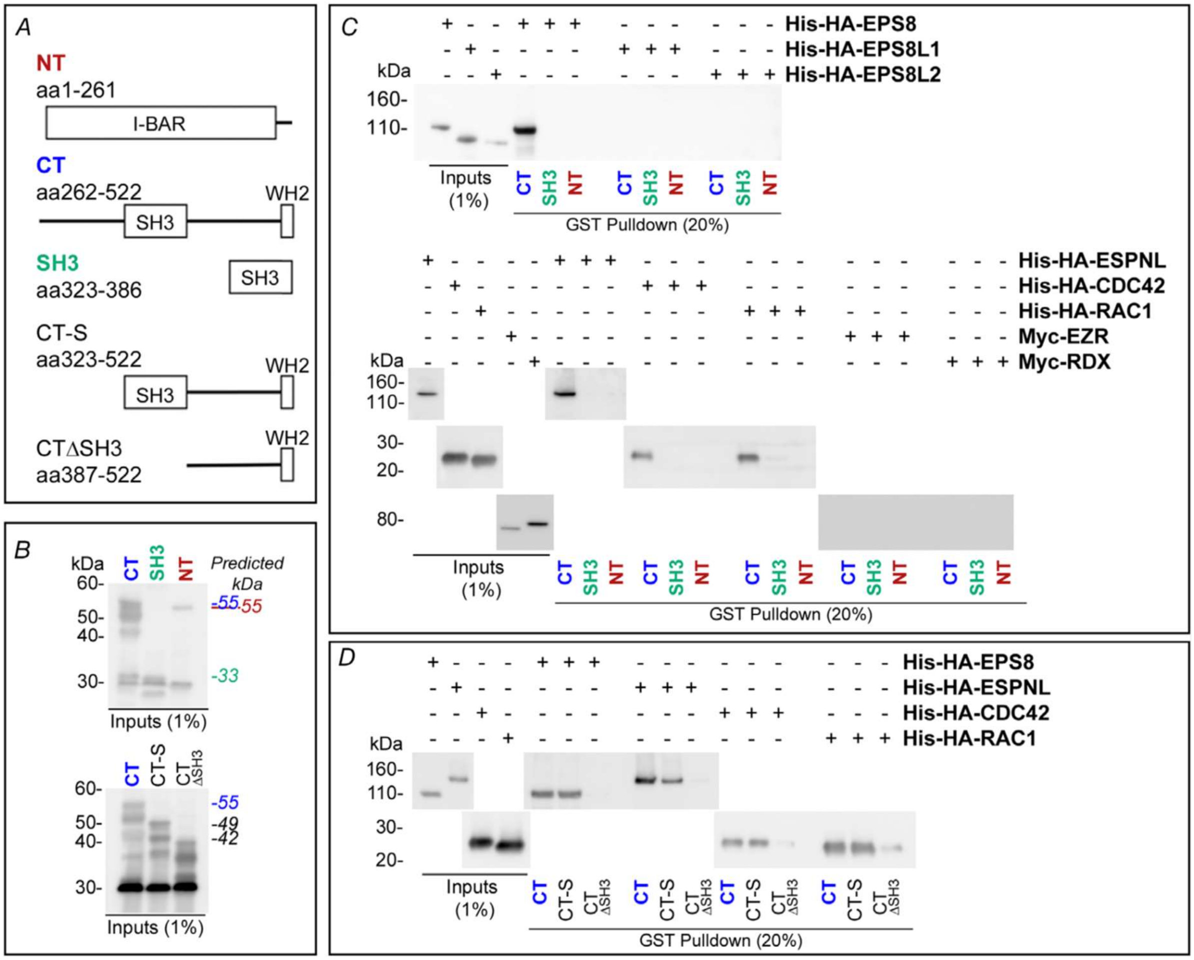

Figure 2-11. BAIAP2L2 interacts with actin-associated stereociliary proteins.

A, Cartoon diagrams showing the GST-tagged *Baiap2l2* constructs used for the *in vitro* pulldown assays (GST tag not included in diagrams). Residue numbering is from the canonical sequence for mouse *Baiap2l2*. *B*, Example immunoblot of GST inputs used for pulldown assays. Detected with rabbit anti-GST. Predicted MW for each of the constructs is indicated on the right, with text colour corresponding to the text colour for callout above the appropriate lane. *C*, Immunoblots with His or Myc inputs, and eluates containing BAIAP2L2 complexes from *in vitro* pulldown assays with *BAIAP2L2* fragments to identify interacting proteins. BAIAP2L2 C-terminal domain interacted with EPS8, EPSNL, CDC42, and RAC1. Immunoblots detected with mouse anti-His (EPS8, EPS8L1, EPSL2, ESPNL, CDC42, RAC1) or rabbit anti-Myc (EZR, RDX). Volume blotted for inputs was 1%, and 20% for pulldown eluates. *D*, Immunoblots with His inputs, and eluates containing BAIAP2L2 complexes from *in vitro* pulldown assays with truncates of the BAIAP2L2 C-terminal domain to map BAIAP2L2 binding site. The BAIAP2L2 SH3 domain was found to be necessary for the identified interactions. Detected with mouse anti-His. For *B-D*, Volume blotted for input lanes was 1% of the total volume used for the assay, while the volume blotted for pulldown lanes was 20% of the total eluate volume.

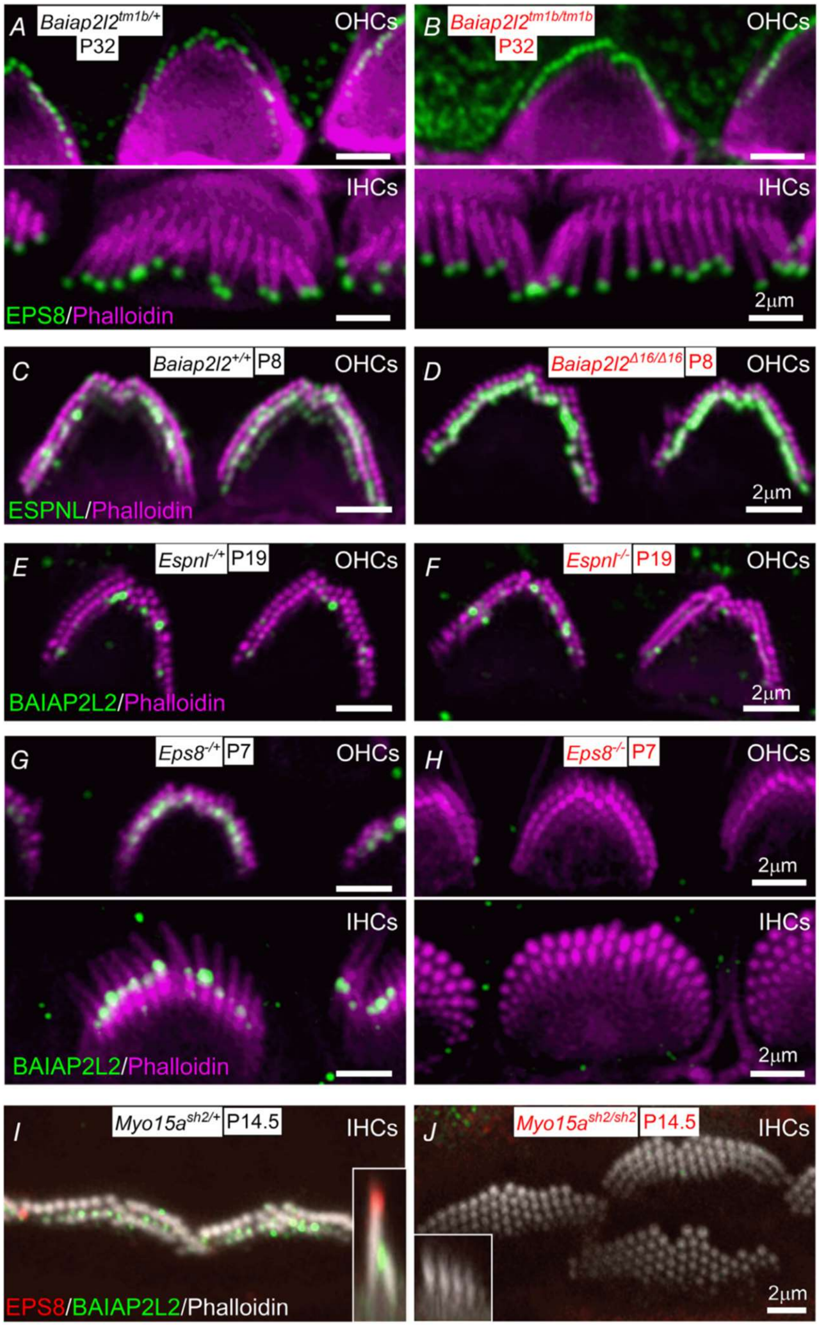

Figure 2-12. BAIAP2L2 targeting to stereocilia tips requires EPS8 and MYO15A.

A,B, EPS8 (green) localization in IHCs and OHCs is normal in *Baiap2l2*$^{tm1b/tm1b}$ mice at P32. ***C,D***, ESPNL is normally localized at the stereocilia of *Baiap2l2*$^{Δ16/Δ16}$ mice. ***E,F***, BAIAP2L2 is also present at the stereocilia tip of *Espnl*$^{-/-}$ mice. ***G,H***, BAIAP2L2 does not localize to stereocilia tips of OHCs (upper panels) and IHC (lower panels) in *Eps8*$^{-/-}$ mice at P7. ***I,J,*** BAIAP2L2 and EPS8 both fail to localize to stereocilia tips in *Myo15a*$^{sh2/sh2}$ mice. Insets of x-z reslices to compare stereocilia profiles and respective localization at row 1 and row 2 tips for EPS8 and BAIAP2L2.

Chapter 3 – Ca^{2+} entry through mechanotransduction channels localizes BAIAP2L2 to stereocilia tips

---

Julia Halford, Michael Bateschell, Peter G. Barr-Gillespie[†]

Oregon Hearing Research Center & Vollum Institute, Oregon Health & Science University, Portland, OR 97239, USA

[†] Manuscript correspondence at: Oregon Hearing Research Center, Mail code L335A, Oregon Health & Science University, 3181 SW Sam Jackson Park Road, Portland, OR 97239, USA; phone, 503-494-2936; email, gillespp@ohsu.edu

This work was published in Molecular Biology of the Cell, April 1, 2022; 33 (4).

Figure Attributions

Fig. 3-1. J.H. performed proximity ligation assays and immunostaining.

Fig. 3-2. J.H. performed interaction assays.

Fig. 3-3. J.H. performed immunostaining.

Fig. 3-4. J.H. prepared cochlear explants and performed immunostaining.

Fig. 3-5. M.B. generated plasmid used in (B). J.H. performed experiments and analysis in (A-I)

Supplemental Fig. 3-1. J.H. performed proximity ligation assays (A-C). M.B. generated the new *Eps8*-null line via i-GONAD (D). J.H. performed immunostaining (E-G).

Supplemental Fig. 3-2. J.H. performed interaction assays.

Supplemental Fig. 3-3. J.H. prepared cochlear explants and performed immunostaining.

Abstract

BAIAP2L2, a membrane-binding protein required for maintenance of mechanotransduction in hair cells, is selectively retained at tips of transducing stereocilia. BAIAP2L2 trafficked to stereocilia tips in the absence of EPS8, but EPS8 increased the efficiency of localization. A tripartite complex of BAIAP2L2, EPS8, and MYO15A formed efficiently *in vitro*, and these three proteins robustly targeted to filopodia tips when co-expressed in cultured cells. Mice lacking functional transduction channels no longer concentrated BAIAP2L2 at row 2 stereocilia tips, a result that was phenocopied by blocking channels with tubocurarine in cochlear explants. Transduction channels permit Ca^{2+} entry into stereocilia, and we found that membrane localization of BAIAP2L2 was enhanced in the presence of Ca^{2+}. Finally, reduction of intracellular Ca^{2+} in hair cells using BAPTA-AM led to a loss of BAIAP2L2 at stereocilia tips. Taken together, our results show that a MYO15A-EPS8 complex transports BAIAP2L2 to stereocilia tips, and Ca^{2+} entry through open channels at row 2 tips retains BAIAP2L2 there.

Abbreviations: BAIAP2L2, brain-specific angiogenesis inhibitor 1-associated protein 2-like protein 2; DIV, days *in vitro*; IHC, inner hair cell; PLA, proximity ligation assay; RFP, red fluorescent protein; ROI, region of interest; IQR, interquartile range.

Introduction

Vertebrate hearing relies on the transduction of the mechanical stimulus of sound into an electrical signal. Hair bundles, which project from the apical surface of sensory hair cells, mediate this process (Hudspeth, 1997). Bundles consist of ~100 stereocilia, membrane-enveloped protrusions of filamentous actin, organized into distinct rows that form a staircase pattern (Tilney *et al.*, 1980; Kaltenbach *et al.*, 1994). In mammalian auditory hair cells, the staircase includes the tall and thick row 1, the shorter and thick row 2, and the shortest and thinnest row 3. Transduction channels, located at tips of row 2 and 3 stereocilia (Beurg *et al.*, 2009), are partially open at rest but open even further as a stimulus deflects the bundle towards the tallest row. Tip links, which are extracellular protein filaments that extend from the tip of a transducing stereocilium to the shaft of its nearest tall neighbor, convey stimulus force to transduction channels (Fettiplace and Kim, 2014).

Transduction modulates the dimensions of stereocilia in the hair bundle. Mouse mutants lacking components of the transduction apparatus have altered stereocilia organization and dimensions (Cosgrove and Zallocchi, 2014). Further, blocking transduction channels or breaking tip links induces reversible changes in stereocilia length within 1-2 days (Velez-Ortega *et al.*, 2017; Krey *et al.*, 2020). Disruption of transduction also affects distribution of key bundle proteins (Krey *et al.*, 2020; McGrath *et al.*, 2021). Finally, Ca^{2+} entry through transduction channels regulates the function of many stereocilia proteins (Fettiplace, 2017).

We and others showed previously that brain-specific angiogenesis inhibitor 1-associated protein 2-like protein 2 (BAIAP2L2) stabilizes the shorter transducing stereocilia. BAIAP2L2 enriches at the tips of those stereocilia, interacts with the actin regulator EPS8, and depends on MYO15A for localization (Carlton *et al.*, 2021; Yan *et al.*, 2022). These results suggested that BAIAP2L2 may be transported by the transduction-regulated MYO15A-EPS8 complex (Manor *et al.*, 2011; Ebrahim *et al.*, 2016b; Lin *et al.*, 2021), which carries other hair-bundle proteins (Tadenev *et al.*, 2019; Krey *et al.*, 2020). MYO15A and EPS8 are both essential for normal bundle development; mutants in either gene produce bundles with short, narrow stereocilia (Belyantseva *et al.*, 2003; Zampini *et al.*, 2011). BAIAP2L2 also can bind EPS8L2 and CAPZB, which both concentrate at row 2 tips, unlike EPS8 and MYO15A (Yan *et al.*, 2022).

BAIAP2L2 is an inverse Bin/amphiphysin/Rvs (I-BAR) domain protein (Pykalainen *et al.*, 2011; Zhao *et al.*, 2011), a family that links the plasma membrane to the actin cytoskeleton. The I-BAR domain of BAIAP2L2 binds phosphoinositide-containing membranes (Pykalainen *et al.*, 2011), and PI(4,5)P_2 is enriched at stereocilia tips (Hirono *et al.*, 2004; Effertz *et al.*, 2017). Moreover, Ca^{2+} modulates protein interactions with phosphoinositides (Bilkova *et al.*, 2017), so Ca^{2+} influx into stereocilia suggests that transduction could modulate BAIAP2L2's association with the stereocilia tip membrane.

Here we show that the MYO15A-EPS8 complex optimally transports BAIAP2L2 within actin-based projections, and that transduction concentrates BAIAP2L2 at stereocilia tips. We also show that BAIAP2L2 association with the plasma membrane is enhanced when Ca^{2+} is elevated, and that chelation of intracellular Ca^{2+} interferes with BAIAP2L2 localization at stereocilia tips. We therefore suggest that BAIAP2L2 delivered to stereocilia tips by MYO15A-EPS8 complexes is subsequently retained there only if Ca^{2+} entering through open transduction channels produces an environment that favors BAIAP2L2 membrane binding.

Results and Discussion

BAIAP2L2 targeting in stereocilia requires MYO15A, but not EPS8

Because BAIAP2L2 localizes abnormally in null mutants of *Myo15a* and *Eps8* (Carlton *et al.*, 2021), we hypothesized that the MYO15A-EPS8 complex may traffic BAIAP2L2. We tested for the presence of a BAIAP2L2-EPS8 complex in inner hair cells (IHCs) from C57BL/6J mice using a proximity ligation assay (PLA), an antibody-based method for assessing the physical juxtaposition of molecules *in situ* (Soderberg *et al.*, 2006) (Figure 3-1, A-D). As a negative control, minimal signal was observed when PLA was carried out for EPS8 alone (Figure 3-1A). As a positive control, PLA for MYO15A and EPS8 produced strong labeling at row 1 stereocilia tips, as well as lower levels of labeling at row 2 tips (Figure 1B); this distribution was expected given their known locations (Manor *et al.*, 2011; Lin *et al.*, 2021). PLA for the combination of BAIAP2L2 and EPS8 produced discrete labeling at row 2 stereocilia tips (Figure 1D), despite the higher concentration of EPS8 at row 1 stereocilia tips compared to those of row 2. We also examined PLA between BAIAP2L2 and RDX, which is present along stereocilia membranes (Kitajiri *et al.*, 2004). PLA with antibodies for BAIAP2L2 and RDX (Figure 3-1C), which we have previously shown do not interact (Carlton *et al.*, 2021), produced labeling with less marked preference towards either row of stereocilia.

We quantified the PLA signal in these experiments using two different normalization methods; BAIAP2L2-EPS8 PLA signal for row 2 was higher than for row 1 when signal was normalized within a cell (Figure 1E; $p<0.0001$) or across all PLA experiments (Figure 3-1F; $p=0.012$). The former method emphasizes relative differences within a cell, while the latter method also reflects the amplitude of the PLA signal. Although PLA data showed considerable variability (Figure 3-1F and Supplemental Figure 3-1A-C), the results suggested that a BAIAP2L2-EPS8 complex forms in hair cells.

We examined the contributions to BAIAP2L2 trafficking by the short and long MYO15A splice isoforms (Fang *et al.*, 2015; Rehman *et al.*, 2016). We first confirmed that BAIAP2L2 was not detected at stereocilia tips at P5.5 in *Myo15a*$^{sh2/sh2}$ mice (Figure 3-1G), which lack functional MYO15A. We then examined P5 cochleas from *Myo15a*$^{\Delta N}$ mice, which specifically lack MYO15A-1 (Fang *et al.*, 2015). BAIAP2L2 localized to tips of transducing stereocilia in *Myo15a*$^{\Delta N/\Delta N}$ hair bundles, showing that MYO15A-1 is not required for tip targeting; normal targeting must instead require MYO15A-2 or MYO15A-3 (Figure 3-1H).

To examine the role of EPS8 in BAIAP2L2 targeting, we used improved-Genome editing via Oviductal Nucleic Acids Delivery (i-GONAD) (Gurumurthy *et al.*, 2019; Ohtsuka and Sato, 2019) to generate *Eps8*$^{\Delta 818}$, a new *Eps8* mutant allele (Supplemental Figure S1D). Targeting two separate gRNAs to exons 3 and 5, we obtained several G0 pups containing indels. The founder for the selected line, Δ818, contained a large deletion spanning 10,818 base pairs of genomic DNA between exons 3 and 5 (115,524–126,324). EPS8 immunoreactivity was absent in *Eps8*$^{\Delta 818/\Delta 818}$ hair cells (Supplemental Figure 3-1E).

In *Eps8*$^{\Delta 818/\Delta 818}$ mice, we unexpectedly detected BAIAP2L2 signal at the tips of all stereocilia; tip signal was more apparent at P15.5 than P3.5 (Figure 3-1, I and K). As we had previously suggested that BAIAP2L2 was absent from all stereocilia in mice lacking *Eps8* (Carlton *et al.*, 2021), we tested the antibody used previously (Atlas Cat# HPA003043) and found that anti-BAIAP2L2 signal was still present in our *Eps8* knockout, albeit reduced compared to heterozygote littermates (Supplemental Figure 3-1F). These results suggested that MYO15A might traffic BAIAP2L2 without EPS8. Indeed, we found that MYO15A was present at all stereocilia tips in *Eps8*$^{\Delta 818/\Delta 818}$ at both P3.5 and P14.5 (Figure 3-1, J and L).

EPS8 enhances MYO15A-BAIAP2L2 trafficking

To test if BAIAP2L2 could interact directly or indirectly with MYO15A without EPS8, we used nanoscale pulldown (NanoSPD) in HeLa cells to examine the interaction (Bird *et al.*, 2017). In NanoSPD, a filopodia-targeting GFP-MYO10-bait and an RFP-tagged prey protein are co-expressed; if they interact, the GFP-MYO10-bait concentrates the RFP-prey at filopodial tips. *mCherry-Baiap2l2* was co-transfected with either the negative control *gfp-Myo10*(HMM) or with *gfp-Myo10*(HMM)-*Myo15a*(tail); the MYO15A(tail) sequence is shared by all MYO15A splice forms. mCherry-BAIAP2L2 signal at filopodial tips was then quantified. BAIAP2L2 did not target to filopodia tips when expressed with MYO10(HMM) (Figure 3-2A and Supplemental Figure 3-2A), but was often localized at filopodial tips when co-expressed with MYO10(HMM)-MYO15A(tail) (Figure 3-2B and Supplemental Figure 3-2, B and E). Variability in the NanoSPD results meant that filopodial tip enrichment of BAIAP2L2 in the presence of MYO15A was not significant (Figure 3-2F and Supplemental Table 3-1).

EPS8 influences the putative interaction between BAIAP2L2 and MYO15A. We co-transfected *myc-Eps8/P2A/mCherry-Baiap2l2* with either *gfp-Myo10*(HMM)-*Myo15a*(tail) or *gfp-Myo10*(HMM) (Figure 3-2, C and D, and Supplemental Figure 3-2, C and D), and found that BAIAP2L2 targeting to filopodia tips increased with the addition of EPS8. In the absence of MYO15A(tail) and the presence of EPS8 (Figure 3-2C and Supplemental Figure 3-2, C and E), BAIAP2L2 was found at filopodia tips at similar levels as BAIAP2L2 co-expressed with MYO15A(tail) (Figure 3-2F and Supplemental Table 3-1). This result indicates that EPS8 does not require MYO15A(tail) to target to filopodia tips, and is consistent with other observations indicating that EPS8 localizes at the tips of filopodia and microvilli (Figure 3-2E) (Menna *et al.*, 2009; Postema *et al.*, 2018). In the hair bundle, however, EPS8 requires MYO15A to localize to stereocilia tips (Manor *et al.*, 2011). Elevated BAIAP2L2 at filopodia tips with co-expression of EPS8 was also consistent with our previous data demonstrating an interaction between BAIAP2L2 and EPS8.

In the presence of both MYO15A(tail) and EPS8 (Figure 3-2D), BAIAP2L2 was most frequently found at filopodia tips, and was at significantly higher levels than in BAIAP2L2/no-bait (Figure 3-2F, Supplemental Figure 3-2E and Supplemental Table 3-1). BAIAP2L2 transport thus was enhanced by the combined presence of MYO15A and EPS8.

We used *in vitro* pulldown experiments to determine whether EPS8 and MYO15A traffic BAIAP2L2 in a tripartite complex. While MYO15A(tail) did not bind directly to the C-terminal domain of BAIAP2L2, inclusion of full-length EPS8 enabled the co-precipitation of MYO15A(tail) with the C-terminal domain of BAIAP2L2 (Figure 3-2I).

As EPS8 can bind either the N-terminal (Manor *et al.*, 2011) or C-terminal (Lin *et al.*, 2021) MyTH-FERM domains of MYO15A(tail), we sought to determine the BAIAP2L2 binding region within EPS8. Testing the C-terminal domain of BAIAP2L2 against a series of EPS8 truncates using an *in vitro* pulldown assay (Figure 3-2, H and J), we found that the BAIAP2L2 binding region maps to residues 208-310 of EPS8, which includes proline-rich motifs. The full-length EPS8 protein produced the strongest pulldown signal (Figure 3-2J), however, suggesting that other domains may contribute as well.

Our results demonstrate the formation of a tripartite complex of MYO15A, EPS8, and BAIAP2L2 (Figure 3-2K), and suggest that this complex transports BAIAP2L2 in hair bundles. Although the appearance of BAIAP2L2 at all stereocilia tips in *Eps8*-null bundles suggested that it could be trafficked without EPS8, PLA experiments indicated that EPS8 and BAIAP2L2 were localized in close proximity in wild-type row 2 stereocilia. Moreover, EPS8 significantly increased the efficiency of BAIAP2L2 filopodial-tip trafficking in HeLa cells, especially in the presence of MYO15A. By *in vitro* pulldown, BAIAP2L2 and MYO15A were unable to interact directly with each other; while MYO15A might transport BAIAP2L2 in the absence of EPS8, the MYO15A-EPS8 complex transports BAIAP2L2 more efficiently.

Transduction mutants fail to enrich BAIAP2L2

Selective localization of BAIAP2L2 to tips of transducing stereocilia suggested that transduction itself might influence targeting. To test this hypothesis, we examined IHCs from mice lacking different components of the transduction apparatus (Figure 3-5J) and localized BAIAP2L2 by immunocytochemistry. We examined mutant mouse lines lacking either both *Tmc* genes (Figure 3-3, A and B) or *Tmie* (Figure 3-3, C and D), lines that presumably lack the channel pore (Zhao *et al.*, 2014; Kawashima *et al.*, 2015; Pan *et al.*, 2018). We also tested *Pcdh15*^{av3} mice (Figure 3-3, E and F), which lack tip links (Ahmed *et al.*, 2006). We localized BAIAP2L2 in cochleas at P8.5, when hair bundles are still developing, and at P21.5, when bundles are effectively mature (Krey *et al.*, 2020).

As seen previously, BAIAP2L2 localized in heterozygote control IHCs to row 2 and 3 tips; at P8.5, BAIAP2L2 labelling was most apparent at row 2 stereocilia tips, while at P21.5, labelling extended below stereocilia tips and became more evident at row 3 tips as well (Figure 3-3D). In contrast, BAIAP2L2 was absent from all stereocilia tips at both time points in transduction mutants, regardless of which component of the transduction apparatus was absent. Rather than redistributing like other stereocilia proteins (Krey *et al.*, 2020), residual BAIAP2L2 labelling was sparse and no longer row-restricted (Figure 3-3D). BAIAP2L2 localization thus may rely on the active transduction conductance to localize to stereocilia tips.

Maintenance of BAIAP2L2 at stereocilia tips depends on open transduction channels

To confirm that active transduction localizes BAIAP2L2, we tested whether transduction block in cultured cochlear explants from C57BL/6J mice led to redistribution of stereocilia BAIAP2L2 in IHCs. After treatment of P4.5 cochleas for 2 days *in vitro* (DIV) with 100 µM tubocurarine, which effectively blocks transduction currents (Glowatzki *et al.*, 1997; Krey *et al.*, 2020), BAIAP2L2 was no longer detectable in hair bundles (Figure 3-4, A and B, and Supplemental Table 3-1). By contrast, tubocurarine treatment induced no changes in EPS8 distribution (Figure 3-4, A and C, and Supplemental Table S1). Tubocurarine block for 1 DIV similarly reduced BAIAP2L2 at row 2 tips (Supplemental Figure 3-3A).

Past P4.5, hair-bundle morphology is not affected by tubocurarine (Krey *et al.*, 2020). We tested if BAIAP2L2 remained susceptible to transduction block in explants from C57BL/6J mice after the morphology critical period. When block was initiated at P8.5, tubocurarine treatment for 2 DIV still abolished BAIAP2L2 signal from bundles (Figure 3-4, D and E, and Supplemental Table 3-1); as in P4.5+2 DIV bundles, tubocurarine treatment did not alter EPS8 distribution (Figure 3-4F and Supplemental Table 3-1).

We next asked whether the loss of BAIAP2L2 from tips could be reversed by relieving transduction block. Cochleas from P4.5 C57BL/6J mice were cultured in control media or in media with tubocurarine. At 2 DIV, media for all samples was replaced with control media, and explants cultured for 1 additional DIV (Figure 3-4G). BAIAP2L2 and EPS8 were immunolocalized at 2 DIV (pre-washout) and at 3 DIV (1 DIV post-washout) (Figure 3-4H). As before, BAIAP2L2 signal was abolished after 2 DIV with tubocurarine (Figure 3-4I and Supplemental Table 3-1). At 1 DIV post-washout, BAIAP2L2 signal returned to row 2 tips (Figure 3-I and Supplemental Table 3-1). EPS8 row 1 signal remained higher than row 2 signal, regardless of treatment.

These experiments indicated that the association of BAIAP2L2 with stereocilia tips relies on the continuous action of active transduction channels. Acute block of transduction led to loss of BAIAP2L2 even after it had targeted to stereocilia tips, suggesting that BAIAP2L2's maintenance there required open channels. Full restoration of BAIAP2L2 to stereocilia tips after relieving transduction block further reinforced the suggestion that continuous transduction was required for targeting, and raised the possibility that BAIAP2L2's retention at transducing stereocilia may require active transduction throughout the lifetime of the hair bundle. By contrast, localization of EPS8 at the tips of row 1 was largely insensitive to transduction block.

Ca^{2+} retains BAIAP2L2 at stereocilia tips

We hypothesized that BAIAP2L2's retention at stereocilia tips relies on Ca^{2+}-mediated membrane association. To test this model, we expressed BAIAP2L2(I-BAR)-mCherry in HeLa cells (Figure 3-5B) and subjected the transfected cells to treatment with 2 µM ionomycin, a Ca^{2+} ionophore (Liu and Hermann, 1978). We supplemented solutions with either 5 mM EGTA or 20 µM $CaCl_2$ to lower or raise the intracellular Ca^{2+} concentration near the plasma membrane. As a control, cells were also subjected to either 5 mM EGTA or 20 µM $CaCl_2$ with the carrier DMSO in place of ionomycin. As an additional control, we expressed the $PI(4,5)P_2$ sensor PLCD1(PH)-GFP (Varnai and Balla, 1998) in HeLa cells (Figure 3-5A), and subjected the transfected cells to the conditions outlined above.

In the PLCD1(PH)-transfected cells, PH membrane association was evident under all conditions tested (Figure 3-5A). However, treatment with ionomycin and $CaCl_2$ together increased the level of cytoplasmic PH, and resulted in a significantly lower level of PH membrane enrichment than did treatment with DMSO and $CaCl_2$ together (Figure 3-5C and Supplemental Table 3-1). As elevated Ca^{2+} has been shown to inhibit $PI(4,5)P_2$ recognition by PLCD1(PH) (Bilkova *et al.*, 2017), the observed decrease in relative membrane association for ionomycin and $CaCl_2$ together was expected.

In BAIAP2L2(I-BAR)-transfected cells, treatment with ionomycin and $CaCl_2$ together significantly elevated I-BAR membrane enrichment over the other conditions (Figure 3-5D and Supplemental Table 3-1). The I-BAR domain of BAIAP2L2 thus was attracted to plasma membranes when local Ca^{2+} levels were elevated.

To test if BAIAP2L2 localization in hair bundles also displayed Ca^{2+} dependence, we cultured cochlear explants from C57BL/6J mice for 2 DIV in the presence or absence of 20 μM BAPTA-AM, a cell-permeant Ca^{2+} chelator. As before, EPS8 and BAIAP2L2 were immunolocalized after the 2 DIV, and their tip signal quantified (Figure 3-5, G-I). We found that reduction of intracellular Ca^{2+} with BAPTA-AM, like acute channel block, strongly attenuated BAIAP2L2 signal at row 2 tips (Figure 3-5H and Supplemental Table 3-1). Abolition of row 2 BAIAP2L2 tip signal was less complete with BAPTA-AM than with tubocurarine, however, and row 1 BAIAP2L2 tip signal was unexpectedly significantly elevated with BAPTA-AM (Figure 3-5H and Supplemental Table 3-1). BAIAP2L2 was still largely retained at row 2 tips after treatment with BAPTA-AM for 1 DIV (Supplemental Figure 3-3B). The EPS8 signal however, showed no response to the BAPTA-AM treatment (Figure 3-5I and Supplemental Table 3-1). Buffering intracellular Ca^{2+} thus recapitulated the effect of blocking transduction in cochlear explants; when Ca^{2+} was reduced, less BAIAP2L2 was present at row 2 stereocilia tips.

Divalent cations such as Ca^{2+} can induce clustering of phosphoinositides, specifically $PI(4,5)P_2$ (Ellenbroek *et al.*, 2011; Bradley *et al.*, 2020), and lipid recognition by proteins can be modulated by changes in lipid conformation (Bilkova *et al.*, 2017). BAIAP2L2 has no identified Ca^{2+}-binding sites, but does display a broad preference towards phosphoinositide-containing membranes (Pykalainen *et al.*, 2011); the I-BAR domain of BAIAP2L2 may therefore bind clusters of Ca^{2+}-bound phosphoinositides. Alternatively, BAIAP2L2 might be localized at stereocilia tips by CIB2, a Ca^{2+}-sensitive component of the transduction complex (Liang *et al.*, 2021). CIB2 interacts with BAIAP2L2 (Yan *et al.*, 2022); if CIB2 tethers BAIAP2L2 to stereocilia tips, the BAIAP2L2-CIB2 interaction might require Ca^{2+}-bound CIB2.

Conclusions

BAIAP2L2 delivery to tips relies on the MYO15A-EPS8 complex, which is also involved in the targeting of several key proteins in stereocilia (Belyantseva *et al.*, 2005; Manor *et al.*, 2011; Tadenev *et al.*, 2019). MYO15A-2 and EPS8 do not accumulate to high levels at row 2 tips, so once BAIAP2L2 reaches its target, the motor complex may shuttle back to the hair cell's cytoplasm. In *Eps8*-null stereocilia, which have significant transduction currents (Zampini *et al.*, 2011), BAIAP2L2 may depend on a different MYO15A complex to transport it to tips.

BAIAP2L2 is at stereocilia tips only when transduction channels are present and open, which explains why BAIAP2L2 is enriched in transducing stereocilia and not in row 1. In wild-type hair cells, potent buffering of Ca^{2+} (Hackney *et al.*, 2005) and transport by Ca^{2+} pumps (Yamoah *et al.*, 1998) limits Ca^{2+} diffusion and should ensure that membrane-bound BAIAP2L2 remains close to transduction channels. Higher levels of BAIAP2L2 at tips of row 2 versus row 3 may result either from hypothesized elevated Ca^{2+} entry (Krey *et al.*, 2020) or from the flatter membrane at row 2 tips, favored for BAIAP2L2 (Pykalainen *et al.*, 2011). I-BAR proteins like BAIAP2L2 also deform membranes (Mattila *et al.*, 2007; Saarikangas *et al.*, 2010; Zhao *et al.*, 2011), which suggests that BAIAP2L2 could influence the physical state of the stereocilia tip membrane.

Finally, elevated Ca^{2+} enhances association of BAIAP2L2's I-BAR domain with plasma membrane, consistent with the observation that chelation of intracellular Ca^{2+} leads to loss of BAIAP2L2 from stereocilia tips. Although the mechanism by which Ca^{2+} enhances membrane binding of BAIAP2L2 is not known, the slow loss of BAIAP2L2 after transduction block suggests that Ca^{2+}

induces a relatively stable membrane interaction that is not immediately reversed after reduction of Ca^{2+} levels.

In summary, BAIAP2L2 is transported by the MYO15A-EPS8 complex in stereocilia, and is retained selectively at the tips of transducing stereocilia because continuous Ca^{2+} influx through open transduction channels produces an environment that favors association of BAIAP2L2 with the plasma membrane (Figure 5J). Ca^{2+} is thus the transduction-specific factor responsible for retaining BAIAP2L2 at stereocilia tips, and its entry via channels provides the signal to modulate the protein environment at stereocilia tips.

Materials and Methods

Animal lines

All animal procedures were approved by the Institutional Animal Care and Use Committee (IACUC) at Oregon Health & Science University (protocol IP00000714). Mouse pups were assumed to be born at midnight, so the animal age on the first day is referred to as P0.5. Both female and male pups were used for all experiments.

C57BL/6J mice (RRID:IMSR_JAX:000664, Jackson Laboratories, Bar Harbor, ME) were used for localization, proximity ligation, and explant culture assays. BAIAP2L2 localization was assessed in *Myo15a*^{sh2} (RRID:IMSR_JAX:000109, Jackson Laboratories) (Probst *et al.*, 1998) and *Myo15a*$^{\Delta N}$ (Fang *et al.*, 2015) lines, which have been previously described, as well as in *Eps8*$^{\Delta 818}$, which was newly generated via i-GONAD (Ohtsuka and Sato, 2019). *Myo15a*$^{\Delta N}$ tissue was a kind gift from Jonathan Bird. BAIAP2L2 localization was also assessed in *Tmc1*^{KO} and *Tmc2*^{KO} double knockout (Kawashima *et al.*, 2015), *Tmie*^{KO} (Zhao *et al.*, 2014), and *Pcdh15*^{av3} (Pawlowski *et al.*, 2006) lines. Animals have been maintained on a C57BL/6J background. *Myo15a*$^{\Delta N}$, *Tmc* double KO, *Tmie*^{KO}, *Pcdh15*^{av3} mice were genotyped using previously described primers (Pawlowski *et al.*, 2006; Zhao *et al.*, 2014; Fang *et al.*, 2015; Kawashima *et al.*, 2015). Genotyping of *Myo15a*^{sh2} mice was performed by TransnetYX, Inc. (Cordova, TN). *Eps8*$^{\Delta 818}$ mice were genotyped using the following primers: wild-type forward primer (exon 3): 5'-AAG GCT CTG GCT TTC CTC TG-3', wild-type reverse primer (exon 3): 5'-TGA TTG AAA CAT CAT CCC TTG GG-3', and wild-type reverse primer (exon 5): 5'-CAG GGG TCG TTG TGA TTC CA-3'; the sequence targeted by wild-type reverse primer (exon 3) is lacking in *Eps8*$^{\Delta 818}$ mice. Phenotypes in all mutants were obvious so blinding to genotype was impossible.

Generation of *Eps8*$^{\Delta 818}$

The *Eps8* locus was targeted for CRISPR-mediated knockout using guide RNAs (gRNAs) designed to exons 3 and 5 (http://crispor.tefor.net/). gRNAs were delivered via in situ electroporation using the i-GONAD procedure (Gurumurthy *et al.*, 2019; Ohtsuka and Sato, 2019). Necessary components, including guides (Alt-R CRISPR-Cas9 crRNA, exon 3 guide—ATATGTCTAACCGCTCCAGT, exon 5 guide—TCTTACTTCCACGCGGTACT), tracrRNA (Cat# 1072532), and Cas9 protein (Cat# 1081060) were obtained from Integrated DNA technologies (IDT). Timed crosses with 2 female and 1 male C57BL/6J mice were set for an E0.7 pregnancy. At this point in pregnancy, the zygote is at the single-cell stage and has lost its cumulus cells, allowing higher efficiency electroporation of the zygotes (Gurumurthy *et al.*, 2019). Pregnancy was confirmed by checking plugs. Ribonucleoprotein (RNP) was prepared. To anneal tracrRNA and crRNA, tracrRNA, and crRNA were mixed to a final concentration of 60 and 30 μM respectively in Duplex buffer (IDT Cat# 1072570), then heated to 95 ˚C and allowed to cool slowly back to room temperature. Cas9 protein was added at a final concentration of 1.5 μg/ml to the annealed tracrRNA/crRNA mix, and the sample heated to 37 ˚C and allowed to cool slowly back to room temperature. Fast Green (Fisher Scientific Cat# 2353-45-9) was prepared in Duplex buffer, and then sterile filtered through a 0.22 μm filter (Millipore Cat# SLGP033RS). Filtered Fast Green was added at 3 mg/ml to the RNP sample so that the mixture could be visualized, once injected within the oviduct. To prepare for electroporation of RNPs, pregnant dams (E0.7) were given an intraperitoneal injection of anesthetic (working stock: 9 mg/ml Nembutal, Sigma Cat# P37610; 20.8 mg/ml $MgSO_4$, Sigma Cat# 63138; 10% ethanol, Sigma Cat# 459836; 40% propylene glycol, Fisher Scientific Cat# P335-1) at 7.8 μl per gram body weight; anesthesia was confirmed by the lack of toe pinch reflex. Surgery was performed to expose the ovary and oviduct, and an estimated 0.5 to 1 µl of the RNP mixture injected into the lumen of the oviductal ampulla. The paddles of the electrode were placed around the portion of the oviduct where the Fast Green was visible, and electroporation performed, using 3 pulses of 5 ms On and 50 ms Off at 30 V. The range of currents achieved under this protocol was from 100-500 mA; optimal surgeries were in the range of 150-250 mA. After electroporation, ovary and oviduct were gently returned to the abdominal cavity, and the incision closed with two stitches and a wound clip. Throughout the surgery, tissue was kept hydrated with prewarmed Lactated Ringers Solution (Baxter Cat# 2B2323). For the first 3 days after surgery, dams were treated with a dose of Meloxicam (MWI Animal Health Cat# 501080) at 1 µl per gram body weight for pain management; the first dose was administered soon after surgery was complete. G0 pups were screened for mutations by PCR and sequencing. Genomic DNA was extracted from G0 tissue samples; using primers set to amplify any sequence containing a deletion between the targeted exons, PCR was performed, amplicons were gel-purified, and then were sequenced. A founder containing a large deletion spanning 10,818 base pairs of genomic DNA between exons 3 and 5 was identified, backcrossed on to the C57BL/6 background, and propagated as the Δ818 line used in this study. This mouse line is available upon reasonable request.

Cell lines

For nanoscale pulldown experiments and plasma membrane association studies, HeLa cells were obtained directly from ATCC (ATCC, CCL-2; RRID:CVCL_0030). For protein production, HEK 293T/17 cells were obtained directly from ATCC (ATCC, CRL-11268; RRID:CVCL_1926). Cells were cultured at 37°C (5% CO_2) in Eagle's Minimum Essential Medium (EMEM) (Fisher Scientific Cat# 30-2003) supplemented with 10% Serum Plus Medium Supplement (Sigma Aldrich Cat# 14008C), 100 units/ml penicillin-G and 100 µg/ml streptomycin (Sigma-Aldrich Cat# P4333). All experiments in

HeLa cells were conducted between passages 10-40; HEK293T/17 cells were used to produce protein at passage 9. Cultures were confirmed mycoplasma-negative with the LookOut Mycoplasma PCR Detection Kit (Millipore Sigma Cat# MP0035).

Immunofluorescence localization

For immunofluorescence, inner ears were isolated from mice of the indicated ages and genotypes and dissected in cold Hank's balanced salt solution (Thermo Fisher Scientific Cat# 14025076) supplemented with 5 mM HEPES, pH 7.4. During inner ear dissection, small openings were made in the periotic bones to allow perfusion of the fixative. Ears were fixed in 4% formaldehyde (Electron Microscopy Sciences Cat# 1570) in 1X PBS for 25 minutes at room temperature and washed twice for 5 minutes each in 1X PBS; cochleas were then dissected from periotic bones and the lateral wall removed. Cochleas were permeabilized in 0.2% Triton X-100 in 1X PBS for 10 minutes, blocked in 5% normal donkey serum (Jackson ImmunoResearch Cat# 017-000-121) diluted in 1X PBS (blocking buffer) for 1 hour at room temperature, and then incubated overnight at 4°C with primary antibodies diluted in blocking buffer. Samples were washed two times in 1X PBS after incubation with primary antibodies. Dilutions were 1:200 for anti-BAIAP2L2 (Abcam Cat# ab224323), 1:150 for the Atlas anti-BAIAP2L2 (Sigma-Aldrich Cat# HPA003043, RRID:AB_2227864), and 1:250 for both anti-EPS8 (BD Transduction Laboratories Cat# 610143; RRID:AB_397544) and anti-pan-MYO15A (PB48, Thomas Friedman lab). The BAIAP2L2 antibodies were validated in this study and in our previous report (Carlton *et al.*, 2021); the EPS8 antibody was validated here; and the MYO15A antibody was validated previously (Belyantseva *et al.*, 2003). Cochleas were then incubated with secondary antibodies, which were either 2 mg/ml donkey anti-mouse Alexa Fluor 488 (Thermo Fisher Scientific Cat# A21202; RRID:AB_141607) or 2 mg/ml donkey anti-rabbit Alexa Fluor 568 (Thermo Fisher Scientific Cat#

A10042; RRID:AB_2534017), for 3-4 hours at room temperature; 1 U/ml CF488A phalloidin (Biotium Cat# 00042) was also included for single-antibody experiments during the incubation with secondary antibodies, while 1 U/ml CF405 phalloidin (Biotium Cat# 00034) was instead included for two-antibody experiments. Tissue was washed three times in 1X PBS and mounted on a glass slide in approximately 50 µl of Vectashield (Vector Laboratories Cat# H-1000) and covered with a #1.5 thickness 22 x 22 mm cover glass (Corning Cat# 2850-22). Cochlear hair bundles were imaged using a 63X, 1.4 NA Plan-Apochromat objective on a Zeiss LSM980 system equipped with an Airyscan2 detector and ZEN 3.3 (blue edition, 64-bit software; Zeiss, Oberköchen, Germany) acquisition software. Manufacturer-suggested settings for optimal Nyquist-based resolution were used for x-y pixel resolution, z-spacing, as well as pinhole diameter. Raw data processing for Airyscan-acquired images was performed using manufacturer-implemented automated settings. For each antibody, 2-3 images were acquired from 1-3 cochlea per genotype per age for each experiment, and experiments were conducted at least twice. Ears from control and mutant littermates were stained together and imaged together for each experiment to limit variability. During image acquisition, the gain and laser settings for the antibody and phalloidin signals were set to reveal the staining pattern in control samples, and the corresponding mutant samples used the same settings. Display adjustments in brightness and contrast were made using Fiji/ImageJ software, as were maximum, average, and/or sum Z-projections.

For proximity ligation assays, tissue processing and staining with primary antibodies was performed as outlined above. The anti-BAIAP2L2, anti-EPS8, anti-pan-MYO15A antibodies were used at the same dilutions as above, and anti-RDX (Abnova Cat# H00005962-M06; RRID:AB_464027) was used at 1:100. After incubation with primary antibodies, proximity ligation was performed according to the manufacturer's specifications (Duolink In Situ PLA; Sigma Aldrich Cat#s DUO92004, DUO92002, DUO92008). Counterstaining with 1 U/ml CF488A phalloidin was performed as described above, and samples were imaged with the same considerations as detailed above.

Expression constructs

PCR amplification and cloning were performed using standard methods, and expression constructs were verified by Sanger sequencing. Plasmid DNA for transfection of mammalian cells was prepared using endotoxin-free purification kits (Plasmid Plus Midi Kit, Qiagen Cat# 12943). Plasmid DNA for transformation of BL21(DE3) *Escherichia coli* (New England Biolabs Cat# C2527) was prepared using smaller scale purification kits (ZR plasmid Miniprep Cat# Fisher Scientific, D4016).

For nanoscale pulldown, the GFP-tagged MYO10 heavy meromyosin (HMM) [*Gfp-Myo10*(HMM)] construct (aa 1-946, NP_776819) was a kind gift from Richard Cheney; this construct encompasses the MYO10 ATPase motor and three tandem IQ motifs. A MYO15A(tail) construct (aa 1973-2943, NP_001096641) [*gfp-Myo15a*(tail)] was a kind gift from Jonathan Bird, and includes two MyTH-FERM repeats and an SH3 domain. To create a bait construct for nanoscale pulldown (Bird *et al.*, 2017), *Myo15a*(tail) was fused to *Myo10*(HMM) [*gfp-Myo10*(HMM)-*Myo15a*(tail)]. Two prey constructs were created—one expressing BAIAP2L2 N-terminally tagged with mCherry (*mCherry-Baiap2l2*), and the other expressing EPS8 N-terminally tagged with myc (myc-*Eps8*) and mCherry-BAIAP2L2 separated by a self-cleaving P2A peptide [*myc-Eps8/P2A/mCherry-Baiap2l2*]. Construct schematics are shown in Figure 3-2G.

For *in vitro* pulldown, the GST-tagged BAIAP2L2 C-terminal domain and 6xHis-2xHA-tagged EPS8 constructs were the same used previously (Carlton *et al.*, 2021). Deletion truncates of EPS8 were generated from the original 6xHis-2xHA-tagged EPS8 construct using a commercial mutagenesis kit

(Q5 Site-Directed Mutagenesis Kit; New England Biolabs Cat# E0554S). GST alone was expressed from an empty pGEX-4T3 vector (Cytiva, Cat# GE28-9545-52). GFP-MYO15A(tail) was expressed from the plasmid provided by Jonathan Bird. Construct schematics are shown in Figure 3-2H.

For plasma membrane association studies, the I-BAR domain of BAIAP2L2 (aa 1-261, NP_808248) was cloned into a pRP[Exp]-CMV backbone with a C-terminal mCherry tag [*Baiap2l2*(I-BAR)-*mCherry*]. *Plcd1*(PH)-*gfp* was a gift from Tamas Balla (PH-PLCD1-GFP, Addgene plasmid # 51407, http://n2t.net/addgene:51407, RRID:Addgene_51407).

Nanoscale pulldown

HeLa cells were double transfected using Lipofectamine 3000 (Thermo Fisher, L3000015) as detailed. Plasmid pairs were as follows: (a) *Gfp-Myo10*(HMM) + *mCherry-Baiap2l2*, (b) *Gfp-Myo10*(HMM)-*Myo15a*(tail) + *mCherry-Baiap2l2*, (c) *Gfp-Myo10*(HMM) + *myc-Eps8/P2A/mCherry-Baiap2l2*, (d) *Gfp-Myo10*(HMM)-*Myo15a*(tail) + *myc-Eps8/P2A/mCherry-Baiap2l2*. Cells were incubated at 37°C for approximately 24 hours post-transfection before being trypsinized and re-seeded onto #1.5 thickness glass coverslips coated in 0.025 mg/ml poly-L-lysine (Sigma Aldrich, P1274). Re-seeded cells were further incubated at 37°C for another 24 hours, and then washed once in 1X PBS, and fixed for 15 minutes in 4% formaldehyde at room temperature. Fixed cells were washed three times in 1X PBS before permeabilizing in 0.1% Triton-X100 in 1X PBS for 10 minutes, and then incubated with 1 U/ml CF405 phalloidin in 1X PBS for 2-3 hours at room temperature. Cells were washed three times in 1X PBS, and coverslips mounted in Everbrite mounting medium (Biotium Cat# 23005). Imaging was performed on the same setup described above. Cells were imaged such that the field of view contained 1-2 cells with clearly extended filopodia that did not contact other cells, and so the z-stack encompassed the filopodia (i.e. the entire cell body was not imaged).

In vitro pulldown with recombinant proteins

Pulldown assays were performed as described previously (Carlton *et al.*, 2021). Briefly, expression of GST alone, GST-tagged BAIAP2L2 C-terminal domain (CT, residues 262-522), and 6xHis-2xHA-tagged EPS8 constructs (residues 1-821 [full-length protein], 1-520, 208-520, 310-520, and 521-821) was induced in BL21(DE3) competent *Escherichia coli* by the addition of 0.5 mM isopropyl *β*-d-1-thiogalactopyranoside (Sigma-Aldrich Cat# I-6758) and allowed to continue overnight at 25°C. To produce GFP-MYO15A(tail) protein, HEK293T/17 cells were transfected with *gfp-Myo15a*(tail) using Lipofectamine 3000 and allowed to express for 24 hours. Cell extracts were prepared by sonication of cells resuspended in 1X PBS supplemented with a protease inhibitor cocktail (Sigma-Aldrich, P8465) and 0.5% Triton X-100. Sonicates were clarified by centrifugation at 12,000 x g for 30 minutes, and the supernatants (clarified extracts) were assessed for expression levels by immunoblotting prior to use in pulldown assays. Glutathione Sepharose 4B beads (Millipore Sigma Cat# 17-0756-01) were incubated with clarified bacterial extracts for 1 hour at room temperature to load GST or GST-tagged BAIAP2L2 CT. GST-loaded beads were then washed in PBS for 3 x 5 minutes at 500 x g. To test if a tripartite complex between MYO15A, EPS8 and BAIAP2L2 could be formed (Figure 3-2I), the GST-loaded beads were then incubated with MYO15A-containing lysate in the absence or presence of EPS8. To map the EPS8-BAIAP2L2 interaction (Figure 2J), the GST-loaded beads were then incubated for 1 hour at room temperature with EPS8-containing extracts to allow EPS8 binding of GST-tagged bait protein. Unbound proteins were removed by washing in PBS for 3 x 5 minutes at 500 x g. Beads were transferred to spin columns, incubated for 10 minutes with hot 2X LDS sample buffer (Invitrogen Cat# NP0007), and then spun for 5 minutes at 1000 x g to elute complexes into 2X reducing agent (Invitrogen, NP0009). Pulldown samples (20% of total eluate) and input lysates (1% of sample applied to beads) were analyzed by immunoblotting and detected with rabbit anti-GST (Santa Cruz Cat# sc-33613; RRID:AB_647588), mouse anti-6xHis (Proteintech Cat# 66005-1; RRID:AB_11232599), or mouse anti-GFP (Santa Cruz Cat# sc-9996; RRID:AB_627695).

Cochlear explants

Explants were prepared essentially as described (Krey *et al.*, 2020). Briefly, C57BL/6J mice were sacrificed at P4.5 or P8.5 using cervical dislocation, and the head removed and surface sterilized by immersion in 70% ethanol for ~30 seconds. The heads were then allowed to air dry for approximately 30 seconds, then they were bisected along the mid-sagittal plane and placed into DMEM/F12 containing L-glutamine and 15 mM HEPES (Sigma Aldrich Cat# D8062) supplemented with 10 mM sodium pyruvate (Thermo Fisher Scientific Cat#, 11360-070) and 30 µM penicillin G (Sigma-Aldrich Cat# P3032) (solution 1) for microdissection. The otic capsule was dissected out from the temporal bone and placed in a new dish with solution 1 before removing the cartilaginous capsule surrounding the cochlea and the stria vascularis. A stainless steel minutien pin (0.02 mm tip diameter, 0.2 mm rod diameter, 10 mm length; Fine Science Tools Cat# 26002-20,) was placed through the modiolus. The minutien pin was then secured to a custom sterile plastic tissue chamber (5-6 mm depth and 9 mm diameter; 200 µl volume) and was transferred to a well in a 24-well plate containing 1 ml of solution 1. Solution 1 was replaced 2 times with DMEM/F12 supplemented with 10 mM sodium pyruvate, 30 µM penicillin G, and the same growth factors at the same concentrations used previously (solution 2). Solution 2 had either the presence or absence of a drug (either 100 µM tubocurarine (Sigma Aldrich Cat# T2379) or 20 µM BAPTA-AM (Cayman Chemical Cat# 15551). The two cochleas from the same animal were given different treatments (control or drug). Tissues were then incubated at 37°C (5% CO_2) for approximately 48 hours, and then fixed in 4% formaldehyde solution for 25 minutes at room temperature. For the wash-in/wash-out experiment shown in Figure 4, G-J, explants were not fixed after 48 h *in vitro*; instead, the culture solution was removed, exchanged 3 times with fresh solution 2 without tubocurarine, then incubated for one additional day *in vitro* at 37°C (5% CO_2) before fixation in 4% formaldehyde solution for 25 minutes at room temperature. Fixed explants were washed twice for 5 minutes each in 1X PBS, and then removed from their minutien pins to complete the microdissection of the organ of Corti. Explants were stained against BAIAP2L2 and EPS8 using the immunofluorescence and Airyscan imaging protocols described above; images were exclusively collected from the middle turn of the cochlea, as this region of tissue was disturbed the least during the process of placing cochleas into culture.

Plasma membrane association studies

HeLa cells seeded on #1.5 thickness glass coverslips coated in 0.025 mg/ml poly-L-lysine were transfected with either *Plcd1*(PH)-*gfp* (Addgene Cat# 51407) or *Baiap2l2*(I-BAR)-*mCherry* again using Lipofectamine 3000, and then incubated at 37°C (5% CO_2) for approximately 24 hours. After the 24-hour incubation, cells were treated with (a) 0.2% DMSO (Sigma Aldrich Cat# D8418) + 5 mM EGTA (Sigma Aldrich Cat# E4378), (b) 2 μM ionomycin (Sigma Aldrich Cat#, I3909) + 5 mM EGTA, (c) 0.2% DMSO + 20 μM $CaCl_2$ (Fisher Chemical Cat# C79), (d) 2 μM ionomycin + 20 μM $CaCl_2$ for 30 minutes at 37°C (5% CO_2). As ionomycin selectively transports Ca^{2+} into the cytosol (Liu and Hermann, 1978), these conditions allowed the comparison of the effect on I-BAR or PH membrane association produced by raising or lowering the local Ca^{2+} concentration near the plasma membrane. After treatment, cells were processed as described above for nanoscale pulldown experiments, and imaged on the same setup. Fields of view were selected to include 1-2 cells, z-stacks were set to encompass the majority of the cell body, and 3-6 cells were imaged per condition. Each treatment condition was repeated 3 times.

Quantification and data analysis

All data based on fluorescence intensity was collected in ImageJ (http://rsbweb.nih.gov/ij/), and analyzed in Excel (Microsoft) and Prism (Graphpad). Prism was used to prepare all plots and to perform any statistical analyses. To determine the appropriate statistical test, the normality of all data was assessed by applying the Shapiro-Wilk test in Prism. For all experiments, data from at least one of the conditions failed normality; accordingly, the non-parametric Kruskal-Wallis test with Dunn's multiple comparisons was used to evaluate differences among groups.

Nanoscale pulldown results were assessed largely as described (Bird *et al.*, 2017) (https://github.com/NanoSPD/NanoSPD/tree/master/macro). Sum projections of 2-4 slices of 0.15 μm thickness were used to fully span all filopodia. Using the sum projections, average line scans (line thickness = 20) along filopodia, starting at the cell body and extending a few micrometers past the filopodia tip, using the GFP and phalloidin signal as guides, were also prepared. The mCherry channel was turned off during tracing to avoid selection bias. Only filopodia >2 μm away from the cell body were analyzed, and a maximum of 10 filopodia were sampled per cell. GFP and mCherry line scan values were exported from ImageJ into an Excel file. In the Excel file, all line scan values were normalized by dividing the value at each position by the average signal across the entire scan to control for differing expression levels of GFP bait protein and mCherry-BAIAP2L2 from cell to cell. The maximum of the normalized GFP signal was used to determine the position of the filopodia tip. To capture the entire filopodia tip, index matching was used to retrieve the normalized mCherry signal for all positions ± 0.16 μm about the maximum GFP signal. The retrieved values were summed, and the result considered the mCherry tip signal for a given filopodium. Tip signal was averaged for each cell.

Stereocilia tip signal intensity was assessed for signal obtained with PLA. Average projections of ~10-20 slices of 0.15 μm thickness encompassing the hair bundle from stereocilia tips to apical surface of the hair cell were created. The range in slice thickness used was due to variations in bundle orientation. Using a circular region of interest (ROI), PLA signal was measured at stereocilia tips. Six to eight stereocilia were measured from row 1 and row 2 per inner hair cell, and ROI area and mean gray value were recorded for each tip, as well as the number of slices used to generate the average projection. For each stereocilia tip ROI, a background ROI was also measured. Raw tip signal was computed as the ROI area multiplied by tip gray value minus background gray value, and then multiplied by the number of slices used for the projection. For any tips where the calculation resulted in a negative number, the value was replaced with zero. Quantified PLA signal was then normalized in two separate ways. First, measured tip signal was normalized to the average of all tips measured for a cell to account for variability of the same PLA assay pair from experiment to experiment. Second, all PLA signals were normalized to the average of all MYO15A-EPS8 PLA signals, the most consistent of the antibody pairs, to compare the signal levels between different antibody pairs. Average row 1 and average row 2 signals for each cell were calculated from the normalized values from both methods.

Stereocilia tip signal intensity for anti-BAIAP2L2 and anti-EPS8 was assessed in cochlear explants, largely using the same method outlined above. To control for staining variability across experiments, average tip signal intensity was computed for all control tips in a given experiment (a set of explants dissected and placed into culture on the same day) were averaged; all tip values within the given experiment were then divided by this average control value to normalize signals. Average row 1 and average row 2 signals for each cell were calculated from the normalized values.

Plasma membrane association of PLCD1(PH)-GFP or BAIAP2L2(I-BAR)-mCherry was assessed by comparison of signal intensity at the plasma membrane to signal intensity within the cytoplasm. Sum projections of 3-6 slices of 0.15 μm thickness were prepared to capture a middle section of the cell body, such that the membrane closest to the coverslip was excluded. Using the sum projections, average line scans (line thickness = 10) were prepared; lines were drawn starting inside the cell body and extended a few micrometers past the cell border as demarcated by the phalloidin (F-actin) signal. The mCherry or GFP channel was turned off during tracing to avoid selection bias. Four scans were acquired for each cell. GFP/mCherry and phalloidin line scan values were exported from ImageJ into an Excel file. In the excel file, the peak of the phalloidin signal was interpreted as the cortical actin at cell border, and used as a proxy for the plasma membrane (Koster and Mayor, 2016). For each line scan, mCherry or GFP signal was summed over a 1 μm segment either at the phalloidin peak to capture the plasma membrane-associated signal (Figure 3-4, E and F; tan boxes) or within the cell body to capture the cytoplasmic signal (Figure 3-4, E and F; aqua boxes); membrane-associated signal was then divided by cytoplasmic signal to find the ratio of membrane-associated to cytoplasmic signal. Ratios were averaged for each cell analyzed. PLCD1(PH) and BAIAP2L2(I-BAR) results were analyzed separately.

Experimental replicates and n

(Figure 3-1, A-F) PLA performed 3-5 times for each antibody combination; each experiment used cochleas from 4-6 littermates; 19-62 IHCs analyzed per condition.

(Figure 3-1, G-L) Immunostaining experiments were conducted 2-3 times for each age and genotype; each experiment analyzed at least two animals per genotype from the same litter.

(Figure 3-2, A-F) Transfections for nanoscale pulldown were conducted 3-5 times, 12-22 cells were analyzed per condition (4-6 cells analyzed per condition per experiment).

(Figure 3-2, I and J) Pulldown by BAIAP2L2 C-terminal domain conducted 2-3 times for each condition.

(Figure 3-3) Immunostaining experiments were performed at least twice for each age and genotype; each experiment analyzed at least two animals per genotype from the same litter.

(Figure 3-4B) 46-55 IHCs analyzed per condition, pooled from 3 experiments with 3-4 littermate animals used per experiment.

(Figure 3-4C) 27-32 IHCs analyzed per condition, pooled from 2 experiments with 3-4 littermate animals used per experiment.

(Figure 3-4, E and F) 18-26 IHCs analyzed per condition, pooled from 2 experiments with 3-4 littermate animals used per experiment.

(Figure 3-4, I and J) 20-29 IHCs analyzed per condition, pooled from 2 experiments with 6-8 littermate animals used per experiment.

(Figure 3-5, A and C) 13-20 cells analyzed per condition, pooled from 3 experiments.

(Figure 3-5, B and D) 18-33 cells analyzed per condition, pooled from 3 experiments.

(Figure 3-5, G-I) 51-56 IHCs analyzed per condition, pooled from 3 experiments with 3-4 littermate animals used per experiment.

Comparisons and n used for each experimental condition are indicated in Supplemental Table 3-1.

Online supplemental material

Three figures and one table are included in the supplemental material.

Supplemental Figure 3-1 shows the range of signal obtained with PLA, the targeted region of the *Eps8* gene for knockout generation via i-GONAD, loss of EPS8 immunoreactivity in the new knockout, and a comparison of the Atlas and Abcam BAIAP2L2 antibodies in the new *Eps8* knockout.

Supplemental Figure 3-2 includes additional nanoscale pulldown data, an alternate presentation of the data in Figure 3-2F, and example immunoblots showing immobilized GST bait protein for the pulldown experiments shown in Figure 3-2, I and J.

Supplemental Figure 3-3 shows the effect of shorter culture period (1 DIV) with tubocurarine or BAPTA-AM on BAIAP2L2 tip enrichment.

Supplemental Table 3-1 contains descriptive statistics (n, median, 25th and 75th percentile) and results of statistical analyses performed for data shown in Figures 3-1, 3-2, 3-4 and 3-5. All data was analyzed by Kruskal-Wallis tests, followed by Dunn's multiple comparisons.

Acknowledgments

Jennifer Goldsmith provided excellent mouse husbandry. Jonathan Bird kindly provided us with *Myo15a*$^{\Delta N}$ tissue and the *egfp-Myo15a*(tail) plasmid; the *Gfp-Myo10*(HMM) plasmid was a gift from Richard Cheney. The pan-MYO15A antibody was generously provided by Tom Friedman. We thank Andy Griffith for the *Tmc1*$^{\mathrm{KO}}$ and *Tmc2*$^{\mathrm{KO}}$ mouse lines, and Uli Müller for the *Tmie*$^{\mathrm{KO}}$ mouse line. Confocal microscopy was performed at the OHSU Advanced Light Microscopy Core @ The Jungers

Center (supported by P30 NS061800). The study was supported by a grant to P. G. Barr-Gillespie (National Institutes of Health, R01DC002368).

Source data

Contains uncropped and unprocessed images with annotations for blots displayed in Figures 2I, 2J and S2F, S2G.

Author contributions

Conceptualization—Peter Barr-Gillespie, Julia Halford

Data curation—Julia Halford

Formal analysis—Julia Halford

Funding acquisition—Peter Barr-Gillespie

Investigation—Julia Halford, Michael Bateschell

Methodology—all authors

Project administration—Peter Barr-Gillespie

Resources—Peter Barr-Gillespie, Michael Bateschell

Software—n/a

Supervision—Peter Barr-Gillespie

Validation—Julia Halford (*Eps8*$^{\Delta818}$ loss of immunoreactivity), Michael Bateschell (*Eps8*$^{\Delta818}$ sequencing)

Visualization—Julia Halford, Peter Barr-Gillespie

Writing (original draft)— Julia Halford, Peter Barr-Gillespie

Writing (review & editing)—all authors

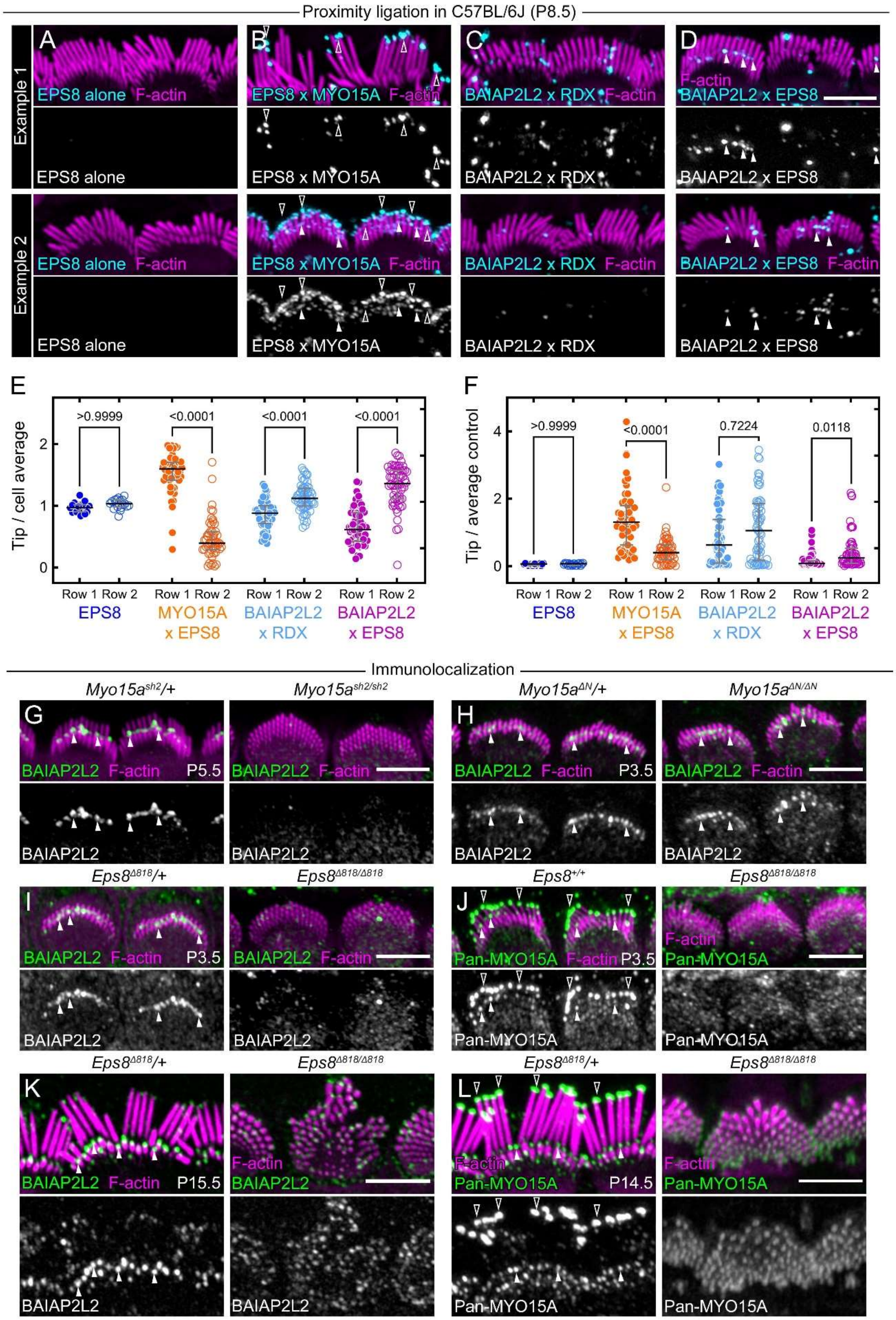
Proximity ligation in C57BL/6J (P8.5)
Example 1
Example 2
A
B
C
D
EPS8 alone F-actin
EPS8 alone
EPS8 x MYO15A F-actin
EPS8 x MYO15A
BAIAP2L2 x RDX F-actin
BAIAP2L2 x RDX
F-actin
BAIAP2L2 x EPS8
BAIAP2L2 x EPS8 F-actin
E
Tip / cell average
>0.9999
<0.0001
<0.0001
<0.0001
0
1
2
Row 1 Row 2
EPS8
MYO15A x EPS8
BAIAP2L2 x RDX
BAIAP2L2 x EPS8
F
Tip / average control
>0.9999
<0.0001
0.7224
0.0118
0
2
4
Immunolocalization
Myo15a^sh2/+
Myo15a^sh2/sh2
Myo15a^ΔN/+
Myo15a^ΔN/ΔN
G
H
BAIAP2L2 F-actin
P5.5
P3.5
BAIAP2L2
Eps8^Δ818/+
Eps8^Δ818/Δ818
Eps8^+/+
I
J
Pan-MYO15A F-actin
P3.5
Pan-MYO15A
K
L
P15.5
P14.5

Figure 3-1. BAIAP2L2 localizes with EPS8 but does not require it for targeting.

(A-D) PLA in P8.5 C57BL/6J IHCs. (A) Single primary antibody (anti-EPS8). (B) Anti-MYO15A and anti-EPS8. (C) Anti-RDX and anti-BAIAP2L2. (D) Anti-BAIAP2L2 and anti-EPS8. Examples from two separate experiments are included to show range of signal. (E, F) Quantification of PLA signal, normalized by cell (E), or normalized by MYO15A-EPS8 signal per experiment (F). Data plotted with median and interquartile range (IQR); individual points are average stereocilia tip signal at row 1 or row 2 per cell. Data were analyzed by Kruskal-Wallis tests, followed by Dunn's multiple comparisons; P values indicated in plot (Supplemental Table S1 for details). (G-I, K) Anti-BAIAP2L2 signal in heterozygote and knockout IHCs. (G) *Myo15a*^{sh2}*/+*, *Myo15a*$^{sh2/sh2}$; P5.5. (H) *Myo15a*$^{\Delta N}$*/+*, *Myo15a*$^{\Delta N/\Delta N}$; P5. (I) *Eps8*$^{\Delta 818}$*/+, Eps8*$^{\Delta 818/\Delta 818}$; P3.5. (K) *Eps8* $^{\Delta 818}$*/+, Eps8* $^{\Delta 818/\Delta 818}$; P15.5. (J) Anti-MYO15A signal in *Eps8*$^{+/+}$*, Eps8* $^{\Delta 818/\Delta 818}$; P3.5. (L) Anti-MYO15A signal in *Eps8*$^{\Delta 818}$*/+, Eps8*$^{\Delta 818/\Delta 818}$; P14.5. Antibody signal intensity was matched between heterozygote and knockout pairs in each panel, but was not comparable across ages or across mutants. Empty arrowheads at row 1 tips, solid arrowheads at row 2 tips. Scale, 5 µm.

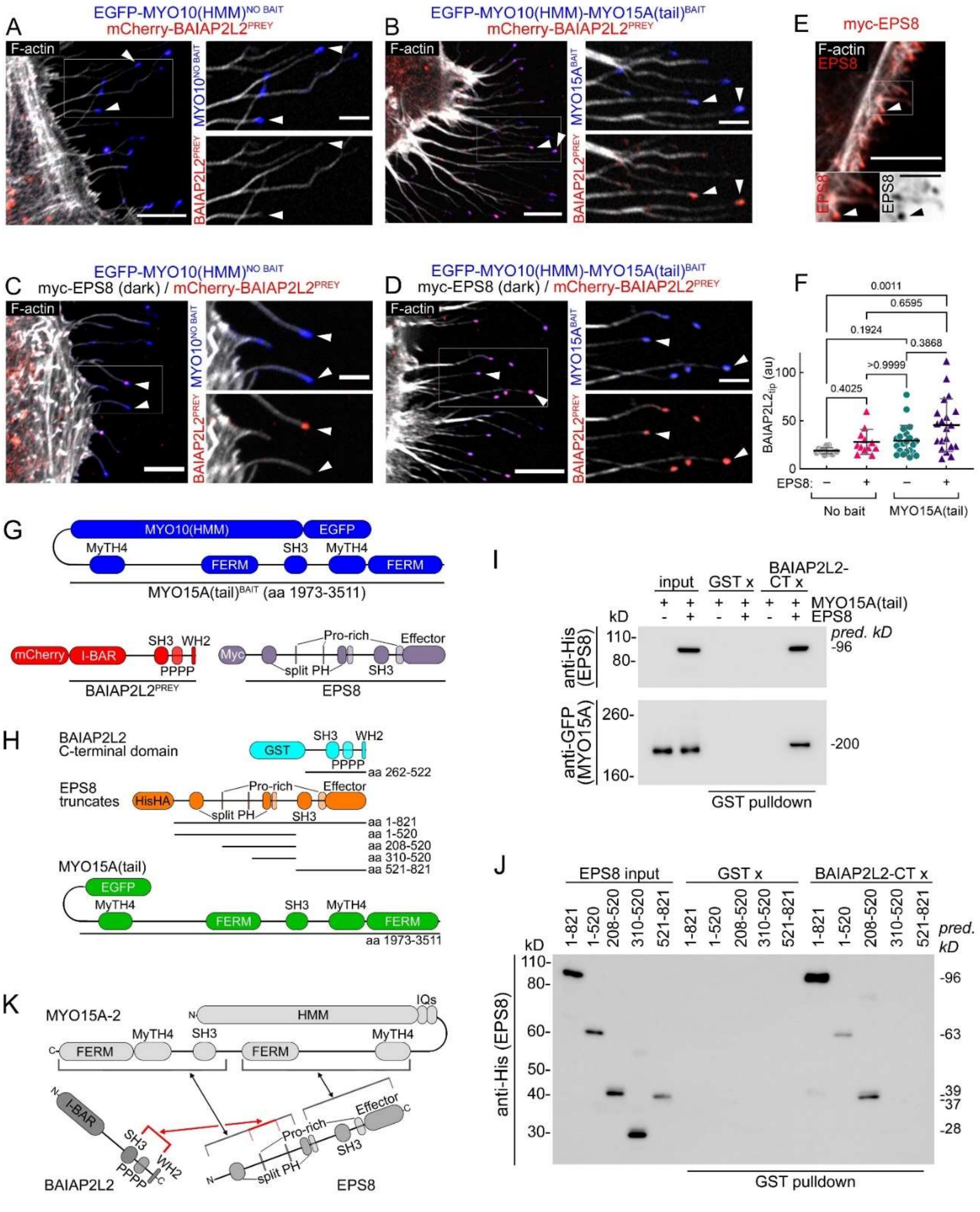

Figure 3-2. MYO15A, EPS8, and BAIAP2L2 form a tripartite complex.

(A-G) NanoSPD in HeLa cells. (A-B) mCherry-BAIAP2L2^{PREY} co-expressed with (A) EGFP-MYO10$^{NO\text{-}BAIT}$ or (B) EGFP-MYO10-MYO15A(tail)^{BAIT}. (C-D) Myc-EPS8 and mCherry-BAIAP2L2^{PREY} co-expressed with (C) EGFP-MYO10$^{\text{NO-BAIT}}$ or (D) EGFP-MYO10-MYO15A(tail)$^{\text{BAIT}}$. Myc-EPS8 and mCherry-BAIAP2L2 were expressed using a P2A-linked bicistronic plasmid. (E) myc-EPS8 expressed alone. Scale, 5 μm in micrographs on the left side of each panel or 2 μm in enlarged insets. (F) Quantitation of BAIAP2L2$^{\text{PREY}}$ fluorescence at filopodial tips for conditions shown in A-D. Data plotted with median and IQR; individual points are average filopodial tip signal per cell. Statistical significance was assessed by Kruskal-Wallis tests, followed by Dunn's multiple comparisons; P values indicated in plot (Supplemental Table S1 for details). (G) Constructs used for nanoscale pulldown. (H) BAIAP2L2, EPS8, MYO15A constructs used for pulldown experiments. BAIAP2L2 C-terminal domain carries N-terminal GST tag. EPS8 and truncates carry N-terminal 6xHis-2xHA tags. MYO15A(tail) carries N-terminal GFP tag. (I) Representative immunoblots of EPS8 and MYO15A(tail) pulldown by BAIAP2L2 CT. EPS8 and truncates detected by anti-6xHis; MYO15A(tail) detected by anti-GFP. (J) Representative immunoblot of EPS8 and truncate pulldown by BAIAP2L2-CT. Input lanes loaded with 2% (I, anti-6xHis), 0.4% (I, anti-GFP), or 1% (J) of total. 10% (I) or 25% (J) of total pulldown fractions (GST x, BAIAP2L2-CT x) were analyzed. Predicted MW of recombinant proteins (right); MW ladder sizes (left). (K) Previously reported interactions between MYO15A and EPS8 (black), as well as the BAIAP2L2-EPS8 interaction described here (red).

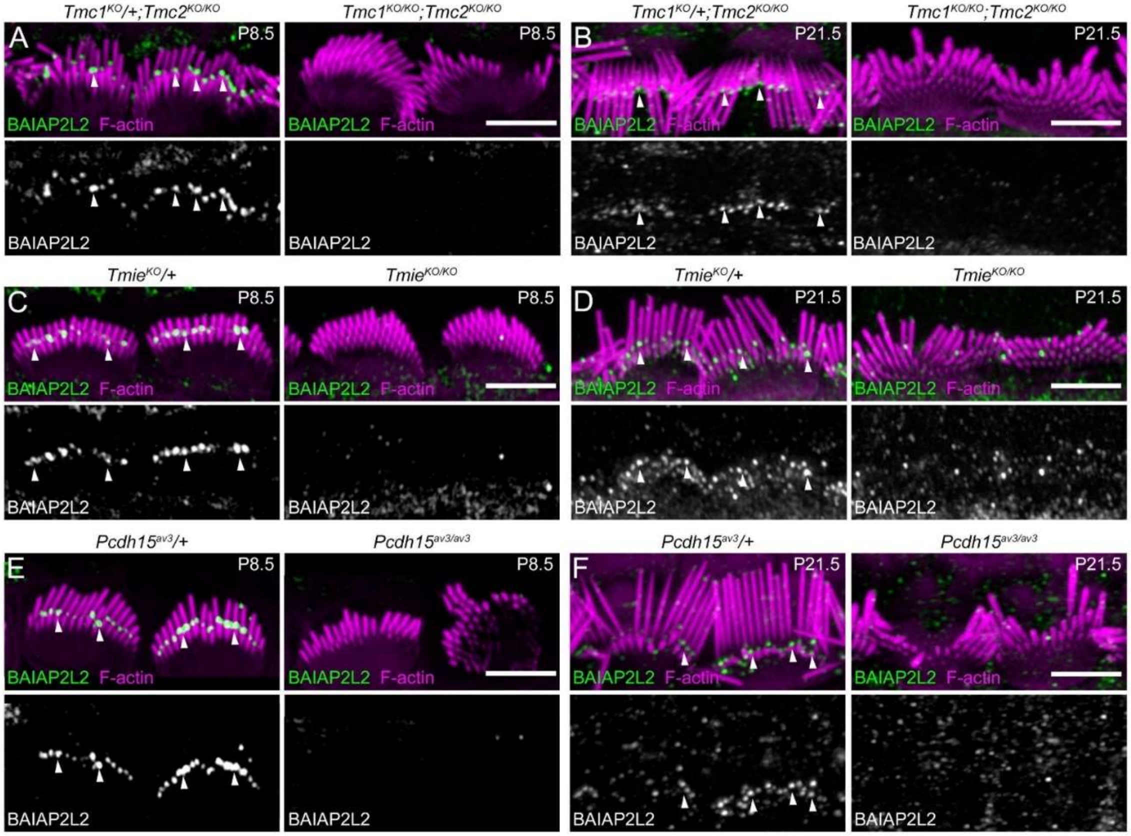

Figure 3-3. BAIAP2L2 is absent from stereocilia tips in transduction mutants.

Anti-BAIAP2L2 signal in transduction mutant heterozygote and knockout IHCs at P8.5 (A, C, E) and P21.5 (B, D, F). In most images, hair bundles were flattened back towards the bare zone. Antibody signal intensity is matched between heterozygote and knockout pairs in each panel, but not comparable across ages or mutants. (A, B) *Tmc1*^{KO}/+; *Tmc2*$^{KO/KO}$ and *Tmc1*$^{KO/KO}$; *Tmc2*$^{KO/KO}$. In P21.5 heterozygote, bundle is folded forward over the shorter stereocilia. (C, D) *Tmie*^{KO}/+ and *Tmie*$^{KO/KO}$. (E, F) *Pcdh15*^{av3}/+ and *Pcdh15*$^{av3/av3}$. Solid arrowheads at row 2 tips. Scale, 5 µm.

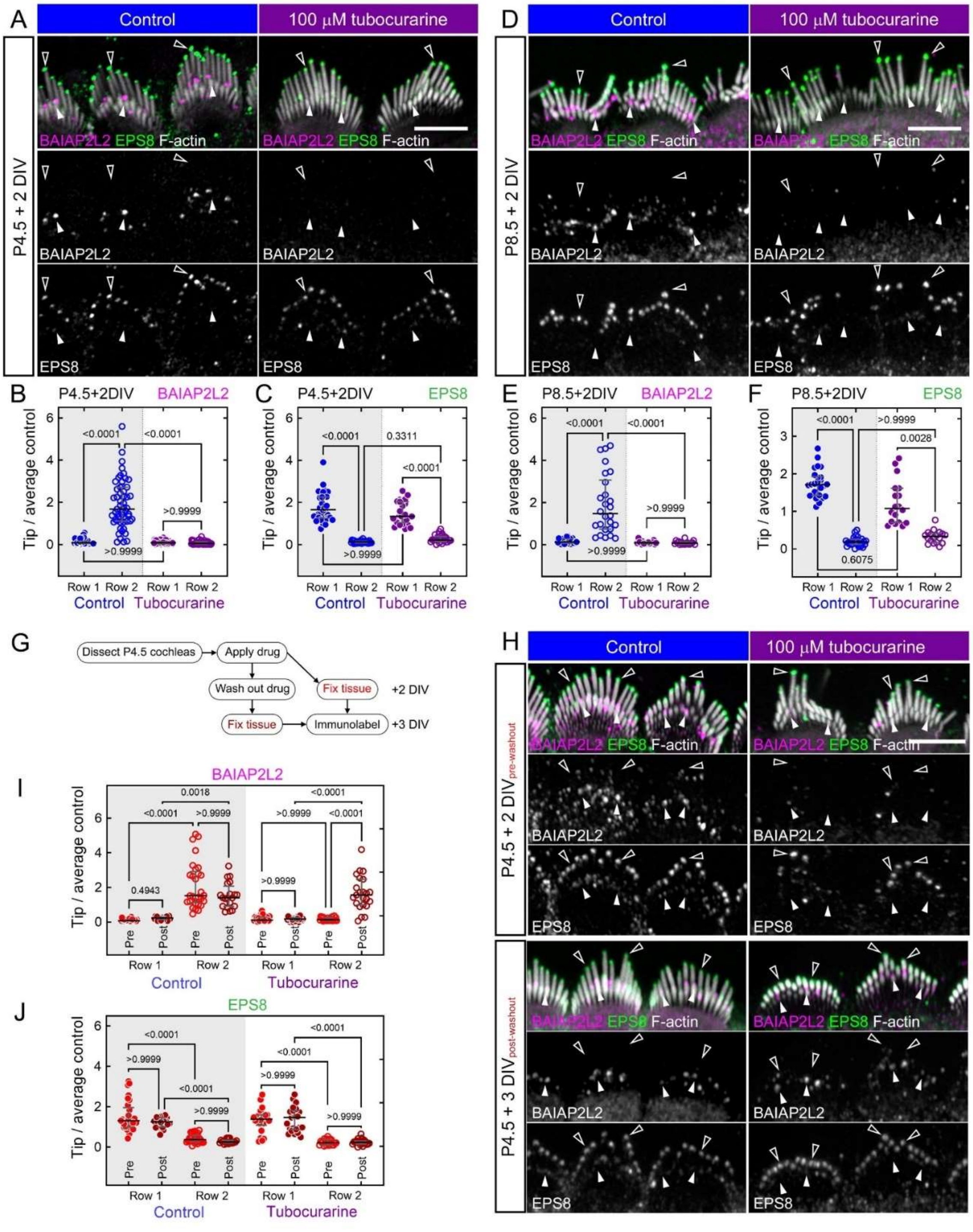

Figure 3-4. BAIAP2L2 tip enrichment is reversibly inhibited by transduction block.

Anti-BAIAP2L2 and anti-EPS8 signal in IHCs of C57BL/6J cochleas cultured for 2 DIV with 100 μM tubocurarine. Cochleas were dissected at either P4.5 (A) or P8.5 (D). (B, C, E, F) Quantitation of BAIAP2L2 (C, E) and EPS8 (D, F) signal from (A, B). Signal was normalized to average control signal of a given experiment. (G) Wash-in/out experiment design. (H) Anti-BAIAP2L2 and anti-EPS8 signal in IHCs of C57BL/6J cochleas dissected at P4.5 and cultured for 2 DIV with 100 μM tubocurarine, followed by wash-out of original media and 1 additional DIV after wash-out. (I, J) Quantitation of BAIAP2L2 (I) and EPS8 (J) signal from (H). Post-washout signal was normalized to control pre-washout signal. Antibody signal intensity was matched between control and tubocurarine pairs for each experiment. Data are plotted with median and IQR; a point represents the average normalized tip signal for a single IHC. Statistical significance was assessed by Kruskal-Wallis tests, followed by Dunn's multiple comparisons; P values indicated in plots (Supplemental Table S1 for details). Empty arrowheads at row 1 tips, solid arrowheads at row 2 tips. Scale, 5 μm.

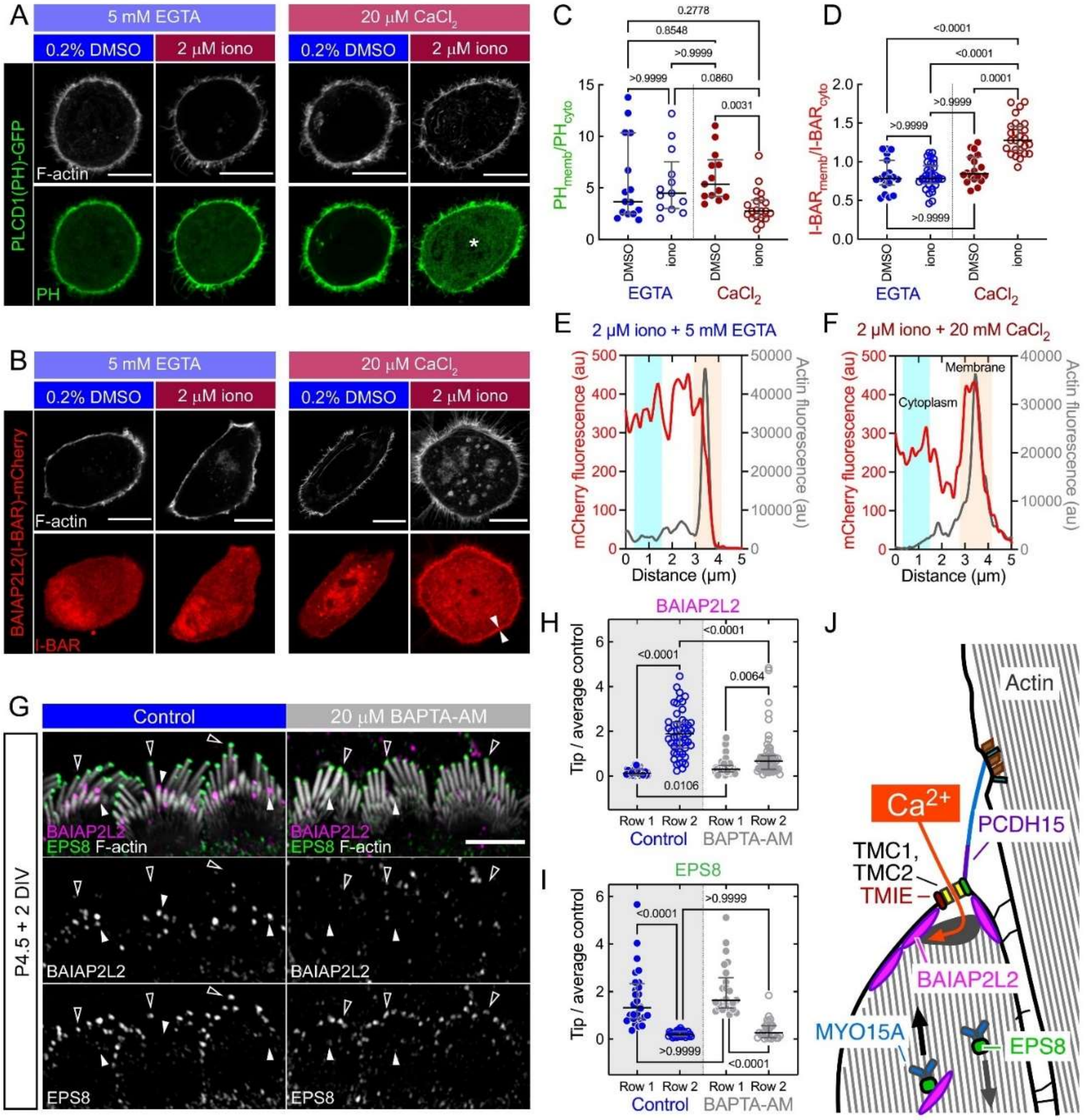

Figure 3-5. Ca^{2+} mediates row 2 tip enrichment of BAIAP2L2.

(A, B) HeLa cells expressing PLCD1(PH) with a C-terminal GFP tag (A) or BAIAP2L2(I-BAR) with a C-terminal mCherry tag (B). Cells treated with 0.2% DMSO or 2 μM ionomycin (iono) supplemented with 5 mM EGTA or 20 μM CaCl$_2$. Fluorescence intensity was adjusted per cell. In iono/Ca^{2+}-treated samples, asterisk indicates elevated PLCD1(PH) in the cytoplasm and arrowheads indicate increased BAIAP2L2(I-BAR) at the membrane. (C, D) Quantitation of membrane enrichment for PLCD1(PH)

(C) or BAIAP2L2(I-BAR) (D) under indicated conditions. (E, F) Example line scans of BAIAP2L2(I-BAR) and F-actin (phalloidin) signal from ionomycin-treated cells with (E) EGTA or (F) $CaCl_2$. (G) Anti-BAIAP2L2 and anti-EPS8 signal in IHCs from P4.5 C57BL/6J cochleas cultured for 2 DIV with 20 μM BAPTA-AM. (H, I) Quantitation of BAIAP2L2 (H) & EPS8 (I) signal (as in Figure 4). (J) Summary schematic depicting BAIAP2L2 transport by MYO15A-EPS8 and Ca^{2+}-aided retention in stereocilia. Data are plotted with median and IQR. Statistical significance was assessed by Kruskal-Wallis tests, followed by Dunn's multiple comparisons; In B and D, a point is the average ratio of membrane/cytoplasm signal per cell. In H and I, a point is the average tip signal for a single IHC. P values indicated in plots (Supplemental Table S1 for details). Scale: A, 10 μm; E, 5 μm.

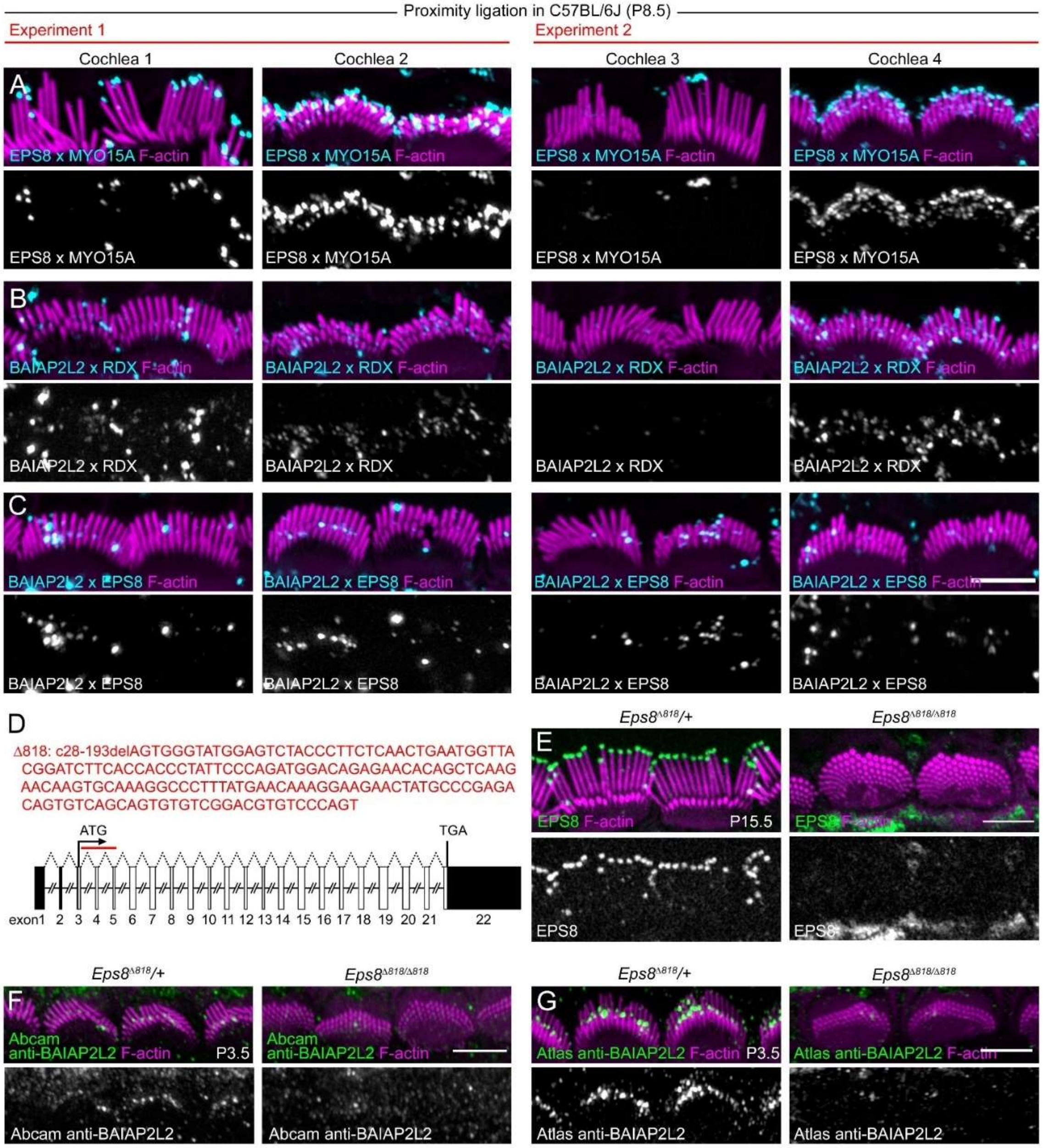

Supplemental Figure 3-1. Variability in proximity ligation assay signal and generation of *Eps8*$^{\Delta 818}$ mutant.

To show the range of signal obtained, four examples from 2 experiments and 4 cochleas were selected for each of the antibody pairs examined by proximity ligation assay (PLA) in Figure 1B-D, including the specific panels shown in Figure 1, B-D. Cochleae from P8.5 C57BL/6J mice were used. (A) Anti-MYO15A and anti-EPS8. (B) Anti-RDX and anti-BAIAP2L2. (C) Anti-BAIAP2L2 and anti-EPS8. Signal intensity is matched for the set of cochleas shown for each experiment. (D) Schematic representation of the mouse *epidermal growth factor receptor kinase substrate 8 (Eps8)* gene (ENSMUSG00000015766; MGI:104684), which consists of 22 exons and spans ~180 kb of genomic DNA on chromosome 6. The translation start (ATG) and stop (TGA) sites are located in exons 3 and 22 respectively. Untranslated regions are shown in black. To generate a null allele, CRISPR/Cas9 was used to target gRNA to exons 3 and 5. (E) Anti-EPS8 signal in P15.5 *Eps8*$^{\Delta 818}$ heterozygote and homozygote IHCs in maximum projections of slices encompassing hair bundles. Antibody used was from BD Transduction Laboratories, catalog #610143, as noted in Methods. Immunoreactivity against EPS8 is lost in the *Eps8*$^{\Delta 818}$ homozygote. (F, G) Anti-BAIAP2L2 signal in P3.5 *Eps8*$^{\Delta 818}$ heterozygote and homozygote IHCs in maximum projections of slices encompassing bundles. The antibodies used were either from Abcam (Cat# ab224323) (F) or Atlas (Sigma-Aldrich Cat# HPA003043) (G). The Abcam antibody was used throughout the present study, while the Atlas antibody was previously tested in *Eps8*-null bundles by Carlton et al. (2020). The Atlas antibody appears to produce brighter stereocilia tip signal in the heterozygote control than in the knockout, whereas the signal intensity of the Abcam antibody is more comparable between heterozygote and knockout. Scale, 5 μm.

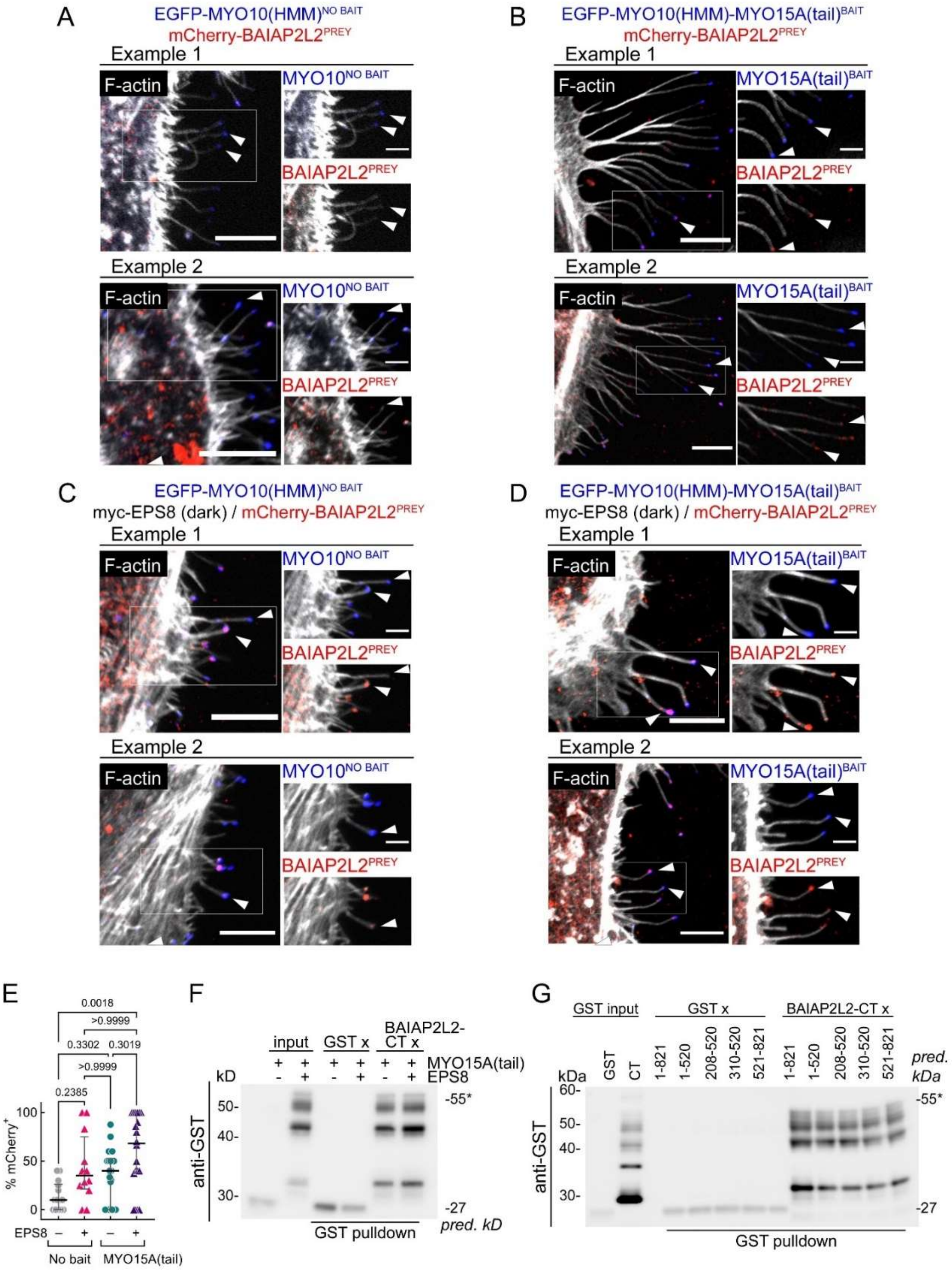

Supplemental Figure 3-2. Interactions of MYO15A, EPS8, and BAIAP2L2.

(A-D) Further examples of nanoscale pulldown in HeLa cells. (A-B) mCherry-BAIAP2L2^{PREY} co-expressed with (A) EGFP-MYO10$^{NO\text{-}BAIT}$ or (B) EGFP-MYO10-MYO15A(tail)^{BAIT}. (C-D) Myc-EPS8 and mCherry-BAIAP2L2$^{\text{PREY}}$ co-expressed with (C) EGFP-MYO10$^{\text{NO-BAIT}}$ or (D) EGFP-MYO10-MYO15A(tail)$^{\text{BAIT}}$. Scale, 5 μm in micrographs on the left side of each panel or 2 μm in insets. (E) Alternate analysis of data shown in Figure 3-2F. Data are median and IQR, with individual points representing the percentage of mCherry-positive filopodia of an analyzed cell. The threshold value for mCherry-positive was defined as the mean normalized intensity signal for mCherry-BAIAP2L2$^{\text{PREY}}$ co-expressed with EGFP-MYO10$^{\text{NO-BAIT}}$. Data were analyzed by Kruskal-Wallis with Dunn's multiple comparisons; P values indicated in plots (Supplemental Table 3-1 for details). (F) Representative immunoblot of immobilized bait proteins used to test the tripartite interaction (Figure 3-2 I). (G). Representative immunoblot of immobilized bait proteins used in mapping the BAIAP2L2-EPS8 interaction (Figure 3-2 J). For input lanes, 2% (F) or 1% (G) of total was analyzed. For pulldown fractions (GST x, BAIAP2L2-CT x), 10% (F) or 25% (G) of total was analyzed. GST and GST-BAIAP2L2-CT detected by anti-GST. Pulldown fractions contain immobilized bait protein. Predicted MW of recombinant proteins indicated on the right (55 kD is the predicted size of the full-length CT construct, marked with *; smaller bands are presumed proteolytic fragments). MW ladder sizes indicated on the left.

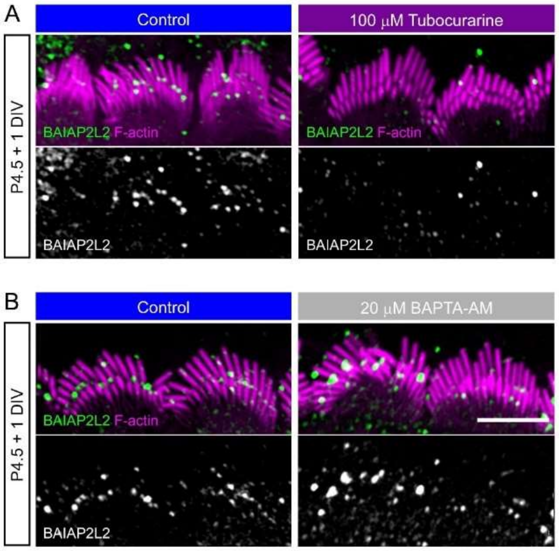

Supplemental Figure 3-3. BAIAP2L2 tip enrichment in explants with tubocurarine and BAPTA-AM at 1 DIV.

(A-B) Anti-BAIAP2L2 in IHCs of C57BL/6J cochleas cultured for 1 DIV with 100 µM tubocurarine (A) or 20 µM BAPTA-AM (B). Cochleas were dissected at P4.5. 1 DIV with tubocurarine was largely sufficient to eliminate BAIAP2L2 tip enrichment, while 1 DIV with BAPTA-AM led to incomplete elimination of BAIAP2L2. Antibody signal intensity was matched between control and drug pairs for each experiment. Scale, 5 µm.

	Group descriptive statistics	**n**	**Q1**	**Median**	**Q3**
Figure 3-1E ***PLA normalized by cell***	EPS8 alone$_{\text{Row 1}}$	19	0.9029	0.9671	1.018
	EPS8 alone$_{\text{Row 2}}$	19	0.9819	1.033	1.097
	MYO15A x EPS8$_{\text{Row 1}}$	51	1.416	1.599	1.706
	MYO15A x EPS8$_{\text{Row 2}}$	51	0.2916	0.3968	0.5842
	BAIAP2L2 x RDX$_{\text{Row 1}}$	61	0.7137	0.8799	1.002
	BAIAP2L2 x RDX$_{\text{Row 2}}$	61	0.9984	1.12	1.286
	BAIAP2L2 x EPS8$_{\text{Row 1}}$	62	0.4272	0.6169	0.8877
	BAIAP2L2 x EPS8$_{\text{Row 2}}$	62	1.112	1.361	1.573
	Dunn's multiple comparisons	**Mean rank diff.**		**P Value**	
	EPS8 alone$_{\text{Row 1}}$ vs. EPS8 alone$_{\text{Row 2}}$	-26.16		>0.9999	
	MYO15A x EPS8$_{\text{Row 1}}$ vs. MYO15A x EPS8$_{\text{Row 2}}$	259.4		<0.0001	
	BAIAP2L2 x RDX$_{\text{Row 1}}$ vs. BAIAP2L2 x RDX$_{\text{Row 2}}$	-86.87		<0.0001	
	BAIAP2L2 x EPS8$_{\text{Row 1}}$ vs. BAIAP2L2 x EPS8$_{\text{Row 2}}$	-180.2		<0.0001	
Figure 3-1F ***PLA normalized to*** ***MYO15A x EPS8***	**Group descriptive statistics**	**n**	**Q1**	**Median**	**Q3**
	EPS8 alone$_{\text{Row 1}}$	19	0.01774	0.06785	0.07316
	EPS8 alone$_{\text{Row 2}}$	19	0.01897	0.07441	0.07984
	MYO15A x EPS8$_{\text{Row 1}}$	51	0.6297	1.304	1.797
	MYO15A x EPS8$_{\text{Row 2}}$	51	0.1942	0.3983	0.6408
	BAIAP2L2 x RDX$_{\text{Row 1}}$	61	0.09291	0.627	1.385
	BAIAP2L2 x RDX$_{\text{Row 2}}$	61	0.1738	1.054	1.855
	BAIAP2L2 x EPS8$_{\text{Row 1}}$	62	0.0577	0.07975	0.1679
	BAIAP2L2 x EPS8$_{\text{Row 2}}$	62	0.08565	0.2416	0.5346
	Dunn's multiple comparisons	**Mean rank diff.**		**P Value**	
	EPS8 alone$_{\text{Row 1}}$ vs. EPS8 alone$_{\text{Row 2}}$	-5.263		>0.9999	
	MYO15A x EPS8$_{\text{Row 1}}$ vs. MYO15A x EPS8$_{\text{Row 2}}$	108.8		<0.0001	
	BAIAP2L2 x RDX$_{\text{Row 1}}$ vs. BAIAP2L2 x RDX$_{\text{Row 2}}$	-27.05		0.7224	
	BAIAP2L2 x EPS8$_{\text{Row 1}}$ vs. BAIAP2L2 x EPS8$_{\text{Row 2}}$	-59.58		0.0118	
Figure 3-2G ***nanoSPDmCherry intensity***	**Group descriptive statistics**	**n**	**Q1**	**Median**	**Q3**
	BAIAP2L2/no bait	14	16.61	18.49	21.12
	BAIAP2L2/MYO15A(tail)	22	17.81	26.18	34.36
	BAIAP2L2+EPS8/no bait	12	20.52	23.72	34.03
	BAIAP2L2+EPS8/MYO15A(tail)	20	23.48	44.12	59.52
	Dunn's multiple comparisons	**Mean rank diff.**		**P Value**	
	BAIAP2L2/no bait vs. BAIAP2L2/MYO15A(tail)	-14.49		0.1924	Ns
	BAIAP2L2/no bait vs. BAIAP2L2+EPS8/no bait	-14.24		0.4025	Ns
	BAIAP2L2/no bait vs. BAIAP2L2+EPS8/MYO15A(tail)	-25.79		0.0011	**
	BAIAP2L2/MYO15A(tail) vs. BAIAP2L2+EPS8/no bait	0.2462		>0.9999	Ns
	BAIAP2L2/MYO15A(tail) vs. BAIAP2L2+EPS8/MYO15A(tail)	-11.3		0.3868	Ns
	BAIAP2L2+EPS8/no bait vs. BAIAP2L2+EPS8/MYO15A(tail)	-11.54		0.6595	Ns

Supplemental Figure 3-1E ***nanoSPD %mCherry+ filopodia***	**Group descriptive statistics**	**n**	**Q1**	**Median**	**Q3**
	BAIAP2L2/no bait	14	0	10	26.25
	BAIAP2L2/MYO15A(tail)	22	0	40	52.5
	BAIAP2L2+EPS8/no bait	12	21.25	35	75
	BAIAP2L2+EPS8/MYO15A(tail)	20	38.13	68.33	100
	Dunn's multiple comparisons	**Mean rank diff.**		**P Value**	
	BAIAP2L2/no bait vs. BAIAP2L2/MYO15A(tail)	-12.81		0.3302	Ns
	BAIAP2L2/no bait vs. BAIAP2L2+EPS8/no bait	-15.8		0.2385	Ns
	BAIAP2L2/no bait vs. BAIAP2L2+EPS8/MYO15A(tail)	-24.63		0.0018	**
	BAIAP2L2/MYO15A(tail) vs. BAIAP2L2+EPS8/no bait	-2.989		>0.9999	Ns
	BAIAP2L2/MYO15A(tail) vs. BAIAP2L2+EPS8/MYO15A(tail)	-11.81		0.3019	Ns
	BAIAP2L2+EPS8/no bait vs. BAIAP2L2+EPS8/MYO15A(tail)	-8.825		>0.9999	Ns
Figure 3-4B ***P4.5+2DIV explants with tubocurarine Normalized BAIAP2L2 intensity***	**Group descriptive statistics**	**n**	**Q1**	**Median**	**Q3**
	Control$_{\text{Row 1}}$	55	0.0501	0.0828	0.1632
	Control$_{\text{Row 2}}$	55	1.1170	1.6820	2.7130
	Tubo$_{\text{Row 1}}$	46	0.0360	0.0795	0.1316
	Tubo$_{\text{Row 2}}$	46	0.0145	0.0461	0.1265
	Dunn's multiple comparisons	**Mean rank diff.**		**P Value**	
	Control$_{\text{Row 1}}$ vs. Control$_{\text{Row 2}}$	-88.58		<0.0001	****
	Control$_{\text{Row 1}}$ vs. Tubo$_{\text{Row 1}}$	6.717		>0.9999	Ns
	Control$_{\text{Row 1}}$ vs. Tubo$_{\text{Row 2}}$	22.35		0.3342	Ns
	Control$_{\text{Row 2}}$ vs. Tubo$_{\text{Row 1}}$	95.3		<0.0001	****
	Control$_{\text{Row 2}}$ vs. Tubo$_{\text{Row 2}}$	110.9		<0.0001	****
	Tubo$_{\text{Row 1}}$ vs. Tubo$_{\text{Row 2}}$	15.63		>0.9999	Ns
Figure 3-4C ***P4.5+2DIV explants with tubocurarine Normalized EPS8 intensity***	**Group descriptive statistics**	**n**	**Q1**	**Median**	**Q3**
	Control$_{\text{Row 1}}$	32	1.2540	1.6610	2.2640
	Control$_{\text{Row 2}}$	32	0.0818	0.1302	0.1627
	Tubo$_{\text{Row 1}}$	27	1.0420	1.3370	2.0360
	Tubo$_{\text{Row 2}}$	27	0.1419	0.2190	0.3793
	Dunn's multiple comparisons	**Mean rank diff.**		**P Value**	
	Control$_{\text{Row 1}}$ vs. Control$_{\text{Row 2}}$	70.5		<0.0001	****
	Control$_{\text{Row 1}}$ vs. Tubo$_{\text{Row 1}}$	7.99		>0.9999	Ns
	Control$_{\text{Row 1}}$ vs. Tubo$_{\text{Row 2}}$	53.36		<0.0001	****
	Control$_{\text{Row 2}}$ vs. Tubo$_{\text{Row 1}}$	-62.51		<0.0001	****
	Control$_{\text{Row 2}}$ vs. Tubo$_{\text{Row 2}}$	-17.14		0.3311	Ns
	Tubo$_{\text{Row 1}}$ vs. Tubo$_{\text{Row 2}}$	45.37		<0.0001	****

Figure 3-4E ***P8.5+2DIV explants with tubocurarine Normalized BAIAP2L2 intensity***	**Group descriptive statistics**	**n**	**Q1**	**Median**	**Q3**
	Control$_{\text{Row 1}}$	26	0.0728	0.1429	0.2852
	Control$_{\text{Row 2}}$	26	0.7454	1.4800	3.0710
	Tubo$_{\text{Row 1}}$	18	0.0608	0.0894	0.1368
	Tubo$_{\text{Row 2}}$	18	0.0298	0.0801	0.1347
	Dunn's multiple comparisons	**Mean rank diff.**		**P Value**	
	Control$_{\text{Row 1}}$ vs. Control$_{\text{Row 2}}$	-36.62		<0.0001	****
	Control$_{\text{Row 1}}$ vs. Tubo$_{\text{Row 1}}$	10.15		>0.9999	Ns
	Control$_{\text{Row 1}}$ vs. Tubo$_{\text{Row 2}}$	13.59		0.496	Ns
	Control$_{\text{Row 2}}$ vs. Tubo$_{\text{Row 1}}$	46.76		<0.0001	****
	Control$_{\text{Row 2}}$ vs. Tubo$_{\text{Row 2}}$	50.21		<0.0001	****
	Tubo$_{\text{Row 1}}$ vs. Tubo$_{\text{Row 2}}$	3.444		>0.9999	Ns
Figure 3-4F ***P8.5+2DIV explants with tubocurarine Normalized EPS8 intensity***	**Group descriptive statistics**	**n**	**Q1**	**Median**	**Q3**
	Control$_{\text{Row 1}}$	26	1.4290	1.7080	1.9260
	Control$_{\text{Row 2}}$	26	0.1209	0.1860	0.2549
	Tubo$_{\text{Row 1}}$	18	0.7017	1.0800	1.6180
	Tubo$_{\text{Row 2}}$	18	0.1685	0.3334	0.4136
	Dunn's multiple comparisons	**Mean rank diff.**		**P Value**	
	Control$_{\text{Row 1}}$ vs. Control$_{\text{Row 2}}$	53.35		<0.0001	****
	Control$_{\text{Row 1}}$ vs. Tubo$_{\text{Row 1}}$	12.84		0.6075	Ns
	Control$_{\text{Row 1}}$ vs. Tubo$_{\text{Row 2}}$	42.67		<0.0001	****
	Control$_{\text{Row 2}}$ vs. Tubo$_{\text{Row 1}}$	-40.51		<0.0001	****
	Control$_{\text{Row 2}}$ vs. Tubo$_{\text{Row 2}}$	-10.68		>0.9999	Ns
	Tubo$_{\text{Row 1}}$ vs. Tubo$_{\text{Row 2}}$	29.83		0.0028	**
Figure 3-4I ***P4.5+3DIV (wash-in/out)*** ***explants with tubocurarine Normalized BAIAP2L2 intensity***	**Group descriptive statistics**	**n**	**Q1**	**Median**	**Q3**
	Control/Pre$_{\text{Row 1}}$	29	0.0668	0.0838	0.1546
	Control/Post$_{\text{Row 1}}$	20	0.1523	0.2334	0.2964
	Tubo/Pre$_{\text{Row 1}}$	22	0.0774	0.1187	0.2865
	Tubo/Post$_{\text{Row 1}}$	23	0.0831	0.1828	0.2527
	Control/Pre$_{\text{Row 2}}$	29	1.1200	1.5230	2.9200
	Control/Post$_{\text{Row 2}}$	20	0.9159	1.4030	2.0800
	Tubo/Pre$_{\text{Row 2}}$	22	0.0802	0.1300	0.2653
	Tubo/Post$_{\text{Row 2}}$	23	0.9997	1.5660	2.4770
	Dunn's multiple comparisons	**Mean rank diff.**		**P Value**	
	Control/Pre$_{\text{Row 1}}$ vs. Control/Post$_{\text{Row 1}}$	-37.53		0.4943	Ns
	Control/Pre$_{\text{Row 1}}$ vs. Tubo/Pre$_{\text{Row 1}}$	-19.42		>0.9999	Ns
	Control/Pre$_{\text{Row 1}}$ vs. Tubo/Post$_{\text{Row 1}}$	-20.99		>0.9999	Ns
	Control/Pre$_{\text{Row 1}}$ vs. Control/Pre$_{\text{Row 2}}$	-114.8		<0.0001	****
	Control/Pre$_{\text{Row 1}}$ vs. Control/Post$_{\text{Row 2}}$	-106.2		<0.0001	****
	Control/Pre$_{\text{Row 1}}$ vs. Tubo/Pre$_{\text{Row 2}}$	-20.38		>0.9999	Ns
	Control/Pre$_{\text{Row 1}}$ vs. Tubo/Post$_{\text{Row 2}}$	-103.4		<0.0001	****

P4.5+3DIV (wash-in/out) explants with Tubocurarine Normalized BAIAP2L2 Intensity (cont.)	Control/Post$_{\text{Row 1}}$ vs. Tubo/Pre$_{\text{Row 1}}$	18.1		>0.9999	Ns
	Dunn's multiple comparisons	**Mean rank diff.**		**P Value**	
	Control/Post$_{\text{Row 1}}$ vs. Tubo/Post$_{\text{Row 1}}$	16.54		>0.9999	Ns
	Control/Post$_{\text{Row 1}}$ vs. Control/Pre$_{\text{Row 2}}$	-77.26		<0.0001	****
	Control/Post$_{\text{Row 1}}$ vs. Control/Post$_{\text{Row 2}}$	-68.7		0.0018	**
	Control/Post$_{\text{Row 1}}$ vs. Tubo/Pre$_{\text{Row 2}}$	17.15		>0.9999	Ns
	Control/Post$_{\text{Row 1}}$ vs. Tubo/Post$_{\text{Row 2}}$	-65.89		0.0021	**
	Tubo/Pre$_{\text{Row 1}}$ vs. Tubo/Post$_{\text{Row 1}}$	-1.563		>0.9999	Ns
	Tubo/Pre$_{\text{Row 1}}$ vs. Control/Pre$_{\text{Row 2}}$	-95.37		<0.0001	****
	Tubo/Pre$_{\text{Row 1}}$ vs. Control/Post$_{\text{Row 2}}$	-86.8		<0.0001	****
	Tubo/Pre$_{\text{Row 1}}$ vs. Tubo/Pre$_{\text{Row 2}}$	-0.9545		>0.9999	Ns
	Tubo/Pre$_{\text{Row 1}}$ vs. Tubo/Post$_{\text{Row 2}}$	-84		<0.0001	****
	Tubo/Post$_{\text{Row 1}}$ vs. Control/Pre$_{\text{Row 2}}$	-93.81		<0.0001	****
	Tubo/Post$_{\text{Row 1}}$ vs. Control/Post$_{\text{Row 2}}$	-85.24		<0.0001	****
	Tubo/Post$_{\text{Row 1}}$ vs. Tubo/Pre$_{\text{Row 2}}$	0.6087		>0.9999	Ns
	Tubo/Post$_{\text{Row 1}}$ vs. Tubo/Post$_{\text{Row 2}}$	-82.43		<0.0001	****
	Control/Pre$_{\text{Row 2}}$ vs. Control/Post$_{\text{Row 2}}$	8.564		>0.9999	Ns
	Control/Pre$_{\text{Row 2}}$ vs. Tubo/Pre$_{\text{Row 2}}$	94.41		<0.0001	****
	Control/Pre$_{\text{Row 2}}$ vs. Tubo/Post$_{\text{Row 2}}$	11.37		>0.9999	Ns
	Control/Post$_{\text{Row 2}}$ vs. Tubo/Pre$_{\text{Row 2}}$	85.85		<0.0001	****
	Control/Post$_{\text{Row 2}}$ vs. Tubo/Post$_{\text{Row 2}}$	2.807		>0.9999	Ns
	Tubo/Pre$_{\text{Row 2}}$ vs. Tubo/Post$_{\text{Row 2}}$	-83.04		<0.0001	****
Figure 3-4J ***P4.5+3DIV (wash-in/out) explants with tubocurarine Normalized EPS8 intensity***	**Group descriptive statistics**	**n**	**Q1**	**Median**	**Q3**
	Control/Pre$_{\text{Row 1}}$	29	0.9835	1.3080	1.9560
	Control/Post$_{\text{Row 1}}$	20	0.9957	1.2580	1.4550
	Tubo/Pre$_{\text{Row 1}}$	22	1.0810	1.3880	1.5970
	Tubo/Post$_{\text{Row 1}}$	23	0.8815	1.4700	1.8090
	Control/Pre$_{\text{Row 2}}$	29	0.2613	0.3729	0.5801
	Control/Post$_{\text{Row 2}}$	20	0.2063	0.2532	0.3396
	Tubo/Pre$_{\text{Row 2}}$	22	0.0994	0.2232	0.3745
	Tubo/Post$_{\text{Row 2}}$	23	0.1471	0.2455	0.2975
	Dunn's multiple comparisons	**Mean rank diff.**		**P Value**	
	Control/Pre$_{\text{Row 1}}$ vs. Control/Post$_{\text{Row 1}}$	7.912		>0.9999	Ns
	Control/Pre$_{\text{Row 1}}$ vs. Tubo/Pre$_{\text{Row 1}}$	4.18		>0.9999	Ns
	Control/Pre$_{\text{Row 1}}$ vs. Tubo/Post$_{\text{Row 1}}$	2.645		>0.9999	Ns
	Control/Pre$_{\text{Row 1}}$ vs. Control/Pre$_{\text{Row 2}}$	75.62		<0.0001	****
	Control/Pre$_{\text{Row 1}}$ vs. Control/Post$_{\text{Row 2}}$	95.91		<0.0001	****
	Control/Pre$_{\text{Row 1}}$ vs. Tubo/Pre$_{\text{Row 2}}$	104.2		<0.0001	****
	Control/Pre$_{\text{Row 1}}$ vs. Tubo/Post$_{\text{Row 2}}$	103.3		<0.0001	****
	Control/Post$_{\text{Row 1}}$ vs. Tubo/Pre$_{\text{Row 1}}$	-3.732		>0.9999	Ns
	Control/Post$_{\text{Row 1}}$ vs. Tubo/Post$_{\text{Row 1}}$	-5.267		>0.9999	Ns
	Control/Post$_{\text{Row 1}}$ vs. Control/Pre$_{\text{Row 2}}$	67.71		0.0005	***
	Control/Post$_{\text{Row 1}}$ vs. Control/Post$_{\text{Row 2}}$	88		<0.0001	****

P4.5+3DIV (wash-in/out) explants with Tubocurarine Normalized EPS8 Intensity (cont.)	Control/Post$_{\text{Row 1}}$ vs. Tubo/Pre$_{\text{Row 2}}$	96.31		<0.0001	****
	Dunn's multiple comparisons	**Mean rank diff.**		**P Value**	
	Control/Post$_{\text{Row 1}}$ vs. Tubo/Post$_{\text{Row 2}}$	95.43		<0.0001	****
	Tubo/Pre$_{\text{Row 1}}$ vs. Tubo/Post$_{\text{Row 1}}$	-1.536		>0.9999	Ns
	Tubo/Pre$_{\text{Row 1}}$ vs. Control/Pre$_{\text{Row 2}}$	71.44		<0.0001	****
	Tubo/Pre$_{\text{Row 1}}$ vs. Control/Post$_{\text{Row 2}}$	91.73		<0.0001	****
	Tubo/Pre$_{\text{Row 1}}$ vs. Tubo/Pre$_{\text{Row 2}}$	100		<0.0001	****
	Tubo/Pre$_{\text{Row 1}}$ vs. Tubo/Post$_{\text{Row 2}}$	99.16		<0.0001	****
	Tubo/Post$_{\text{Row 1}}$ vs. Control/Pre$_{\text{Row 2}}$	72.98		<0.0001	****
	Tubo/Post$_{\text{Row 1}}$ vs. Control/Post$_{\text{Row 2}}$	93.27		<0.0001	****
	Tubo/Post$_{\text{Row 1}}$ vs. Tubo/Pre$_{\text{Row 2}}$	101.6		<0.0001	****
	Tubo/Post$_{\text{Row 1}}$ vs. Tubo/Post$_{\text{Row 2}}$	100.7		<0.0001	****
	Control/Pre$_{\text{Row 2}}$ vs. Control/Post$_{\text{Row 2}}$	20.29		>0.9999	Ns
	Control/Pre$_{\text{Row 2}}$ vs. Tubo/Pre$_{\text{Row 2}}$	28.61		>0.9999	Ns
	Control/Pre$_{\text{Row 2}}$ vs. Tubo/Post$_{\text{Row 2}}$	27.72		>0.9999	Ns
	Control/Post$_{\text{Row 2}}$ vs. Tubo/Pre$_{\text{Row 2}}$	8.314		>0.9999	Ns
	Control/Post$_{\text{Row 2}}$ vs. Tubo/Post$_{\text{Row 2}}$	7.428		>0.9999	Ns
	Tubo/Pre$_{\text{Row 2}}$ vs. Tubo/Post$_{\text{Row 2}}$	-0.8854		>0.9999	Ns
Figure 3-5C ***Plasma membrane enrichment PLCD1(PH)***	**Group descriptive statistics**	**n**	**Q1**	**Median**	**Q3**
	DMSO+EGTA	15	2.4800	3.6730	10.3500
	iono+EGTA	13	3.0120	4.4900	7.5430
	DMSO+CaCl$_2$	13	4.1740	5.3660	7.7200
	iono+CaCl$_2$	20	2.1450	2.7620	3.8210
	Dunn's multiple comparisons	**Mean rank diff.**		**P Value**	
	DMSO+EGTA vs. iono+EGTA	-3.405		>0.9999	Ns
	DMSO+EGTA vs. DMSO+CaCl$_2$	-9.867		0.8548	Ns
	DMSO+EGTA vs. iono+CaCl$_2$	12.08		0.2778	Ns
	iono+EGTA vs. DMSO+CaCl$_2$	-6.462		>0.9999	Ns
	iono+EGTA vs. iono+CaCl$_2$	15.49		0.086	Ns
	DMSO+CaCl$_2$ vs. iono+CaCl$_2$	21.95		0.0031	**
Figure 3-5D ***Plasma membrane enrichment BAIAP2L2(I-BAR)***	**Group descriptive statistics**	**n**	**Q1**	**Median**	**Q3**
	DMSO+EGTA	19	0.7000	0.7801	1.0180
	iono+EGTA	33	0.7189	0.7822	0.9488
	DMSO+CaCl$_2$	18	0.7699	0.8423	1.0610
	iono+CaCl$_2$	27	1.1470	1.2760	1.4550
	Dunn's multiple comparisons	**Mean rank diff.**		**P Value**	
	DMSO+EGTA vs. iono+EGTA	0.3844		>0.9999	Ns
	DMSO+EGTA vs. DMSO+CaCl$_2$	-10.35		>0.9999	Ns
	DMSO+EGTA vs. iono+CaCl$_2$	-46.51		<0.0001	****
	iono+EGTA vs. DMSO+CaCl$_2$	-10.73		>0.9999	Ns
	iono+EGTA vs. iono+CaCl$_2$	-46.9		<0.0001	****
	DMSO+CaCl$_2$ vs. iono+CaCl$_2$	-36.17		0.0001	***

Figure 3-5H ***P4.5+2DIV explants with BAPTA-AM Normalized BAIAP2L2 intensity***	**Group descriptive statistics**	**n**	**Q1**	**Median**	**Q3**
	Control$_{\text{Row 1}}$	51	0.0470	0.1303	0.2963
	Control$_{\text{Row 2}}$	51	1.2580	1.8840	2.3930
	BAPTA-AM$_{\text{Row 1}}$	56	0.1921	0.3022	0.4755
	BAPTA-AM$_{\text{Row 2}}$	56	0.2988	0.6714	0.9151
	Dunn's multiple comparisons	**Mean rank diff.**		**P Value**	
	Control$_{\text{Row 1}}$ vs. Control$_{\text{Row 2}}$	-129.1		<0.0001	****
	Control$_{\text{Row 1}}$ vs. BAPTA-AM$_{\text{Row 1}}$	-37.47		0.0106	*
	Control$_{\text{Row 1}}$ vs. BAPTA-AM$_{\text{Row 2}}$	-75.74		<0.0001	****
	Control$_{\text{Row 2}}$ vs. BAPTA-AM$_{\text{Row 1}}$	91.59		<0.0001	****
	Control$_{\text{Row 2}}$ vs. BAPTA-AM$_{\text{Row 2}}$	53.32		<0.0001	****
	BAPTA-AM$_{\text{Row 1}}$ vs. BAPTA-AM$_{\text{Row 2}}$	-38.27		0.0064	**
Figure 3-5I ***P4.5+2DIV explants with BAPTA-AM Normalized EPS8 intensity***	**Group descriptive statistics**	**n**	**Q1**	**Median**	**Q3**
	Control$_{\text{Row 1}}$	28	0.8746	1.3230	2.3330
	Control$_{\text{Row 2}}$	28	0.1147	0.1883	0.3193
	BAPTA-AM$_{\text{Row 1}}$	25	1.3120	1.6390	2.5920
	BAPTA-AM$_{\text{Row 2}}$	25	0.0573	0.2679	0.5660
	Dunn's multiple comparisons	**Mean rank diff.**		**P Value**	
	Control$_{\text{Row 1}}$ vs. Control$_{\text{Row 2}}$	48.96		<0.0001	****
	Control$_{\text{Row 1}}$ vs. BAPTA-AM$_{\text{Row 1}}$	-9.501		>0.9999	Ns
	Control$_{\text{Row 1}}$ vs. BAPTA-AM$_{\text{Row 2}}$	42.34		<0.0001	****
	Control$_{\text{Row 2}}$ vs. BAPTA-AM$_{\text{Row 1}}$	-58.47		<0.0001	****
	Control$_{\text{Row 2}}$ vs. BAPTA-AM$_{\text{Row 2}}$	-6.626		>0.9999	ns
	BAPTA-AM$_{\text{Row 1}}$ vs. BAPTA-AM$_{\text{Row 2}}$	51.84		<0.0001	****

Supplemental Table 3-1. Descriptive statistics and results for individual comparisons by Kruskal-Wallis test.

Chapter 4 – Conclusions and future directions

General summary

This dissertation describes work done to determine the significance of BAIAP2L2 in auditory hair bundles, from the functional to potentially more generalizable mechanisms. Chapter 2 focuses on the functional aspects, describing the phenotype of *Baiap2l2* mouse knockouts by assessing their auditory behavior and bundle morphology. These analyses demonstrate that BAIAP2L2 is an essential molecule for the maintenance of hearing. We also present some preliminary insights into the potential interactome of BAIAP2L2 in Chapter 2. Chapter 3 examines BAIAP2L2 targeting within the bundle, tying BAIAP2L2 to the MYO15A-EPS8 complex that is typically associated with row 1 stereocilia tips. Crucially, the work presented in Chapter 3 also identifies Ca^{2+} as a component of the transduction current responsible for modulation of the protein environment at stereocilia tips. The finding that Ca^{2+} enhances the attraction of BAIAP2L2's I-BAR domain to plasma membrane both potentially informs how BAIAP2L2 localization in the bundle is regulated by transduction and well may be applicable to the function and regulation of BAIAP2L2 and other I-BAR domain-containing proteins in other cellular contexts.

Chapter 2 conclusions and future directions

We report *Baiap2l2* as a novel deafness gene in the mouse. *Baiap2l2* deficiency causes progressive hearing loss and the progressive deterioration of bundle as the transducing stereocilia are resorbed after initially developing largely normally. We thus concluded that BAIAP2L2's primary role is in stabilizing the structure of the bundle over its lifetime. As each stereocilium of the bundle is composed of bundled actin filaments that are molded by the constant activity of other proteins, it is logical that BAIAP2L2 may exert its stabilizing influence on the transducing stereocilia by regulating some subset of those other actin effector molecules. Identifying the actin effectors downstream (or upstream) of BAIAP2L2 and their specific activities in stereocilia will be vital for fully understanding how BAIAP2L2 maintains bundle stability.

In view of that aim, we identified several potential members of BAIAP2L2's hair bundle interactome in Chapter 2. *In vitro,* the C-terminal domain of BAIAP2L2 can bind the actin-associated proteins EPS8, ESPNL, CDC42 and RAC1 in interactions mediated through BAIAP2L2's SH3 domain. A complementary panel of interacting proteins, including CIB2, CAPZB, TWF2 and EPS8L2 in addition to EPS8 has also been identified (Yan *et al.*, 2022). EPS8L2 had been included in our panel of potential binding partners but failed to bind under our assay conditions, suggesting that a BAIAP2L2-EPS8L2 interaction may not be of very high affinity, although that does not preclude it from being an important interaction. The identified BAIAP2L2-binding proteins are all expressed in hair cells and have demonstrated roles in bundles (Grimsley-Myers *et al.*, 2009; Peng *et al.*, 2009; Zampini *et al.*, 2011; Riazuddin *et al.*, 2012; Furness *et al.*, 2013; Ueyama *et al.*, 2014; Kirjavainen *et al.*, 2015; Ebrahim *et al.*, 2016a; Avenarius *et al.*, 2017). Understanding if BAIAP2L2 interacts with any of these proteins in the bundle—not only in the artificial context of the *in vitro* binding assays presented in Chapter 2—is essential to understanding how BAIAP2L2 activity contributes to the maintenance of bundle structure and function. As such, future directions should include further examination of the identified interactions. While the BAIAP2L2-EPS8 interaction has been thoroughly investigated in Chapter 3, BAIAP2L2 interactions with the remaining identified partners have yet to be fully characterized.

The simplest approach to evaluating whether any of the identified interactions for BAIAP2L2 are biologically relevant is to assess whether the partners' localization changes in the absence of

BAIAP2L2 or vice versa. This preliminary step has been taken and published for several of the candidates. We report in Chapter 2 that the localization of EPS8 and EPSNL is unchanged in *Baiap2l2*-deficient bundles. Others report that the localization of CIB2 is unchanged in *Baiap2l2*-deficient bundles while CAPZB signal is abolished (Yan *et al.*, 2022). For the converse experiments, where BAIAP2L2 localization has been evaluated in the absence of candidate partners, BAIAP2L2 loses row specificity and labels all stereocilia in *Eps8*-null bundles (Chapter 3), concentrates normally at the tips of transducing stereocilia in *Espnl*-null bundles (Chapter 2), and is lost from all stereocilia in *Cib2*-null bundles (Yan *et al.*, 2022). While it can be argued that an interaction with CIB2 tethers BAIAP2L2 to stereocilia tips, in the context of other data presented in Chapter 3 demonstrating that BAIAP2L2 fails to localize in the absence of several other components of the transduction apparatus, our interpretation is that BAIAP2L2 absence from *Cib2*-null bundles is likely better explained by the lack of a functional transduction channel and the resultant absence of ion influx.

While not yet published, we have also tested for changes in the distribution of the remaining candidates—EPS8L2, TWF2, RAC1 and CDC42—in *Baiap2l2* mutants (Fig. 4-1 – 4-3). EPS8L2 and CAPZB localization were assessed by immunostaining in *Baiap2l2*-null bundles at P14.5 (Fig. 4-1). CAPZB labeling was not completely abolished in the absence of BAIAP2L2 but was instead still found at row 2 stereocilia in both *Baiap2l2* knockout (Fig. 4-1 E, F) and heterozygote control (Fig. 4-1 A, B) bundles, albeit at greatly reduced levels in knockout bundles. Similarly, EPS8L2 was also only retained at residual levels at row 2 tips in *Baiap2l2*-null bundles (Fig. 4-1 G, H), whereas EPS8L2 in heterozygote controls localized intensely along the shafts of all stereocilia with perhaps some concentration at row 2 (Fig. 4-1 C, D). Overall, staining intensity for both CAPZB and EPS8L2 was greatly diminished in the *Baiap2l2*-null bundles (Fig. 4-1 E-H) relative to heterozygote controls (Fig. 4-1 A-D). We have not yet examined BAIAP2L2 in *Eps8l2*- or *Capzb*-null bundles; changes in BAIAP2L2 signal in either mutant would provide further evidence that these proteins function together in bundles, or if BAIAP2L2 is unchanged, suggest that EPS8L2 or CAPZB may function as downstream effectors of BAIAP2L2.

TWF2 localization was also assessed in P7.5 *Baiap2l2*-null hair bundles using immunostaining (Fig. 4-2 A-D). TWF2 signal concentrated towards the ankle link regions, highlighting the space between rows 1 and 2 in IHCs (Fig. 4-2 C, D) and the spaces between rows 1 and 2 and between rows 2 and 3 in OHCs (Fig. 4-2 A, B) for both heterozygote control bundles and *Baiap2l2*-null bundles. BAIAP2L2 localization was also examined in P7.5 *Twf2*-null bundles (Fig. 4-2 E-H). BAIAP2L2 labeled row 2 tips in IHCs of both heterozygote control bundles and *Twf2*-null bundles (Fig. 4-2 G, H), but was sparse in OHCs of either genotype (Fig. 4-2 E, F). Overall, it appears that BAIAP2L2 and TWF2 localize independently of each other in hair bundles. However, TWF2 localization enriches more at row 2 tips later in development (Peng *et al.*, 2009; Avenarius *et al.*, 2017); it is possible that examination of TWF2 in *Baiap2l2*-null bundles or vice versa at ages greater than P7.5 could still reveal differences.

To evaluate the localization of Rho GTPases, we turned to AAV1-mediated expression of GFP-tagged constructs. GFP-CDC42 localization in hair cells was evaluated in cochleas at approximately 2 weeks postnatal, P15.5 for wild-type tissue (Fig. 4-3 A, B) and P14.5 for *Baiap2l2*-null tissue (Fig. 4-3 C, D). Distribution of GFP-CDC42 appeared largely the same in both genotypes. GFP-CDC42 signal appeared predominantly within the cell body, with some labelling of stereocilia shafts (see x-z reslices). GFP signal concentrated at the apical cell junctions for IHCs; this pericuticular signal appeared somewhat punctate in *Baiap2l2*-null IHCs. These observations are consistent with a previous report that also demonstrates elevated levels of CDC42 in stereocilia and at the apical cell junctions of hair cells; CDC42 signal in this report appears smooth along the cell junctions (Ueyama *et al.*, 2014). The

GFP-CD42 puncta may be a consequence of *Baiap2l2* deficiency. Interestingly, the initial report of BAIAP2L2 localization (Pykalainen *et al.*, 2011) placed BAIAP2L2 at regions of cell-cell contact in cultures of Caco-2 cells, a human epithelial cell line derived from a colon carcinoma frequently used as a model of the intestinal brush border. Pykalainen et al. also note that BAIAP2L2 co-localizes in punctate structures with another small GTPase, RAB13, that is associated with junctional complexes (Sakane *et al.*, 2012). However, the cellular organization in the organ of Corti of *Baiap2l2*-deficient mice is grossly normal, unlike what might be expected in mutants where junctional complexes are disrupted (Ueyama *et al.*, 2014; Morozko *et al.*, 2015; Avenarius *et al.*, 2017). BAIAP2L2 labelling is also not readily apparent at apical junctions of hair cells, although the high background outside of the bundle for the BAIAP2L2 antibody used throughout the presented work makes such a claim difficult to verify.

We also attempted to assess the coincidence of BAIAP2L2 and the two identified Rho GTPase binding partners in the bundle by combining AAV1-mediated expression of GFP-tagged RAC1 or CDC42 with immunostaining of BAIAP2L2 (Fig. 4-4). These preliminary analyses at P4.5 and P10.5 show that both RAC1 and CDC42 appear to localize diffusely throughout the cell body and can coat the shafts of the stereocilia (see P10.5 IHC in Fig. 4-4 D, reslices in Fig. 4-3). RAC1 potentially displays a higher preference towards localization in the stereocilia than does CDC42, but variable expression levels of the tagged proteins from cell to cell or animal to animal and the small number of samples limits the interpretability of these data. Immunostaining for BAIAP2L2 in transfected cochleas was similarly inconclusive. In RAC1-transfected cochleas, BAIAP2L2 signal appeared unaffected by RAC1-overexpression (Fig. 4-2 A-D), while in CDC42-transfected cochleas, BAIAP2L2 signal may be attenuated in GFP-positive cells (Fig. 4-2 E, F) at P4.5. If these observations were to bear out, it would suggest that the over-expressed CDC42 might inhibit BAIAP2L2 localization in the bundle. CDC42 and other Rho GTPases are known to associate with plasma membrane; it is conceivable that severely over-expressed CDC42 may out-compete BAIAP2L2 for available membrane binding sites.

Of the proteins identified as candidate binding partners for BAIAP2L2, EPS8L2 and CAPZB appear to be the most strongly affected by the absence of BAIAP2L2, with greatly reduced signal intensity in *Baiap2l2* mutants relative to heterozygote controls, suggesting that BAIAP2L2, EPS8L2, and CAPZB may work together in some form to stabilize the transducing stereocilia. The shared concentration of these molecules at the tips of row 2 stereocilia also makes it plausible that they share enough proximity in stereocilia to form a complex or complexes together. CAPZB activity is clearly associated with stereocilia elongation and widening (Avenarius *et al.*, 2017). The loss of EPS8L2 produces stereocilia that are thinner, and like the loss of BAIAP2L2, eventually leads to the deterioration of the shorter rows of stereocilia (Furness *et al.*, 2013). While CAPZB interacts with TWF2 (Vartiainen *et al.*, 2003), and TWF2 apparently can interact with BAIAP2L2, TWF2 localizes separately from BAIAP2L2. If TWF2 contributes to the activity of a complex with BAIAP2L2 and CAPZB, it is localized to stereocilia tips separately and then added onto such a complex. Altogether, the joint activity of BAIAP2L2-CAPZB-EPS8L2 and potentially TWF2 and the assembly of such a complex merits further thought and investigation.

The conclusions drawn in Chapter 2 and elaborated on above hinge on the assumption that the observable functional and morphological phenotype of the *Baiap2l2*-nulls is attributable to the absence of BAIAP2L2 protein. However, our studies have a potential confounding effect from the C57BL/6 background of both the *Baiap2l2*^{tm1b} line used by our collaborators and the *Baiap2l2*$^{\Delta 16}$ line created and used by our lab. The C57BL/6 strain experiences high frequency hearing loss with an onset around 3-6 months of age (Erway *et al.*, 1996). The genetic factor responsible for this phenotype was initially mapped to a locus (*ahl* for age-related hearing loss) on Chromosome 10 (Johnson *et al.*, 1997), and then mapped to a mutation in *Cdh23*, the gene encoding the upper portion of the tip link (Erway *et al.*, 1996; Noben-Trauth *et al.*, 2003). It is possible that the effects of the *Cdh23* mutation present in the C57BL/6 background could compound and worsen the effects of a potential *Baiap2l2*-null phenotype, thus complicating the interpretation of any observed auditory phenotype for the *Baiap2l2*-null. However, the C57BL/6 background still has some advantages, such as a fully-sequenced genome and ubiquity in the production of numerous knockout strains. Further, the lab's morphological studies are largely confined to the first three weeks post-natal, the period during which bundles develop, well before the onset of hearing loss associated with the *Cdh23* mutation in C57BL/6. While we cannot exclude the possibility that *Cdh23* mutation may impact the observed phenotype in our *Baiap2l2* mutant line, the phenotype of another independent *Baiap2l2* mutant line (Yan *et al.*, 2022) created on an ICR background largely agrees with what we observed, namely elevated ABR thresholds shortly after the onset of hearing and the deterioration of row 3 stereocilia. While the ICR genetic background is not as fully mapped as that of C57BL/6, this line is not associated with congenital hearing loss, and presumably does not share the *Cdh23* mutation responsible for age-related hearing loss in C57BL/6.

Expanded Chapter 3 conclusions and future directions

Chapter 3 examines the trafficking of BAIAP2L2 within the hair bundle. The primary conclusions are that BAIAP2L2 is most likely trafficked non-selectively to all stereocilia tips by a complex of MYO15A-EPS8, but that Ca^{2+} influx through open transduction channels is necessary to retain BAIAP2L2, driving its enrichment at the tips of rows 2 and row 3, the transducing stereocilia. The results in Chapter 3 suggest a means by which ion influx through transduction channels may actively modulate the protein environment within stereocilia, but also raise interesting questions about how proteins circulate within the bundle and the hair cell.

The work in Chapter 3 demonstrates that BAIAP2L2's I-BAR domain is attracted to plasma membrane in the presence of Ca^{2+} but falls short of determining how that attraction is mediated. We do however offer the hypothesis that BAIAP2L2's I-BAR domain may preferentially bind to Ca^{2+}-induced clusters of $PI(4,5)P_2$. To test this hypothesis, future work may include screening for I-BAR binding to vesicles of different lipid composition under either no or elevated Ca^{2+} conditions. Alternatively, the Val169Ala mutation in BAIAP2L2's I-BAR domain identified by Mutai *et al.*, 2022 presents an interesting opportunity to test the effect of a deafness mutation on protein function. A first step would be to ascertain whether this mutation disrupts the capacity of the I-BAR to bind membranes. Membrane association of the mutant I-BAR could be assessed by examining its localization in the same cell assay used in Chapter 3, where cells are subjected to no or elevated Ca^{2+}; this assay would also reveal if Val169Ala perturbs the Ca^{2+} requirement for BAIAP2L2 membrane binding. Some possible results are thus: (1) the mutant I-BAR displays the same behavior as the wildtype I-BAR, and only associates with plasma membrane under elevated Ca^{2+}, (2) the mutant I-BAR fails to associate with membrane under either no or elevated Ca^{2+}, or (3) the mutant I-BAR associates with membrane regardless of Ca^{2+}. As Val169Ala is reported to produce a dominant phenotype of hearing loss, no changes in activity would be somewhat surprising. Of the other two possibilities presented, a loss of membrane binding capacity seems more likely, as the affected residue is likely buried and changes to buried residues frequently prove destabilizing to domain structures.

Reduction of BAIAP2L2 immunoreactivity following transduction block or chelation of intracellular Ca^{2+} with BAPTA-AM appeared to occur relatively slowly, where BAPTA-AM required greater than 24h of treatment to attenuate BAIAP2L2 signal and transduction block abolished BAIAP2L2 signal after 24h. Admittedly, shorter time periods than 24h were not tested, so it is possible that BAIAP2L2 attenuation could occur more rapidly after transduction block with tubocurarine. However, BAIAP2L2 immunoreactivity was attenuated on a rapid time scale by treating isolated cochleas with phenylarsine oxide (PAO), an inhibitor of $PI(4,5)P_2$ synthesis (Hirono *et al.*, 2004; Effertz *et al.*, 2017), for periods as short as 1 hour (Fig. 4-5). The difference in timescale for these observations can potentially be reconciled by hypothesizing that the interventions affecting Ca^{2+} levels at stereocilia tips may not immediately affect pre-existing and presumably stable interactions between BAIAP2L2 and plasma membrane. In contrast, treatment with PAO, by reducing levels of $PI(4,5)P_2$ present in the plasma membrane, may remove necessary substrate for a BAIAP2L2-membrane interaction to occur, as BAIAP2L2 and other I-BAR proteins have been shown to bind phosphoinositide-containing membranes with some preference (Mattila *et al.*, 2007; Pykalainen *et al.*, 2011). $PI(4,5)P_2$ is a necessary co-factor for active transduction channels (Hirono *et al.*, 2004; Effertz *et al.*, 2017; Cunningham *et al.*, 2020), and $PI(4,5)P_2$ depletion by PAO or treatment with other inhibitors of $PI(4,5)P_2$ reduces the amplitude of the transduction current, and presumably decreases the available Ca^{2+} at stereocilia tips. Thus, PAO treatment may undermine BAIAP2L2 membrane association on two fronts, first by reducing the available binding sites by decreasing the prevalence of $PI(4,5)P_2$ in the membrane, and then by weakening the association of BAIAP2L2's I-BAR domain with the membrane by inhibition of the transduction current and subsequent depletion of the Ca^{2+} ions that facilitate I-BAR/membrane binding.

The relative speed at which BAIAP2L2 can apparently be removed from its niche at stereocilia tips may suggest that once BAIAP2L2 is no longer bound, it could be actively transported away from the tips and out of the stereocilia. Our model, where MYO15A-EPS8 complexes constantly sample the environments at individual stereocilia tips before either unloading cargo like BAIAP2L2 or ultimately binding at row 1 tips, offers a facile explanation where BAIAP2L2 released from row 2 or 3 tips in the absence of Ca^{2+} or $PI(4,5)P_2$ can rebind to MYO15A-EPS8 for subsequent trips to perhaps sample other stereocilia. However, MYO15A is a plus end-directed myosin, and as such, its active movement along the actin filaments of a stereocilium's core can only move in the direction of the stereocilium's tip. If BAIAP2L2's exit from the stereocilium is indeed mediated by MYO15A-EPS8, then two main possibilities present themselves. In the first possibility, BAIAP2L2's carrier complex diffuses back down the shaft of stereocilia in the absence of retaining factors. In this situation, a carrier complex would be rather superfluous. Alternately, BAIAP2L2 and/or its carrier complex are trafficked back down through stereocilia by a minus end-directed myosin, such as MYO6. While MYO6 is an important molecule for hair bundle maintenance, such a role for MYO6 is purely conjecture. While the specific detail of how BAIAP2L2 is removed from stereocilia following transduction block is perhaps artificially interesting, MYO15A-EPS8 that localizes to the tips of immature row 2 or 3 stereocilia does presumably need to be re-localized as the bundle develops, and so requires a means to exit stereocilia.

The finding that BAIAP2L2 is likely targeted to stereocilia tips as a cargo of EPS8 is bolstered by the observation that a truncated BAIAP2L2 protein including solely its SH3 domain can localize to bundles (Fig. 4-6 A), while a truncate consisting of only the BAIAP2L2 I-BAR domain appears to be excluded from bundles (Fig. 4-6 B). As shown in Chapter 2, the interactions we identified for BAIAP2L2 are mediated through its SH3 domain. If the I-BAR domain alone cannot target within stereocilia while its isolated SH3 domain can, it follows that the entire BAIAP2L2 protein that localizes to stereocilia tips is likely a cargo of some other protein, and that it may bind this other protein through its SH3 domain. Chapter 3 argues that this other protein is in most cases EPS8 for the purposes of BAIAP2L2 targeting in bundles. However, we also show that BAIAP2L2 can target in the absence of EPS8: *Eps8*-null bundles have BAIAP2L2 labelling at all stereocilia tips, and in nanoSPD experiments, some level of BAIAP2L2 targets to filopodia tips when co-expressed with MYO15A but not EPS8. If BAIAP2L2 is incapable of transporting to the tips of actin-based protrusions independently, then in these cases, BAIAP2L2 transports as part of an alternate complex. The binding activity of BAIAP2L2's SH3 domain is not selective to EPS8, and so allows for the formation of other complexes, suggesting an interesting degree of flexibility in how various bundle proteins may associate with each other.

Concluding remarks

While the specific activity of BAIAP2L2 in hair bundles remains to be defined, this dissertation has demonstrated that BAIAP2L2 is necessary for the maintenance of the bundle's lifetime integrity, and thus necessary for the sense of hearing. This dissertation then has contributed a new molecule to the solution of how a hair cell assembles its bundle. The forays made into the potential interactome of BAIAP2L2 provides insight into how future experiments might attempt to define the specific role of BAIAP2L2 in stabilizing the bundle. Further, the work outlined here provides evidence for direct influence of Ca^{2+} on BAIAP2L2's membrane-binding properties. Ion influx through open transduction channels has been previously observed to drive changes in protein activity and localization in the bundle, but no mechanistic explanation has yet been given. The discoveries in this dissertation describe how ion influx through transduction channels can act directly on an aspect of a bundle protein's biochemical properties, thereby providing a novel and mechanistic explanation as to how Ca^{2+} entering through active transduction channels regulates protein localization in stereocilia.

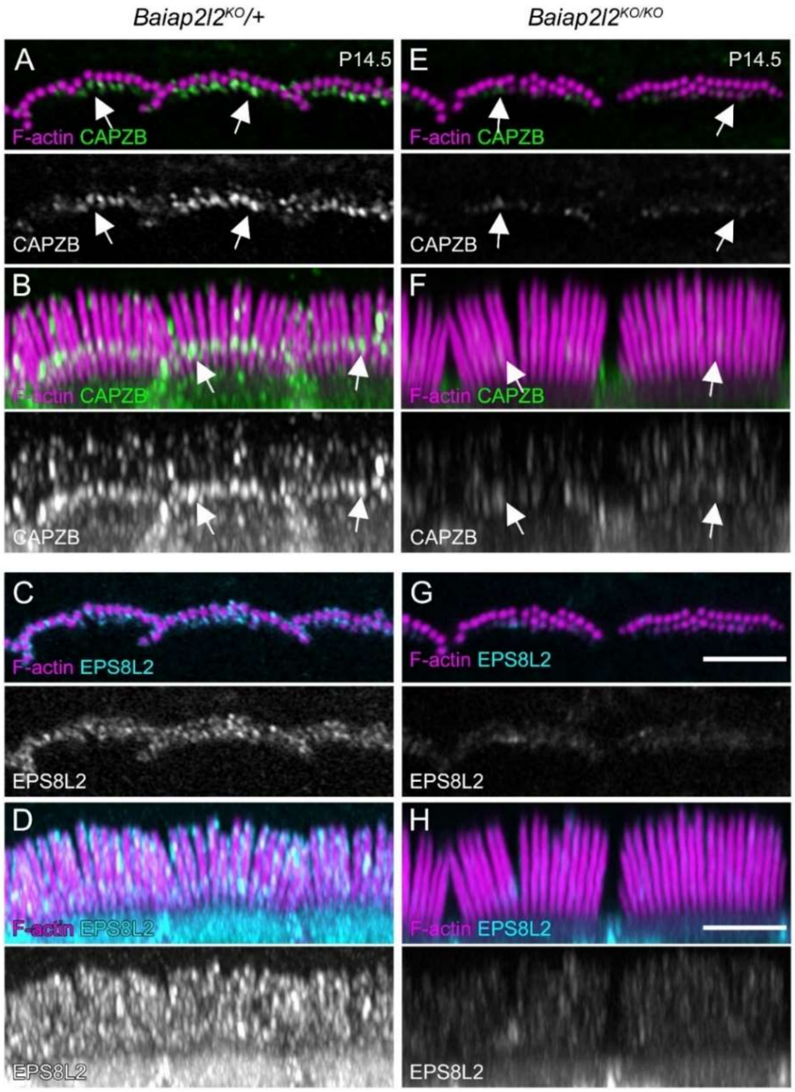

Figure 4-1. CAPZB and EPS8L2 signal is dramatically attenuated in *Baiap2l2*-null bundles. Cochleas from *Baiap2l2*^{KO}/+ (A-D) or *Baiap2l2*$^{KO/KO}$ (E-H) were isolated and co-stained for CAPZB (A, B, E, F) and EPS8L2 (C, D, G, H). CAPZB and EPS8L2 staining of the same bundles are shown separately for clarity (the bundles in A & B are the same as those in C & D). Images in A, E, C, G are single slices at approximately the tips of row 2 stereocilia. Images in B, D, F, H are en face maximum projections of the same bundles shown for each genotype. Scale, 5 μm. Immunostaining experiments performed twice.

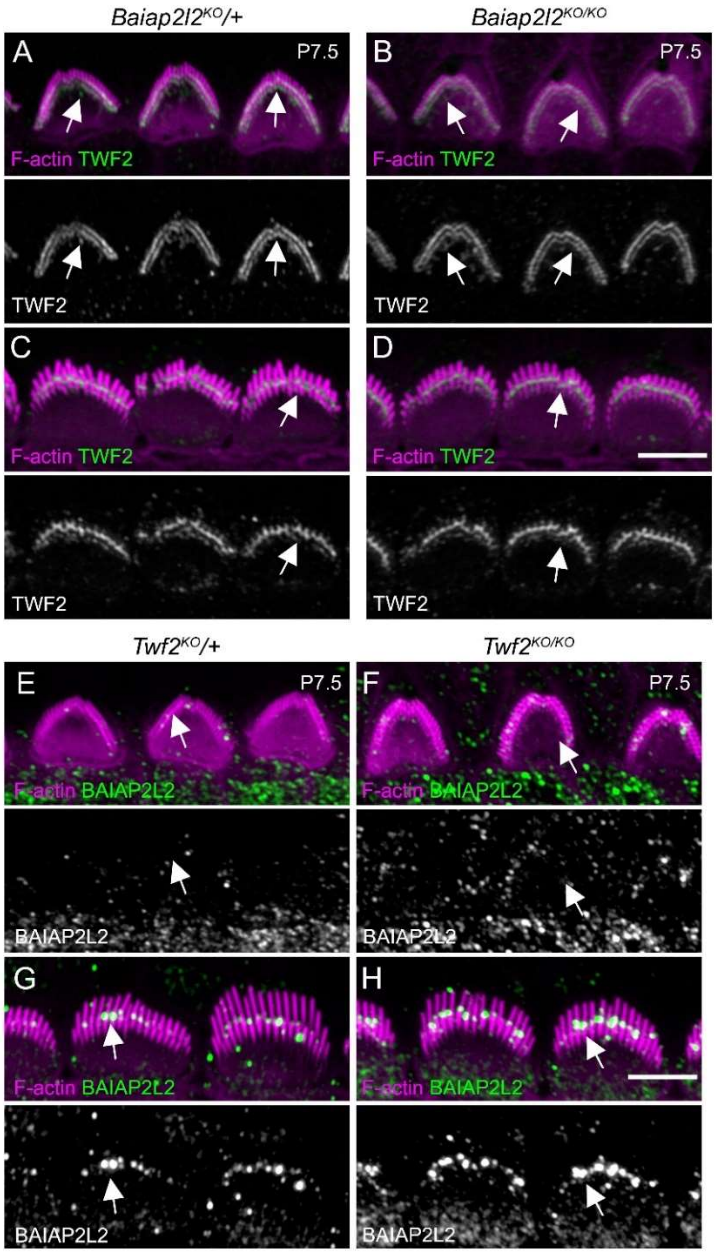

Figure 4-2. BAIAP2L2 and TWF2 localize independently of each other in hair bundles.

(A-D) TWF2 immunostaining in *Baiap2l2*^{KO}*/+* (A, C) or *Baiap2l2*$^{KO/KO}$ (B, D) OHCs (A, B) and IHCs (C, D) at P7.5. (E-H) BAIAP2L2 immunostaining in *Twf2*^{KO}*/+* (E, G) or *Baiap2l2*$^{KO/KO}$ (F, H) OHCs (E, F) and IHCs (G, H) at P7.5. Image intensity is matched for TWF2 or BAIAP2L2 signal of IHCs and OHC for knockout and heterozygotes, but TWF2 signal should not be directly compared to BAIAP2L2 signal.

Images shown are maximum projections that encompass the bundle. Scale, 5 μm. Each immunostaining experiment performed once.

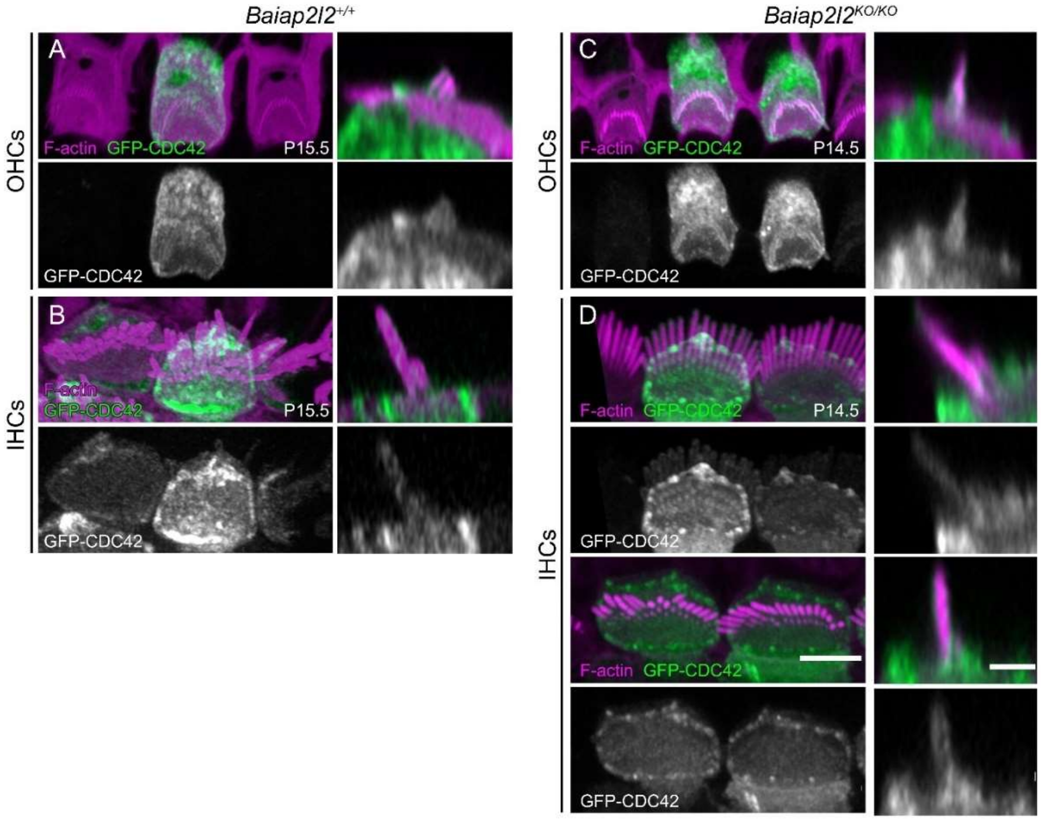

Figure 4-3. Loss of *Baiap2l2* has no obvious effect on CDC42 localization in hair cells.

CDC42 was over-expressed in the cochleas of wild-type (A, B) and *Baiap2l2*-null (C, D) mice following following *in utero* electroporation of AAV1 vector carrying GFP-tagged sequence. Tissue was examined at approximately 2 weeks post-natal (P15.5 or P14.5) for each genotype. Images shown are maximum projections that encompass the bundle (left image for each panel), or x-z reslices (right image for each panel). IHCs (B, D) display slightly different pattern of localization than do OHCs (A, C), where GFP-CDC42 concentrates more strongly at pericuticular necklace of IHCs than of OHCs for both genotypes. GFP-CDC42 distributes evenly along shafts of stereocilia in reslices of both OHCs and IHCs of both genotypes. Scale, 5 μm for maximum projections; 2 μm for x-z reslices. Experiment performed twice for each construct.

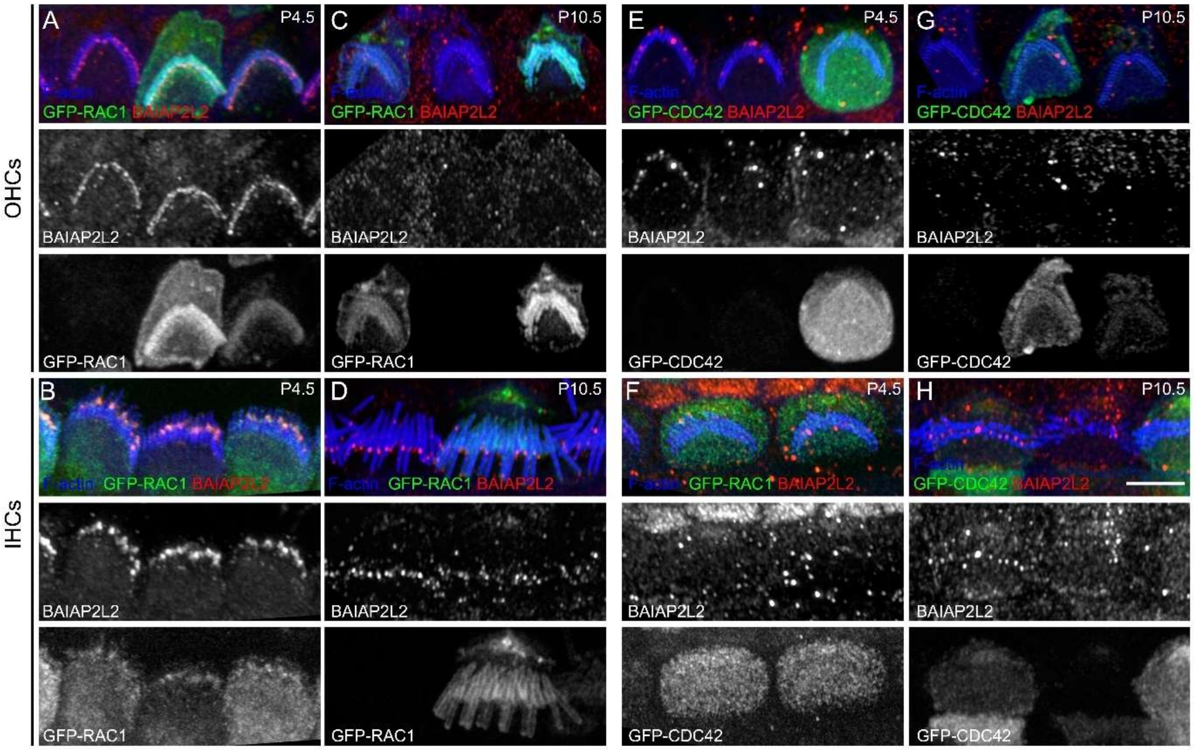

Figure 4-4. RAC1 and CDC42 localization remains stable during early stages of bundle development.

(A-D) RAC1 and (E-H) CDC42 were over-expressed in the cochleas of wild-type mice (CD1 background) following *in utero* electroporation of AAV1 vector carrying GFP-tagged sequence for each small Rho GTPase. Tissue was examined at P4.5 (A, B, E, F) and P10.5 (C, D, G, H) and immunostained against BAIAP2L2. Image intensity is matched for BAIAP2L2 signal of IHCs and OHCs at a given age. GFP signal intensity is adjusted per expression level in selected cells. Images shown are maximum projections that encompass the bundle. Scale, 5 μm. Experiment performed twice for each construct.

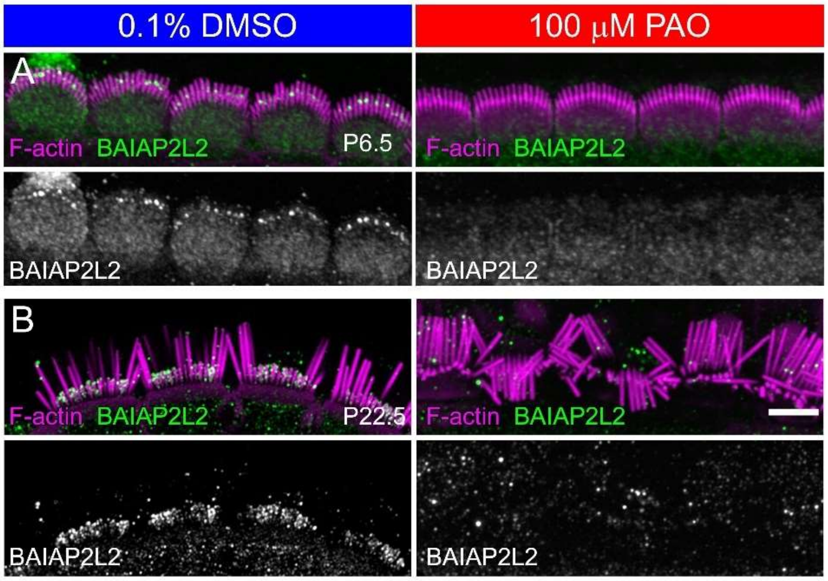

Figure 4-5. PI(4,5)P_2 depletion with PAO reduces BAIAP2L2 immunoreactivity.

Cochleas were isolated from C57BL/6J mice at P6.5 (A) or P22.5 (B), transferred into L-15 supplemented with either 0.1% of the vehicle DMSO (left) or 100 µM PAO (right), incubated for 1 h at 37°C, then fixed and immunostained against BAIAP2L2. Signal intensity is matched for 0.1% DMSO and 100 µM PAO conditions at each age but should not be compared between (A) and (B). Images shown are maximum projections that encompass the bundle. Scale, 5 µm. Experiment performed twice at P6.5, and once at P22.5.

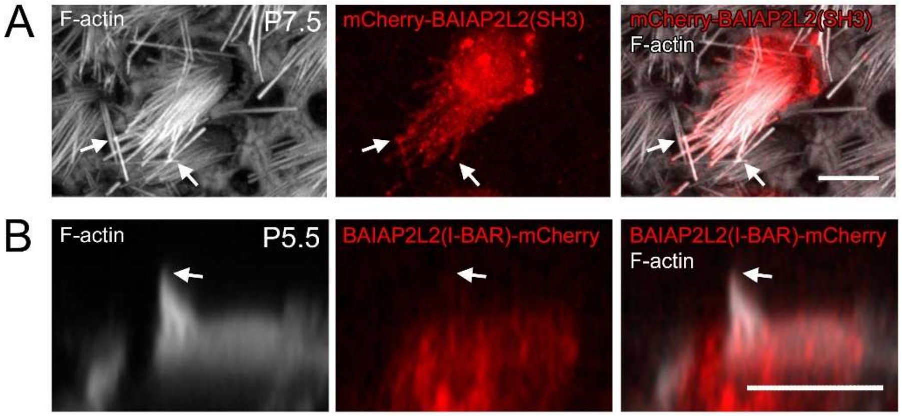

Figure 4-6. BAIAP2L2 requires its SH3 domain to localize to bundles.

BAIAP2L2 fragments were expressed in P6.5 mouse utricle (A) and cochlea (B) following *in utero* electroporation of an adeno-associated viral vector (AAV1) carrying *Baiap2l2* coding sequence of either the SH3 domain alone (A) or the I-BAR domain alone (B). Fragments are tagged with mCherry for visualization. SH3 localization was examined at P7.5; I-BAR localization was examined at P5.5. Arrows mark stereocilia tips. Images shown from the utricle are maximum projections that encompass the bundle. Images shown from the cochlea are re-sliced in x-z axes and depict bundles of OHCs. Scale, 5 μm. Experiments performed 3 times per construct.

Supplemental Methods

Mouse lines

The *Baiap2l2* line used in Fig. 4-1, Fig. 4-2 and Fig. 4-3 is described in detail in Chapter 2. The *Twf2* line, originally obtained from Stefan Heller and maintained on a C57BL/6J background, used in Fig. 4-2 was initially described in Krey et al. (2020). Mice were genotyped using the following primers: wildtype forward 5'-CGGGTACAAGTGCAGCATCAAG-3', wildtype reverse 5'-TCA-CCT-TCT-CCT-AGC-CCC-ATC-C-3', mutant forward 5'-GGT-GCA-CGC-AGG-CAA-CCC-TC-3', and mutant reverse 5'-GTA-CCT-GAC-TGA-TGA-AGT-TCC-TAT-AC-3'. For experiments with transfected constructs in wildtype animals, C57BL/6J males were crossed with CD1 females to generate embryos for microinjection and electroporation.

Immunofluorescence microscopy

Sample preparation, immunolabelling and imaging were carried out as described in Chapters 2 & 3. The rabbit polyclonal anti-TWF2 antibody was used at 1:150.

Staining for CAPZB and EPS8L2 in *Baiap2l2* tissue was carried out twice at P14.5 and once at P22.5 (not shown).

Staining for TWF2 in *Baiap2l2* tissue was carried out once at P7.5 and once at P8.5 (not shown). Imaging was done while blinded to genotype.

Staining for BAIAP2L2 in *Twf2* tissue was carried out once at P7.5. Imaging was done while blinded to genotype.

In utero electroporation of the inner ear

Adeno-associated viral vectors carrying sequence encoding the proteins of interest and NLS-tagged BFP were microinjected through the uterus into the otocyst at embryonic day 11.5 (E11.5). See

Table 4-1 for constructs used. Injected embryos were then electroporated to drive DNA into cells. Methods for surgery are detailed previously (Brigande *et al.*, 2009; Ebrahim *et al.*, 2016a). Tissue was collected at the indicated ages and immunohistochemistry performed as described in Chapters 2 & 3. For samples with mCherry-BAIAP2L2(SH3) or mCherry-BAIAP2L2(I-BAR) alone, F-actin was visualized with 0.4 U/mL Alexa Fluor 488 phalloidin. For samples with GFP-CDC42 alone, F-actin was visualized with 0.4 U/mL CF568 phalloidin. For samples with GFP-RAC1 or GFP-CDC42 co-stained with anti-BAIAP2L2, the same antibody used in Chapters 2 &3 was used at the same dilution (1:150), and F-actin was visualized with 0.8U/mL CF405 phalloidin. Samples were imaged on the setups described in Chapters 2 & 3.

Plasmid name	*Protein ID*	*Residues*
pAAV-BAIAP2L2(I-BAR)-mCherry	Q80Y61	1-239
pAAV-mCherry-BAIAP2L2(SH3)	Q80Y61	324-387
pAAV-GFP-RAC1	P63001	1-192
pAAV-GFP-CDC42	P60766	1-191

Table 4-1. Constructs used for *in utero* electroporation.

Manipulation of PI(4,5)P_2 levels in isolated cochleas by treatment with PAO.

Cochleas were isolated from C57BL/6J mice at the indicated ages and placed into Leibovitz's L-15 medium (L-15) with 5 mM HEPES, pH 7.4 supplemented with either 100 μM phenylarsine oxide (PAO), an inhibitor of PI(4)K that blocks the resynthesis of PI(4,5)P_2, or 0.1% of the vehicle DMSO. For each animal, one cochlea was treated with PAO, and other cochlea was treated with DMSO as a control. Treated cochleas were incubated at 37°C for 1 h in a humidified chamber (small box lined with damp paper towels), then fixed and processed as described in Chapters 2 & 3 for BAIAP2L2 immunostaining. Samples were imaged on the microscopy setup described in Chapters 2 & 3. PAO treatment was performed twice at P6.5, and once at P22.5.

References

Abe, T., Kakehata, S., Kitani, R., Maruya, S., Navaratnam, D., Santos-Sacchi, J., and Shinkawa, H. (2007). Developmental expression of the outer hair cell motor prestin in the mouse. *J Membr Biol* 215, 49-56.

Ahmed, S., Goh, W.I., and Bu, W. (2010). I-BAR domains, IRSp53 and filopodium formation. *Semin Cell Dev Biol* 21, 350-356.

Ahmed, Z.M., Goodyear, R., Riazuddin, S., Lagziel, A., Legan, P.K., Behra, M., Burgess, S.M., Lilley, K.S., Wilcox, E.R., Riazuddin, S., Griffith, A.J., Frolenkov, G.I., Belyantseva, I.A., Richardson, G.P., and Friedman, T.B. (2006). The tip-link antigen, a protein associated with the transduction complex of sensory hair cells, is protocadherin-15. *J Neurosci* 26, 7022-7034.

Assad, J.A., Shepherd, G.M., and Corey, D.P. (1991). Tip-link integrity and mechanical transduction in vertebrate hair cells. *Neuron* 7, 985-994.

Avenarius, M.R., Krey, J.F., Dumont, R.A., Morgan, C.P., Benson, C.B., Vijayakumar, S., Cunningham, C.L., Scheffer, D.I., Corey, D.P., Muller, U., Jones, S.M., and Barr-Gillespie, P.G. (2017). Heterodimeric capping protein is required for stereocilia length and width regulation. *J Cell Biol* 216, 3861-3881.

Barr-Gillespie, P.G. (2015). Assembly of hair bundles, an amazing problem for cell biology. *Mol Biol Cell* 26, 2727-2732.

Bartles, J.R. (2000). Parallel actin bundles and their multiple actin-bundling proteins. *Curr Opin Cell Biol* 12, 72-78.

Bartles, J.R., Zheng, L., Li, A., Wierda, A., and Chen, B. (1998). Small espin: a third actin-bundling protein and potential forked protein ortholog in brush border microvilli. *J Cell Biol* 143, 107-119.

Behlouli, A., Bonnet, C., Abdi, S., Bouaita, A., Lelli, A., Hardelin, J.P., Schietroma, C., Rous, Y., Louha, M., Cheknane, A., Lebdi, H., Boudjelida, K., Makrelouf, M., Zenati, A., and Petit, C. (2014).

EPS8, encoding an actin-binding protein of cochlear hair cell stereocilia, is a new causal gene for autosomal recessive profound deafness. *Orphanet J Rare Dis* 9, 55.

Belyantseva, I.A., Boger, E.T., and Friedman, T.B. (2003). Myosin XVa localizes to the tips of inner ear sensory cell stereocilia and is essential for staircase formation of the hair bundle. *Proc Natl Acad Sci U S A* 100, 13958-13963.

Belyantseva, I.A., Boger, E.T., Naz, S., Frolenkov, G.I., Sellers, J.R., Ahmed, Z.M., Griffith, A.J., and Friedman, T.B. (2005). Myosin-XVa is required for tip localization of whirlin and differential elongation of hair-cell stereocilia. *Nat Cell Biol* 7, 148-156.

Beurg, M., Fettiplace, R., Nam, J.H., and Ricci, A.J. (2009). Localization of inner hair cell mechanotransducer channels using high-speed calcium imaging. *Nat Neurosci* 12, 553-558.

Bilkova, E., Pleskot, R., Rissanen, S., Sun, S., Czogalla, A., Cwiklik, L., Rog, T., Vattulainen, I., Cremer, P.S., Jungwirth, P., and Coskun, U. (2017). Calcium Directly Regulates Phosphatidylinositol 4,5-Bisphosphate Headgroup Conformation and Recognition. *J Am Chem Soc* 139, 4019-4024.

Bird, J.E., Barzik, M., Drummond, M.C., Sutton, D.C., Goodman, S.M., Morozko, E.L., Cole, S.M., Boukhvalova, A.K., Skidmore, J., Syam, D., Wilson, E.A., Fitzgerald, T., Rehman, A.U., Martin, D.M., Boger, E.T., Belyantseva, I.A., and Friedman, T.B. (2017). Harnessing molecular motors for nanoscale pulldown in live cells. *Mol Biol Cell* 28, 463-475.

Bowl, M.R., Simon, M.M., Ingham, N.J., Greenaway, S., Santos, L., Cater, H., Taylor, S., Mason, J., Kurbatova, N., Pearson, S., Bower, L.R., Clary, D.A., Meziane, H., Reilly, P., Minowa, O., Kelsey, L., International Mouse Phenotyping, C., Tocchini-Valentini, G.P., Gao, X., Bradley, A., Skarnes, W.C., Moore, M., Beaudet, A.L., Justice, M.J., Seavitt, J., Dickinson, M.E., Wurst, W., de Angelis, M.H., Herault, Y., Wakana, S., Nutter, L.M.J., Flenniken, A.M., McKerlie, C., Murray, S.A., Svenson, K.L., Braun, R.E., West, D.B., Lloyd, K.C.K., Adams, D.J., White, J., Karp, N., Flicek, P., Smedley, D., Meehan, T.F., Parkinson, H.E., Teboul, L.M., Wells, S., Steel, K.P., Mallon, A.M., and Brown, S.D.M. (2017). A large scale hearing loss screen reveals an extensive unexplored genetic landscape for auditory dysfunction. *Nat Commun* 8, 886.

Bradley, R.P., Slochower, D.R., Janmey, P.A., and Radhakrishnan, R. (2020). Divalent cations bind to phosphoinositides to induce ion and isomer specific propensities for nano-cluster initiation in bilayer membranes. *R Soc Open Sci* 7, 192208.

Brigande, J.V., Gubbels, S.P., Woessner, D.W., Jungwirth, J.J., and Bresee, C.S. (2009). Electroporation-mediated gene transfer to the developing mouse inner ear. *Methods Mol Biol* 493, 125-139.

Carlton, A.J., Halford, J., Underhill, A., Jeng, J.Y., Avenarius, M.R., Gilbert, M.L., Ceriani, F., Ebisine, K., Brown, S.D.M., Bowl, M.R., Barr-Gillespie, P.G., and Marcotti, W. (2021). Loss of Baiap2l2 destabilizes the transducing stereocilia of cochlear hair cells and leads to deafness. *J Physiol* 599, 1173-1198.

Carman, P.J., and Dominguez, R. (2018). BAR domain proteins-a linkage between cellular membranes, signaling pathways, and the actin cytoskeleton. *Biophys Rev* 10, 1587-1604.

Carpena, N.T., and Lee, M.Y. (2018). Genetic Hearing Loss and Gene Therapy. *Genomics Inform* 16, e20.

Choi, J., Ko, J., Racz, B., Burette, A., Lee, J.R., Kim, S., Na, M., Lee, H.W., Kim, K., Weinberg, R.J., and Kim, E. (2005). Regulation of dendritic spine morphogenesis by insulin receptor substrate 53, a downstream effector of Rac1 and Cdc42 small GTPases. *J Neurosci* 25, 869-879.

Chou, A.M., Sem, K.P., Lam, W.J., Ahmed, S., and Lim, C.Y. (2017). Redundant functions of I-BAR family members, IRSp53 and IRTKS, are essential for embryonic development. *Sci Rep* 7, 40485.

Corns, L.F., Johnson, S.L., Kros, C.J., and Marcotti, W. (2014). Calcium entry into stereocilia drives adaptation of the mechanoelectrical transducer current of mammalian cochlear hair cells. *Proc Natl Acad Sci U S A* 111, 14918-14923.

Corns, L.F., Johnson, S.L., Roberts, T., Ranatunga, K.M., Hendry, A., Ceriani, F., Safieddine, S., Steel, K.P., Forge, A., Petit, C., Furness, D.N., Kros, C.J., and Marcotti, W. (2018). Mechanotransduction is required for establishing and maintaining mature inner hair cells and regulating efferent innervation. *Nat Commun* 9, 4015.

Cosgrove, D., and Zallocchi, M. (2014). Usher protein functions in hair cells and photoreceptors. *Int J Biochem Cell Biol* 46, 80-89.

Croce, A., Cassata, G., Disanza, A., Gagliani, M.C., Tacchetti, C., Malabarba, M.G., Carlier, M.F., Scita, G., Baumeister, R., and Di Fiore, P.P. (2004). A novel actin barbed-end-capping activity in EPS-8 regulates apical morphogenesis in intestinal cells of Caenorhabditis elegans. *Nat Cell Biol* 6, 1173-1179.

Cunningham, C.L., Qiu, X., Wu, Z., Zhao, B., Peng, G., Kim, Y.H., Lauer, A., and Muller, U. (2020). TMIE Defines Pore and Gating Properties of the Mechanotransduction Channel of Mammalian Cochlear Hair Cells. *Neuron* 107, 126-143 e128.

Drummond, M.C., Belyantseva, I.A., Friderici, K.H., and Friedman, T.B. (2012). Actin in hair cells and hearing loss. *Hear Res* 288, 89-99.

Du, H., Zhou, H., Sun, Y., Zhai, X., Chen, Z., Wang, Y., and Xu, Z. (2021). The Rho GTPase Cell Division Cycle 42 Regulates Stereocilia Development in Cochlear Hair Cells. *Front Cell Dev Biol* 9, 765559.

Ebrahim, S., Avenarius, M.R., Grati, M., Krey, J.F., Windsor, A.M., Sousa, A.D., Ballesteros, A., Cui, R., Millis, B.A., Salles, F.T., Baird, M.A., Davidson, M.W., Jones, S.M., Choi, D., Dong, L., Raval, M.H., Yengo, C.M., Barr-Gillespie, P.G., and Kachar, B. (2016a). Stereocilia-staircase spacing is influenced by myosin III motors and their cargos espin-1 and espin-like. *Nat Commun* 7, 10833.

Ebrahim, S., Ingham, N.J., Lewis, M.A., Rogers, M.J.C., Cui, R., Kachar, B., Pass, J.C., and Steel, K.P. (2016b). Alternative Splice Forms Influence Functions of Whirlin in Mechanosensory Hair Cell Stereocilia. *Cell Rep* 15, 935-943.

Effertz, T., Becker, L., Peng, A.W., and Ricci, A.J. (2017). Phosphoinositol-4,5-Bisphosphate Regulates Auditory Hair-Cell Mechanotransduction-Channel Pore Properties and Fast Adaptation. *J Neurosci* 37, 11632-11646.

Ehret, G. (1983). Development of hearing and response behavior to sound stimuli, behavioral studies. In: Development of the Auditory and Vestibular Systems, ed. R. Romand, New York, NY: Academic Press, 211-237.

Ellenbroek, W.G., Wang, Y.H., Christian, D.A., Discher, D.E., Janmey, P.A., and Liu, A.J. (2011). Divalent cation-dependent formation of electrostatic PIP2 clusters in lipid monolayers. *Biophys J* 101, 2178-2184.

Erway, L.C., Shiau, Y.W., Davis, R.R., and Krieg, E.F. (1996). Genetics of age-related hearing loss in mice. III. Susceptibility of inbred and F1 hybrid strains to noise-induced hearing loss. *Hear Res* 93, 181-187.

Fang, Q., Indzhykulian, A.A., Mustapha, M., Riordan, G.P., Dolan, D.F., Friedman, T.B., Belyantseva, I.A., Frolenkov, G.I., Camper, S.A., and Bird, J.E. (2015). The 133-kDa N-terminal domain enables myosin 15 to maintain mechanotransducing stereocilia and is essential for hearing. *Elife* 4.

Fettiplace, R. (2017). Hair Cell Transduction, Tuning, and Synaptic Transmission in the Mammalian Cochlea. *Compr Physiol* 7, 1197-1227.

Fettiplace, R., and Kim, K.X. (2014). The physiology of mechanoelectrical transduction channels in hearing. *Physiol Rev* 94, 951-986.

Frolenkov, G.I., Belyantseva, I.A., Friedman, T.B., and Griffith, A.J. (2004). Genetic insights into the morphogenesis of inner ear hair cells. *Nat Rev Genet* 5, 489-498.

Furness, D.N., and Hackney, C.M. (1986). High-resolution scanning-electron microscopy of stereocilia using the osmium-thiocarbohydrazide coating technique. *Hear Res* 21, 243-249.

Furness, D.N., Johnson, S.L., Manor, U., Ruttiger, L., Tocchetti, A., Offenhauser, N., Olt, J., Goodyear, R.J., Vijayakumar, S., Dai, Y., Hackney, C.M., Franz, C., Di Fiore, P.P., Masetto, S., Jones, S.M., Knipper, M., Holley, M.C., Richardson, G.P., Kachar, B., and Marcotti, W. (2013). Progressive hearing loss and gradual deterioration of sensory hair bundles in the ears of mice lacking the actin-binding protein Eps8L2. *Proc Natl Acad Sci U S A* 110, 13898-13903.

Gaeta, I.M., Meenderink, L.M., Postema, M.M., Cencer, C.S., and Tyska, M.J. (2021). Direct visualization of epithelial microvilli biogenesis. *Curr Biol* 31, 2561-2575 e2566.

Giese, A.P.J., Tang, Y.Q., Sinha, G.P., Bowl, M.R., Goldring, A.C., Parker, A., Freeman, M.J., Brown, S.D.M., Riazuddin, S., Fettiplace, R., Schafer, W.R., Frolenkov, G.I., and Ahmed, Z.M. (2017). CIB2 interacts with TMC1 and TMC2 and is essential for mechanotransduction in auditory hair cells. *Nat Commun* 8, 43.

Gillespie, P.G., and Muller, U. (2009). Mechanotransduction by hair cells: models, molecules, and mechanisms. *Cell* 139, 33-44.

Glowatzki, E., Ruppersberg, J.P., Zenner, H.P., and Rusch, A. (1997). Mechanically and ATP-induced currents of mouse outer hair cells are independent and differentially blocked by d-tubocurarine. *Neuropharmacology* 36, 1269-1275.

Goh, W.I., Lim, K.B., Sudhaharan, T., Sem, K.P., Bu, W., Chou, A.M., and Ahmed, S. (2012). mDia1 and WAVE2 proteins interact directly with IRSp53 in filopodia and are involved in filopodium formation. *J Biol Chem* 287, 4702-4714.

Goodyear, R.J., Marcotti, W., Kros, C.J., and Richardson, G.P. (2005). Development and properties of stereociliary link types in hair cells of the mouse cochlea. *J Comp Neurol* 485, 75-85.

Grimsley-Myers, C.M., Sipe, C.W., Geleoc, G.S., and Lu, X. (2009). The small GTPase Rac1 regulates auditory hair cell morphogenesis. *J Neurosci* 29, 15859-15869.

Gurumurthy, C.B., Sato, M., Nakamura, A., Inui, M., Kawano, N., Islam, M.A., Ogiwara, S., Takabayashi, S., Matsuyama, M., Nakagawa, S., Miura, H., and Ohtsuka, M. (2019). Creation of CRISPR-based germline-genome-engineered mice without ex vivo handling of zygotes by i-GONAD. *Nat Protoc* 14, 2452-2482.

Hackney, C.M., Mahendrasingam, S., Penn, A., and Fettiplace, R. (2005). The concentrations of calcium buffering proteins in mammalian cochlear hair cells. *J Neurosci* 25, 7867-7875.

Hertzog, M., Milanesi, F., Hazelwood, L., Disanza, A., Liu, H., Perlade, E., Malabarba, M.G., Pasqualato, S., Maiolica, A., Confalonieri, S., Le Clainche, C., Offenhauser, N., Block, J., Rottner, K., Di

Fiore, P.P., Carlier, M.F., Volkmann, N., Hanein, D., and Scita, G. (2010). Molecular basis for the dual function of Eps8 on actin dynamics: bundling and capping. *PLoS Biol* 8, e1000387.

Hirono, M., Denis, C.S., Richardson, G.P., and Gillespie, P.G. (2004). Hair cells require phosphatidylinositol 4,5-bisphosphate for mechanical transduction and adaptation. *Neuron* 44, 309-320.

Hudspeth, A.J. (1997). How hearing happens. *Neuron* 19, 947-950.

Ingham, N.J., Pearson, S., and Steel, K.P. (2011). Using the Auditory Brainstem Response (ABR) to Determine Sensitivity of Hearing in Mutant Mice. *Curr Protoc Mouse Biol* 1, 279-287.

Jeng, J.Y., Johnson, S.L., Carlton, A.J., De Tomasi, L., Goodyear, R.J., De Faveri, F., Furness, D.N., Wells, S., Brown, S.D.M., Holley, M.C., Richardson, G.P., Mustapha, M., Bowl, M.R., and Marcotti, W. (2020). Age-related changes in the biophysical and morphological characteristics of mouse cochlear outer hair cells. *J Physiol* 598, 3891-3910.

Johnson, K.R., Erway, L.C., Cook, S.A., Willott, J.F., and Zheng, Q.Y. (1997). A major gene affecting age-related hearing loss in C57BL/6J mice. *Hear Res* 114, 83-92.

Kachar, B., Parakkal, M., Kurc, M., Zhao, Y., and Gillespie, P.G. (2000). High-resolution structure of hair-cell tip links. *Proc Natl Acad Sci U S A* 97, 13336-13341.

Kaltenbach, J.A., Falzarano, P.R., and Simpson, T.H. (1994). Postnatal development of the hamster cochlea. II. Growth and differentiation of stereocilia bundles. *J Comp Neurol* 350, 187-198.

Kast, D.J., Yang, C., Disanza, A., Boczkowska, M., Madasu, Y., Scita, G., Svitkina, T., and Dominguez, R. (2014). Mechanism of IRSp53 inhibition and combinatorial activation by Cdc42 and downstream effectors. *Nat Struct Mol Biol* 21, 413-422.

Kawashima, Y., Kurima, K., Pan, B., Griffith, A.J., and Holt, J.R. (2015). Transmembrane channel-like (TMC) genes are required for auditory and vestibular mechanosensation. *Pflugers Arch* 467, 85-94.

Kirjavainen, A., Laos, M., Anttonen, T., and Pirvola, U. (2015). The Rho GTPase Cdc42 regulates hair cell planar polarity and cellular patterning in the developing cochlea. *Biol Open* 4, 516-526.

Kitajiri, S., Fukumoto, K., Hata, M., Sasaki, H., Katsuno, T., Nakagawa, T., Ito, J., Tsukita, S., and Tsukita, S. (2004). Radixin deficiency causes deafness associated with progressive degeneration of cochlear stereocilia. *J Cell Biol* 166, 559-570.

Kolla, L., Kelly, M.C., Mann, Z.F., Anaya-Rocha, A., Ellis, K., Lemons, A., Palermo, A.T., So, K.S., Mays, J.C., Orvis, J., Burns, J.C., Hertzano, R., Driver, E.C., and Kelley, M.W. (2020). Characterization of the development of the mouse cochlear epithelium at the single cell level. *Nat Commun* 11, 2389.

Koster, D.V., and Mayor, S. (2016). Cortical actin and the plasma membrane: inextricably intertwined. *Curr Opin Cell Biol* 38, 81-89.

Krey, J.F., Chatterjee, P., Dumont, R.A., O'Sullivan, M., Choi, D., Bird, J.E., and Barr-Gillespie, P.G. (2020). Mechanotransduction-Dependent Control of Stereocilia Dimensions and Row Identity in Inner Hair Cells. *Curr Biol* 30, 442-454 e447.

Kros, C.J., Ruppersberg, J.P., and Rusch, A. (1998). Expression of a potassium current in inner hair cells during development of hearing in mice. *Nature* 394, 281-284.

Kurochkina, N., and Guha, U. (2013). SH3 domains: modules of protein-protein interactions. *Biophys Rev* 5, 29-39.

Lee, S.H., Kerff, F., Chereau, D., Ferron, F., Klug, A., and Dominguez, R. (2007). Structural basis for the actin-binding function of missing-in-metastasis. *Structure* 15, 145-155.

Liang, X., Qiu, X., Dionne, G., Cunningham, C.L., Pucak, M.L., Peng, G., Kim, Y.H., Lauer, A., Shapiro, L., and Muller, U. (2021). CIB2 and CIB3 are auxiliary subunits of the mechanotransduction channel of hair cells. *Neuron* 109, 2131-2149 e2115.

Lin, L., Shi, Y., Wang, M., Wang, C., Lu, Q., Zhu, J., and Zhang, R. (2021). Phase separation-mediated condensation of Whirlin-Myo15-Eps8 stereocilia tip complex. *Cell Rep* 34, 108770.

Liu, C., and Hermann, T.E. (1978). Characterization of ionomycin as a calcium ionophore. *J Biol Chem* 253, 5892-5894.

Manor, U., Disanza, A., Grati, M., Andrade, L., Lin, H., Di Fiore, P.P., Scita, G., and Kachar, B. (2011). Regulation of stereocilia length by myosin XVa and whirlin depends on the actin-regulatory protein Eps8. *Curr Biol* 21, 167-172.

Manor, U., and Kachar, B. (2008). Dynamic length regulation of sensory stereocilia. *Semin Cell Dev Biol* 19, 502-510.

Marcotti, W., Corns, L.F., Goodyear, R.J., Rzadzinska, A.K., Avraham, K.B., Steel, K.P., Richardson, G.P., and Kros, C.J. (2016). The acquisition of mechano-electrical transducer current adaptation in auditory hair cells requires myosin VI. *J Physiol* 594, 3667-3681.

Marcotti, W., Johnson, S.L., Holley, M.C., and Kros, C.J. (2003). Developmental changes in the expression of potassium currents of embryonic, neonatal and mature mouse inner hair cells. *J Physiol* 548, 383-400.

Marcotti, W., Johnson, S.L., and Kros, C.J. (2004). Effects of intracellular stores and extracellular Ca(2+) on Ca(2+)-activated K(+) currents in mature mouse inner hair cells. *J Physiol* 557, 613-633.

Marcotti, W., and Kros, C.J. (1999). Developmental expression of the potassium current IK,n contributes to maturation of mouse outer hair cells. *J Physiol* 520 Pt 3, 653-660.

Martin, G.K., Stagner, B.B., and Lonsbury-Martin, B.L. (2006). Assessment of cochlear function in mice: distortion-product otoacoustic emissions. *Curr Protoc Neurosci* Chapter 8, Unit8 21C.

Mattila, P.K., Pykalainen, A., Saarikangas, J., Paavilainen, V.O., Vihinen, H., Jokitalo, E., and Lappalainen, P. (2007). Missing-in-metastasis and IRSp53 deform PI(4,5)P2-rich membranes by an inverse BAR domain-like mechanism. *J Cell Biol* 176, 953-964.

Mburu, P., Mustapha, M., Varela, A., Weil, D., El-Amraoui, A., Holme, R.H., Rump, A., Hardisty, R.E., Blanchard, S., Coimbra, R.S., Perfettini, I., Parkinson, N., Mallon, A.M., Glenister, P., Rogers, M.J., Paige, A.J., Moir, L., Clay, J., Rosenthal, A., Liu, X.Z., Blanco, G., Steel, K.P., Petit, C., and Brown, S.D. (2003). Defects in whirlin, a PDZ domain molecule involved in stereocilia elongation, cause deafness in the whirler mouse and families with DFNB31. *Nat Genet* 34, 421-428.

Mburu, P., Romero, M.R., Hilton, H., Parker, A., Townsend, S., Kikkawa, Y., and Brown, S.D. (2010). Gelsolin plays a role in the actin polymerization complex of hair cell stereocilia. *PLoS One* 5, e11627.

McGrath, J., Tung, C.Y., Liao, X., Belyantseva, I.A., Roy, P., Chakraborty, O., Li, J., Berbari, N.F., Faaborg-Andersen, C.C., Barzik, M., Bird, J.E., Zhao, B., Balakrishnan, L., Friedman, T.B., and Perrin, B.J. (2021). Actin at stereocilia tips is regulated by mechanotransduction and ADF/cofilin. *Curr Biol* 31, 1141-1153 e1147.

Menna, E., Disanza, A., Cagnoli, C., Schenk, U., Gelsomino, G., Frittoli, E., Hertzog, M., Offenhauser, N., Sawallisch, C., Kreienkamp, H.J., Gertler, F.B., Di Fiore, P.P., Scita, G., and Matteoli, M. (2009). Eps8 regulates axonal filopodia in hippocampal neurons in response to brain-derived neurotrophic factor (BDNF). *PLoS Biol* 7, e1000138.

Meyers, J.R., MacDonald, R.B., Duggan, A., Lenzi, D., Standaert, D.G., Corwin, J.T., and Corey, D.P. (2003). Lighting up the senses: FM1-43 loading of sensory cells through nonselective ion channels. *J Neurosci* 23, 4054-4065.

Mikaelian, D., and Ruben, R.J. (1964). Development of hearing in the normal CBA-J mouse: correlation of physiological observations with behavioural responses and with cochlear anatomy. . *Acta Otolaryngol* 59, 451-461.

Millard, T.H., Bompard, G., Heung, M.Y., Dafforn, T.R., Scott, D.J., Machesky, L.M., and Futterer, K. (2005). Structural basis of filopodia formation induced by the IRSp53/MIM homology domain of human IRSp53. *EMBO J* 24, 240-250.

Moller, A.R., and Jannetta, P.J. (1982). Evoked potentials from the inferior colliculus in man. *Electroencephalogr Clin Neurophysiol* 53, 612-620.

Morozko, E.L., Nishio, A., Ingham, N.J., Chandra, R., Fitzgerald, T., Martelletti, E., Borck, G., Wilson, E., Riordan, G.P., Wangemann, P., Forge, A., Steel, K.P., Liddle, R.A., Friedman, T.B., and Belyantseva, I.A. (2015). ILDR1 null mice, a model of human deafness DFNB42, show structural aberrations of tricellular tight junctions and degeneration of auditory hair cells. *Hum Mol Genet* 24, 609-624.

Mutai, H., Momozawa, Y., Kamatani, Y., Nakano, A., Sakamoto, H., Takiguchi, T., Nara, K., Kubo, M., and Matsunaga, T. (2022). Whole exome analysis of patients in Japan with hearing loss reveals high heterogeneity among responsible and novel candidate genes. *Orphanet J Rare Dis* 17, 114.

Noben-Trauth, K., Zheng, Q.Y., and Johnson, K.R. (2003). Association of cadherin 23 with polygenic inheritance and genetic modification of sensorineural hearing loss. *Nat Genet* 35, 21-23.

Offenhauser, N., Borgonovo, A., Disanza, A., Romano, P., Ponzanelli, I., Iannolo, G., Di Fiore, P.P., and Scita, G. (2004). The eps8 family of proteins links growth factor stimulation to actin reorganization generating functional redundancy in the Ras/Rac pathway. *Mol Biol Cell* 15, 91-98.

Ohtsuka, M., and Sato, M. (2019). i-GONAD: A method for generating genome-edited animals without ex vivo handling of embryos. *Dev Growth Differ* 61, 306-315.

Oliver, D., Knipper, M., Derst, C., and Fakler, B. (2003). Resting potential and submembrane calcium concentration of inner hair cells in the isolated mouse cochlea are set by KCNQ-type potassium channels. *J Neurosci* 23, 2141-2149.

Olt, J., Mburu, P., Johnson, S.L., Parker, A., Kuhn, S., Bowl, M., Marcotti, W., and Brown, S.D. (2014). The actin-binding proteins eps8 and gelsolin have complementary roles in regulating the growth and stability of mechanosensory hair bundles of mammalian cochlear outer hair cells. *PLoS One* 9, e87331.

Pan, B., Akyuz, N., Liu, X.P., Asai, Y., Nist-Lund, C., Kurima, K., Derfler, B.H., Gyorgy, B., Limapichat, W., Walujkar, S., Wimalasena, L.N., Sotomayor, M., Corey, D.P., and Holt, J.R. (2018). TMC1 Forms the Pore of Mechanosensory Transduction Channels in Vertebrate Inner Ear Hair Cells. *Neuron* 99, 736-753 e736.

Paunola, E., Mattila, P.K., and Lappalainen, P. (2002). WH2 domain: a small, versatile adapter for actin monomers. *FEBS Lett* 513, 92-97.

Pawlowski, K.S., Kikkawa, Y.S., Wright, C.G., and Alagramam, K.N. (2006). Progression of inner ear pathology in Ames waltzer mice and the role of protocadherin 15 in hair cell development. *J Assoc Res Otolaryngol* 7, 83-94.

Peng, A.W., Belyantseva, I.A., Hsu, P.D., Friedman, T.B., and Heller, S. (2009). Twinfilin 2 regulates actin filament lengths in cochlear stereocilia. *J Neurosci* 29, 15083-15088.

Peter, B.J., Kent, H.M., Mills, I.G., Vallis, Y., Butler, P.J., Evans, P.R., and McMahon, H.T. (2004). BAR domains as sensors of membrane curvature: the amphiphysin BAR structure. *Science* 303, 495-499.

Petit, C., and Richardson, G.P. (2009). Linking genes underlying deafness to hair-bundle development and function. *Nat Neurosci* 12, 703-710.

Pickles, J.O., Rouse, G.W., and von Perger, M. (1991). Morphological correlates of mechanotransduction in acousticolateral hair cells. *Scanning Microsc* 5, 1115-1124; discussion 1124-1118.

Postema, M.M., Grega-Larson, N.E., Neininger, A.C., and Tyska, M.J. (2018). IRTKS (BAIAP2L1) Elongates Epithelial Microvilli Using EPS8-Dependent and Independent Mechanisms. *Curr Biol* 28, 2876-2888 e2874.

Powers, R.J., Roy, S., Atilgan, E., Brownell, W.E., Sun, S.X., Gillespie, P.G., and Spector, A.A. (2012). Stereocilia membrane deformation: implications for the gating spring and mechanotransduction channel. *Biophys J* 102, 201-210.

Probst, F.J., Fridell, R.A., Raphael, Y., Saunders, T.L., Wang, A., Liang, Y., Morell, R.J., Touchman, J.W., Lyons, R.H., Noben-Trauth, K., Friedman, T.B., and Camper, S.A. (1998). Correction of deafness in shaker-2 mice by an unconventional myosin in a BAC transgene. *Science* 280, 1444-1447.

Pykalainen, A., Boczkowska, M., Zhao, H., Saarikangas, J., Rebowski, G., Jansen, M., Hakanen, J., Koskela, E.V., Peranen, J., Vihinen, H., Jokitalo, E., Salminen, M., Ikonen, E., Dominguez, R., and Lappalainen, P. (2011). Pinkbar is an epithelial-specific BAR domain protein that generates planar membrane structures. *Nat Struct Mol Biol* 18, 902-907.

Rehman, A.U., Bird, J.E., Faridi, R., Shahzad, M., Shah, S., Lee, K., Khan, S.N., Imtiaz, A., Ahmed, Z.M., Riazuddin, S., Santos-Cortez, R.L., Ahmad, W., Leal, S.M., Riazuddin, S., and Friedman, T.B. (2016). Mutational Spectrum of MYO15A and the Molecular Mechanisms of DFNB3 Human Deafness. *Hum Mutat* 37, 991-1003.

Riazuddin, S., Belyantseva, I.A., Giese, A.P., Lee, K., Indzhykulian, A.A., Nandamuri, S.P., Yousaf, R., Sinha, G.P., Lee, S., Terrell, D., Hegde, R.S., Ali, R.A., Anwar, S., Andrade-Elizondo, P.B., Sirmaci, A., Parise, L.V., Basit, S., Wali, A., Ayub, M., Ansar, M., Ahmad, W., Khan, S.N., Akram, J., Tekin, M., Riazuddin, S., Cook, T., Buschbeck, E.K., Frolenkov, G.I., Leal, S.M., Friedman, T.B., and Ahmed, Z.M. (2012). Alterations of the CIB2 calcium- and integrin-binding protein cause Usher syndrome type 1J and nonsyndromic deafness DFNB48. *Nat Genet* 44, 1265-1271.

Romand, R. (1983). Development in the frequency selectivity of auditory nerve fibers in the kitten. *Neurosci Lett* 35, 271-276.

Roth, B., and Bruns, V. (1992). Postnatal development of the rat organ of Corti. II. Hair cell receptors and their supporting elements. *Anat Embryol (Berl)* 185, 571-581.

Rzadzinska, A.K., Schneider, M.E., Davies, C., Riordan, G.P., and Kachar, B. (2004). An actin molecular treadmill and myosins maintain stereocilia functional architecture and self-renewal. *J Cell Biol* 164, 887-897.

Saarikangas, J., Hakanen, J., Mattila, P.K., Grumet, M., Salminen, M., and Lappalainen, P. (2008). ABBA regulates plasma-membrane and actin dynamics to promote radial glia extension. *J Cell Sci* 121, 1444-1454.

Saarikangas, J., Kourdougli, N., Senju, Y., Chazal, G., Segerstrale, M., Minkeviciene, R., Kuurne, J., Mattila, P.K., Garrett, L., Holter, S.M., Becker, L., Racz, I., Hans, W., Klopstock, T., Wurst, W., Zimmer, A., Fuchs, H., Gailus-Durner, V., Hrabe de Angelis, M., von Ossowski, L., Taira, T., Lappalainen, P., Rivera, C., and Hotulainen, P. (2015). MIM-Induced Membrane Bending Promotes Dendritic Spine Initiation. *Dev Cell* 33, 644-659.

Saarikangas, J., Zhao, H., and Lappalainen, P. (2010). Regulation of the actin cytoskeleton-plasma membrane interplay by phosphoinositides. *Physiol Rev* 90, 259-289.

Saarikangas, J., Zhao, H., Pykalainen, A., Laurinmaki, P., Mattila, P.K., Kinnunen, P.K., Butcher, S.J., and Lappalainen, P. (2009). Molecular mechanisms of membrane deformation by I-BAR domain proteins. *Curr Biol* 19, 95-107.

Sakane, A., Abdallah, A.A., Nakano, K., Honda, K., Ikeda, W., Nishikawa, Y., Matsumoto, M., Matsushita, N., Kitamura, T., and Sasaki, T. (2012). Rab13 small G protein and junctional Rab13-binding protein (JRAB) orchestrate actin cytoskeletal organization during epithelial junctional development. *J Biol Chem* 287, 42455-42468.

Schaette, R., and McAlpine, D. (2011). Tinnitus with a normal audiogram: physiological evidence for hidden hearing loss and computational model. *J Neurosci* 31, 13452-13457.

Scheffer, D.I., Shen, J., Corey, D.P., and Chen, Z.Y. (2015). Gene Expression by Mouse Inner Ear Hair Cells during Development. *J Neurosci* 35, 6366-6380.

Sekerkova, G., Loomis, P.A., Changyaleket, B., Zheng, L., Eytan, R., Chen, B., Mugnaini, E., and Bartles, J.R. (2003). Novel espin actin-bundling proteins are localized to Purkinje cell dendritic spines and bind the Src homology 3 adapter protein insulin receptor substrate p53. *J Neurosci* 23, 1310-1319.

Sekerkova, G., Richter, C.P., and Bartles, J.R. (2011). Roles of the espin actin-bundling proteins in the morphogenesis and stabilization of hair cell stereocilia revealed in CBA/CaJ congenic jerker mice. *PLoS Genet* 7, e1002032.

Shin, J.B., Krey, J.F., Hassan, A., Metlagel, Z., Tauscher, A.N., Pagana, J.M., Sherman, N.E., Jeffery, E.D., Spinelli, K.J., Zhao, H., Wilmarth, P.A., Choi, D., David, L.L., Auer, M., and Barr-Gillespie, P.G. (2013). Molecular architecture of the chick vestibular hair bundle. *Nat Neurosci* 16, 365-374.

Soderberg, O., Gullberg, M., Jarvius, M., Ridderstrale, K., Leuchowius, K.J., Jarvius, J., Wester, K., Hydbring, P., Bahram, F., Larsson, L.G., and Landegren, U. (2006). Direct observation of individual endogenous protein complexes in situ by proximity ligation. *Nat Methods* 3, 995-1000.

Sudhaharan, T., Sem, K.P., Liew, H.F., Yu, Y.H., Goh, W.I., Chou, A.M., and Ahmed, S. (2016). The Rho GTPase Rif signals through IRTKS, Eps8 and WAVE2 to generate dorsal membrane ruffles and filopodia. *J Cell Sci* 129, 2829-2840.

Suetsugu, S., Kurisu, S., Oikawa, T., Yamazaki, D., Oda, A., and Takenawa, T. (2006). Optimization of WAVE2 complex-induced actin polymerization by membrane-bound IRSp53, PIP(3), and Rac. *J Cell Biol* 173, 571-585.

Tadenev, A.L.D., Akturk, A., Devanney, N., Mathur, P.D., Clark, A.M., Yang, J., and Tarchini, B. (2019). GPSM2-GNAI Specifies the Tallest Stereocilia and Defines Hair Bundle Row Identity. *Curr Biol* 29, 921-934 e924.

Takei, K., Slepnev, V.I., Haucke, V., and De Camilli, P. (1999). Functional partnership between amphiphysin and dynamin in clathrin-mediated endocytosis. *Nat Cell Biol* 1, 33-39.

Tarchini, B., Tadenev, A.L., Devanney, N., and Cayouette, M. (2016). A link between planar polarity and staircase-like bundle architecture in hair cells. *Development* 143, 3926-3932.

Tilney, L.G., Derosier, D.J., and Mulroy, M.J. (1980). The organization of actin filaments in the stereocilia of cochlear hair cells. *J Cell Biol* 86, 244-259.

Tilney, L.G., Tilney, M.S., and DeRosier, D.J. (1992). Actin filaments, stereocilia, and hair cells: how cells count and measure. *Annu Rev Cell Biol* 8, 257-274.

Ueyama, T., Sakaguchi, H., Nakamura, T., Goto, A., Morioka, S., Shimizu, A., Nakao, K., Hishikawa, Y., Ninoyu, Y., Kassai, H., Suetsugu, S., Koji, T., Fritzsch, B., Yonemura, S., Hisa, Y., Matsuda, M., Aiba, A., and Saito, N. (2014). Maintenance of stereocilia and apical junctional complexes by Cdc42 in cochlear hair cells. *J Cell Sci* 127, 2040-2052.

Varnai, P., and Balla, T. (1998). Visualization of phosphoinositides that bind pleckstrin homology domains: calcium- and agonist-induced dynamic changes and relationship to myo-[3H]inositol-labeled phosphoinositide pools. *J Cell Biol* 143, 501-510.

Vartiainen, M.K., Sarkkinen, E.M., Matilainen, T., Salminen, M., and Lappalainen, P. (2003). Mammals have two twinfilin isoforms whose subcellular localizations and tissue distributions are differentially regulated. *J Biol Chem* 278, 34347-34355.

Velez-Ortega, A.C., Freeman, M.J., Indzhykulian, A.A., Grossheim, J.M., and Frolenkov, G.I. (2017). Mechanotransduction current is essential for stability of the transducing stereocilia in mammalian auditory hair cells. *Elife* 6.

Velez-Ortega, A.C., and Frolenkov, G.I. (2019). Building and repairing the stereocilia cytoskeleton in mammalian auditory hair cells. *Hear Res* 376, 47-57.

Virtanen, P., Gommers, R., Oliphant, T.E., Haberland, M., Reddy, T., Cournapeau, D., Burovski, E., Peterson, P., Weckesser, W., Bright, J., van der Walt, S.J., Brett, M., Wilson, J., Millman, K.J., Mayorov, N., Nelson, A.R.J., Jones, E., Kern, R., Larson, E., Carey, C.J., Polat, I., Feng, Y., Moore, E.W., VanderPlas, J., Laxalde, D., Perktold, J., Cimrman, R., Henriksen, I., Quintero, E.A., Harris, C.R., Archibald, A.M., Ribeiro, A.H., Pedregosa, F., van Mulbregt, P., and SciPy, C. (2020). SciPy 1.0: fundamental algorithms for scientific computing in Python. *Nat Methods* 17, 261-272.

Wells, H.R.R., Freidin, M.B., Zainul Abidin, F.N., Payton, A., Dawes, P., Munro, K.J., Morton, C.C., Moore, D.R., Dawson, S.J., and Williams, F.M.K. (2019). GWAS Identifies 44 Independent Associated Genomic Loci for Self-Reported Adult Hearing Difficulty in UK Biobank. *Am J Hum Genet* 105, 788-802.

Willott, J.F. (2006). Measurement of the auditory brainstem response (ABR) to study auditory sensitivity in mice. *Curr Protoc Neurosci* Chapter 8, Unit8 21B.

Wilmarth, P.A., Krey, J.F., Shin, J.B., Choi, D., David, L.L., and Barr-Gillespie, P.G. (2015). Hair-bundle proteomes of avian and mammalian inner-ear utricles. *Sci Data* 2, 150074.

Yamagishi, A., Masuda, M., Ohki, T., Onishi, H., and Mochizuki, N. (2004). A novel actin bundling/filopodium-forming domain conserved in insulin receptor tyrosine kinase substrate p53 and missing in metastasis protein. *J Biol Chem* 279, 14929-14936.

Yamoah, E.N., Lumpkin, E.A., Dumont, R.A., Smith, P.J., Hudspeth, A.J., and Gillespie, P.G. (1998). Plasma membrane Ca2+-ATPase extrudes Ca2+ from hair cell stereocilia. *J Neurosci* 18, 610-624.

Yan, K., Zong, W., Du, H., Zhai, X., Ren, R., Liu, S., Xiong, W., Wang, Y., and Xu, Z. (2022). BAIAP2L2 is required for the maintenance of mechanotransducing stereocilia of cochlear hair cells. *J Cell Physiol* 237, 774-788.

Zampini, V., Ruttiger, L., Johnson, S.L., Franz, C., Furness, D.N., Waldhaus, J., Xiong, H., Hackney, C.M., Holley, M.C., Offenhauser, N., Di Fiore, P.P., Knipper, M., Masetto, S., and Marcotti, W. (2011). Eps8 regulates hair bundle length and functional maturation of mammalian auditory hair cells. *PLoS Biol* 9, e1001048.

Zhao, B., Wu, Z., Grillet, N., Yan, L., Xiong, W., Harkins-Perry, S., and Muller, U. (2014). TMIE is an essential component of the mechanotransduction machinery of cochlear hair cells. *Neuron* 84, 954-967.

Zhao, H., Pykalainen, A., and Lappalainen, P. (2011). I-BAR domain proteins: linking actin and plasma membrane dynamics. *Curr Opin Cell Biol* 23, 14-21.

Zhao, H.B., and Yu, N. (2006). Distinct and gradient distributions of connexin26 and connexin30 in the cochlear sensory epithelium of guinea pigs. *J Comp Neurol* 499, 506-518.

Zhao, Y., Yamoah, E.N., and Gillespie, P.G. (1996). Regeneration of broken tip links and restoration of mechanical transduction in hair cells. *Proc Natl Acad Sci U S A* 93, 15469-15474.

Zhu, Y., Scheibinger, M., Ellwanger, D.C., Krey, J.F., Choi, D., Kelly, R.T., Heller, S., and Barr-Gillespie, P.G. (2019). Single-cell proteomics reveals changes in expression during hair-cell development. *Elife* 8.

Zine, A., and Romand, R. (1996). Development of the auditory receptors of the rat: a SEM study. *Brain Res* 721, 49-58.